ALLSENSORS 2026

The Eleventh International Conference on Advances in Sensors, Actuators, Metering and Sensing

ISBN: 978-1-68558-388-0

May 24 - 28, 2026

Venice, Italy

ALLSENSORS 2026 Editors

Paulo Estevao Cruvinel, Embrapa Instrumentation, Brazil

ALLSENSORS 2026

Forward

The Eleventh International Conference on Advances in Sensors, Actuators, Metering and Sensing (ALLSENSORS 2026), held between May 24, 2026, and May 28, 2026, in Venice, Italy, continued a series of events covering related topics on theory, practice, and applications of sensor devices, techniques, data acquisition and processing, and on wired and wireless sensors and sensor networks.

Sensors and sensor networks have a great potential of providing diverse services to broad range of applications, not only in science and engineering, but equally importantly on issues related to critical infrastructure protection and security, healthcare, the environment, energy, food safety, and the potential impact on the quality of all areas of life.

We take here the opportunity to warmly thank all the members of the ALLSENSORS 2026 technical program committee, as well as all the reviewers. The creation of such a high-quality conference program would not have been possible without their involvement. We also kindly thank the authors who dedicated time and effort to contribute to ALLSENSORS 2026. We truly believe that, thanks to all these efforts, the final conference program consisted of top-quality contributions. We also thank the members of the ALLSENSORS 2026 organizing committee for their help in handling the logistics of this event.

We hope that ALLSENSORS 2026 was a successful international forum for the exchange of ideas and results between academia and industry or the promotion of progress in the field of sensors, actuators, metering, and sensing.

ALLSENSORS 2026 Chairs

ALLSENSORS 2026 Steering Committee
Michael Niedermayer, Berliner Hochschule für Technik, Germany
Paulo E. Cruvinel, Embrapa Instrumentation, Brazil
Matteo Tonezzer, CNR-IMEM, Trento, Italy
Sandrine Bernardini, Aix Marseille University, France
Almudena Rivadeneyra, Universidad de Granada, Spain
Laura Garcia, Universidad Politécnica de Cartagena, Spain
Sung Ho Cho, Hanyang University, South Korea

ALLSENSORS 2026 Publicity Chairs
José Miguel Jiménez, Universitat Politecnica de Valencia, Spain
Francisco Javier Díaz Blasco, Universitat Politècnica de València, Spain
Ali Ahmad, Universitat Politècnica de València, Spain
Sandra Viciano Tudela, Universitat Politecnica de Valencia, Spain
Laura Garcia, Universidad Politécnica de Cartagena, Spain

ALLSENSORS 2026
Committee

ALLSENSORS 2026 Steering Committee

Michael Niedermayer, Berliner Hochschule für Technik, Germany
Paulo E. Cruvinel, Embrapa Instrumentation, Brazil
Matteo Tonezzer, CNR-IMEM, Trento, Italy
Sandrine Bernardini, Aix Marseille University, France
Almudena Rivadeneyra, Universidad de Granada, Spain
Laura Garcia, Universidad Politécnica de Cartagena, Spain
Sung Ho Cho, Hanyang University, South Korea

ALLSENSORS 2026 Publicity Chairs

José Miguel Jiménez, Universitat Politecnica de Valencia, Spain
Francisco Javier Díaz Blasco, Universitat Politècnica de València, Spain
Ali Ahmad, Universitat Politècnica de València, Spain
Sandra Viciano Tudela, Universitat Politecnica de Valencia, Spain
Laura Garcia, Universidad Politécnica de Cartagena, Spain

ALLSENSORS 2026 Technical Program Committee

Francesco Aggogeri, University of Brescia, Italy
Otman Aghzout, National School of Applied Sciences of Tetouan, Morocco
Amin Al-Habaibeh, Nottingham Trent University, UK
Youssef Altherwy, Prince Sattam bin Abdulaziz University, Saudi Arabia
Darius Andriukaitis, Kaunas University of Technology, Lithuania
Piotr Artiemjew, University of Warmia and Mazury, Poland
Farzad Asgarian, University of Michigan, Ann Arbor, USA
Herve Aubert, Laboratory for Analysis and Architecture of Systems (LAAS-CNRS), France
Yang Bai, University of Maryland College Park, USA
Roberto Beghi, Università degli Studi di Milano, Italy
Artur Bejger, Maritime University of Szczecin, Poland
Roc Berenguer Pérez, TECNUN - Technological Campus of the University of Navarra, Spain
Sandrine Bernardini, Aix Marseille University, France
Mourad Bezzeghoud, University of Évora, Portugal
Xavier Boddaert, Mines Saint Etienne | Centre Microélectronique de Provence (CMP), France
Muhammad Ali Butt, Warsaw University of Technology, Poland
Maria Candelaria Hernandez Goya, Universidad de La Laguna, Spain
Juan Vicente Capella Hernández, Universitat Politècnica de València, Spain
Vítor Carvalho, 2AI-EST-IPCA / Algoritmi Research Centre - UM, Portugal
Paula María Castro Castro, Universidade da Coruña, Spain
Debashish Chakravarty, IIT Khaargpur, India
M Girish Chandra, TCS Research, India
Bocheng Chen, University of Mississippi, USA

Copyright Information

For your reference, this is the text governing the copyright release for material published by IARIA.

The copyright release is a transfer of publication rights, which allows IARIA and its partners to drive the dissemination of the published material. This allows IARIA to give articles increased visibility via distribution, inclusion in libraries, and arrangements for submission to indexes.

I, the undersigned, declare that the article is original, and that I represent the authors of this article in the copyright release matters. If this work has been done as work-for-hire, I have obtained all necessary clearances to execute a copyright release. I hereby irrevocably transfer exclusive copyright for this material to IARIA. I give IARIA permission or reproduce the work in any media format such as, but not limited to, print, digital, or electronic. I give IARIA permission to distribute the materials without restriction to any institutions or individuals. I give IARIA permission to submit the work for inclusion in article repositories as IARIA sees fit.

I, the undersigned, declare that to the best of my knowledge, the article is does not contain libelous or otherwise unlawful contents or invading the right of privacy or infringing on a proprietary right.

Following the copyright release, any circulated version of the article must bear the copyright notice and any header and footer information that IARIA applies to the published article.

IARIA grants royalty-free permission to the authors to disseminate the work, under the above provisions, for any academic, commercial, or industrial use. IARIA grants royalty-free permission to any individuals or institutions to make the article available electronically, online, or in print.

IARIA acknowledges that rights to any algorithm, process, procedure, apparatus, or articles of manufacture remain with the authors and their employers.

I, the undersigned, understand that IARIA will not be liable, in contract, tort (including, without limitation, negligence), pre-contract or other representations (other than fraudulent misrepresentations) or otherwise in connection with the publication of my work.

Exception to the above is made for work-for-hire performed while employed by the government. In that case, copyright to the material remains with the said government. The rightful owners (authors and government entity) grant unlimited and unrestricted permission to IARIA, IARIA's contractors, and IARIA's partners to further distribute the work.

Table of Contents

Electrical Conductivity Modeling of SiO_2/CuBr Composite Sensitive Layer for Ammonia Gas Sensor Application

Caroline Lambert-Mauriat, Princesse N'Nang M'Boukou, Lisa Weber, Virginie Martini, Marc Bendahan
Aix Marseille Univ, Université de Toulon, CNRS, IM2NP
Marseille, France
e-mail: {caroline.mauriat | virginie.martini | marc.bendahan}@im2np.fr
e-mail: nnangmboukou@yahoo.com
e-mail: lisarm.weber@gmail.com

***Abstract*—Skin-perspired ammonia (NH_3) could be used for non-invasive medical monitoring of patients suffering from chronic kidney disease. Copper-bromide (CuBr) based sensors are known to be very selective to ammonia at room-temperature, making them specially adapted for such applications. However, their sensitivity remains insufficient and requires further improvement, as around 100 ppb of NH_3 must be detected. In a previous work, this limitation is addressed by employing a sensing layer based on a mesoporous SiO_2 matrix impregnated with a CuBr solution. To better understand the mechanisms involved in electrical conductivity of this layer, a numerical model is introduced here. Based on random unit conductivity lattice, the model considers both porosity and disorder. Total conductivity is deduced from the calculation of electrical potential at each node of the conductivity lattice. Numerical results show that 18% of impregnated CuBr is required to observe an increase in total conductivity. This concentration is consistent with the value of 13% experimentally observed, and for which the sensor performance is optimal.**

Keywords-Sensors; Simulation; Modeling.

I. Introduction

Non-invasive devices that enable continuous medical monitoring offer numerous benefits to patients, such as a reduced risk of infection, data storage, and ability to perform examinations at home. As an alternative to urine and blood tests, detection of skin-emitted ammonia on patients suffering from chronic kidney disease is chosen. Indeed, previous studies showed that ammonia rate in blood is linked with transdermal ammonia concentration [1][2].

Most NH_3 microsensors are based on metal oxides such as SnO_2 or WO_3. While these materials are widely used, metal-oxide-based sensors generally require high operating temperatures in the range of $200 - 450°C$ and exhibit poor selectivity due to their sensitivity to a broad variety of interfering gases. An alternative strategy for improving microsensor selectivity relies on molecular recognition, which is based on specific interactions between the target gas and highly mobile species in solids, especially mobile ions in ionic or mixed conductors. In this sense, previous studies showed that CuBr is a promising candidate. Indeed, upon exposure to ammonia, Cu^+ ions migrate toward the surface, where they form $[Cu(NH_3)_2]^+$ complexes. This ionic redistribution induces an accumulation of copper vacancies at the surface and a depletion of interstitial Cu^+ ions, resulting in a widening of the depletion layer and a decrease in the overall electrical conductivity [3][4]. In addition to this high selectivity, CuBr-based sensors exhibit high sensitivity toward ammonia and operate at room temperature, which is crucial for sensors intended for skin contact. Then, in this work, CuBr is chosen for NH_3 detection, as transdermal ammonia concentrations are estimated around 100 ppb [5]. The sensitive layer of the sensors developed in a previous work [6] is made of small CuBr nanocrystals, obtained by impregnating the ionic conductor within a mesoporous silica matrix synthesized by a sol–gel process. The regular repartition of CuBr within the pores and the large specific surface area of the mesoporous network promotes high sensitivity as well as fast response and recovery kinetics. Gas sensing measurements in the presence of very low concentrations of NH_3 $(100 - 500$ ppb) demonstrated that the sensor combines high sensitivity with strong selectivity, thereby supporting the validity of the approach.

For better understanding, effect of the porosity on total conductivity is studied in this work by introducing a numerical model, which considers both the morphology of the layer (size of CuBr particles and pores, composition) and the different constitutive conductivities, as silica is an insulator and CuBr a mixed conductor.

The organization of the paper is the following. The numerical model is introduced in Section II. Then, results are presented and discussed in Section III. Finally, the paper concludes with Section IV.

II. Numerical Model and Methods

A two-step approach is used in this study. First, the sensitive layer is modeled by considering its structural properties (porosity, composition, grain size). Secondly, a conductance lattice whose total conductivity is calculated by classical method is build.

A. Mesoporous Layer Modeling

Sensor realization, along with the morphological and electrical characterization of the sensitive layer, has been detailed in our previous work [6]. Structural analysis revealed that the mesoporous SiO_2 layer exhibits a disordered, worm-like porous network with a porosity of 56% (Figure 1). Impregnation of the mesopores by CuBr is clearly visible (CuBr appears light grey).

 ISBN: 978-1-68558-388-0

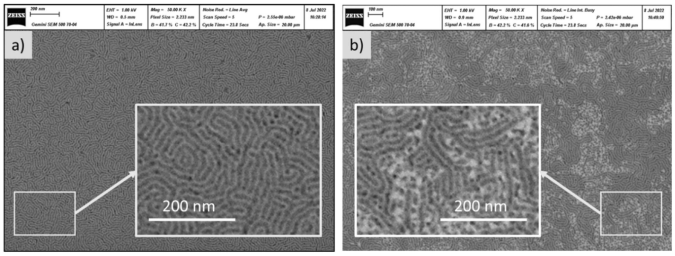

Figure 1. SEM images of the mesoporous SiO_2 film: before (a) and after (b) impregnation with CuBr, from [6].

Moreover, the mapping obtained by Energy-Dispersive X-ray (EDX) spectroscopy shows a homogeneous dispersion of CuBr throughout the thickness of the layer (Figure 2).

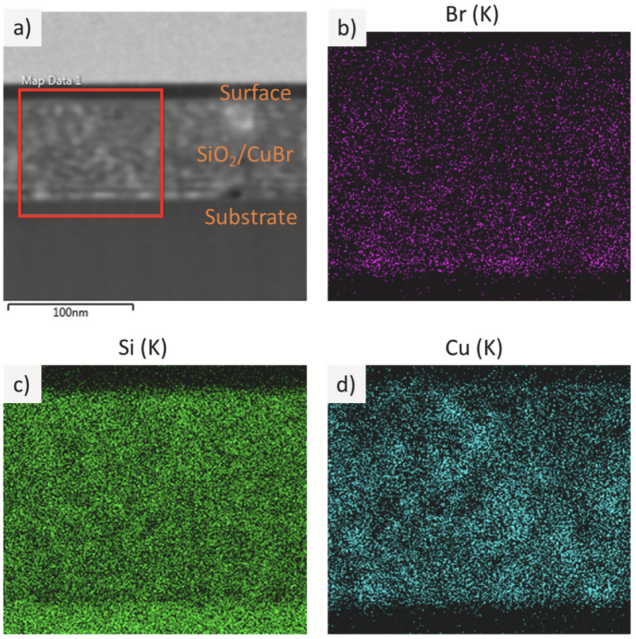

Figure 2. EDX mapping of the CuBr-impregnated SiO_2 mesoporous layer: distribution of the K line, for Br (b), Si (c) and Cu (d) atoms, in the area outlined in red on the image obtained by STEM (a), from [6].

Based on these observations, the sensitive layer is modeled by a simple cubic lattice. Each lattice site is the center of a unit cube corresponding either to CuBr crystal or to SiO_2 crystal. Then, sites are randomly occupied by CuBr (with a probability p) or by SiO_2 (with a probability $q = 1 - p$) (Figure 3-a). This lattice is converted to a cubic array of conductance by adopting the following rules: if two nearby sites are occupied by CuBr, the bond that connects them has a conductance g_{CuBr}; if they are occupied by SiO_2, the corresponding bond takes the value g_{SiO_2}; finally, if the two sites are occupied one by CuBr and the other by SiO_2, the conductance of the bond is an interface conductance noted g_{int} (Figure 3-b).

Porosity is introduced by removing 60% of the lattice sites consisting solely of SiO_2. Then, the unoccupied sites are randomly filled by CuBr in the concentration range of 0 to 100%. Thus, the CuBr filling in the overall volume, i.e., SiO_2 plus pores, varies from 0 to 60%. When at least one site is unoccupied, the corresponding bond is set to g_{por}. Figure 3 illustrates this approach for a two-dimensional lattice without porosity, which is easier to represent. However, its generalization to three dimensions is very simple.

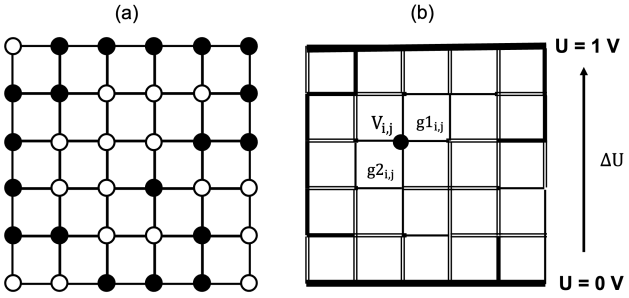

Figure 3. Two-dimensional representation of the conductance array (b) derived from the site lattice (a): the thick lines connect two sites occupied by SiO_2 (black sites); the thin lines connect two sites occupied by CuBr (white sites) ; finally, the double lines connect sites occupied by both. $V_{i,j}$ is the potential at the node (i, j) from which the two conductances, $g1_{i,j}$ and $g2_{i,j}$, are defined.

The choice of conductivity values is based on our knowledge of the various components of the sensitive layer. Copper bromide (CuBr) is a mixed conductor whose conductivity is highly dependent on the processing conditions and the temperature at which the measurement is carried out. Indeed, β-CuBr phase has an ionic conductivity greater than 1 S/cm, whereas the γ-CuBr phase presents a smaller value of ionic conductivity, the transition temperature being around 380 °C [7]. Then, the conductivity of CuBr layers deposited by radio frequency magnetron sputtering from compacted powder target is $\sigma \approx 5.10^{-7}$ S/cm at T = 25°C [8]. At the same temperature, grain conductivity measured by impedance spectroscopy on poly-crystallin CuBr is $\sigma \approx 3.10^{-5}$ S/cm [7]. On the other hand, SiO_2 is an insulator whose conductivity is between 10^{-16} and 10^{-12} S/cm (crystal) and less than 10^{-18} S/cm (amorphous).

Thus, the ratio of conductances being between 10^{-5} and 10^{-13}, simulations are carried out with $g_{CuBr} = 1$ and $g_{SiO_2} = 10^{-9}$.

It is more difficult to determine the interface conductivity, g_{int}, which is unknown and not estimated by experiments. However, previous work on CuBr/TiO_2 composite showed that conductivity is increased at the CuBr-TiO_2 interfaces [9]. By considering that CuBr-TiO_2 composites are like CuBr-SiO_2 ones, the arbitrary value $g_{int} = 10$ is used. Finally, the porosity bond is set to $g_{por} = 10^{-12}$, corresponding to an insulator.

Moreover, to minimize size effects, periodic boundary conditions are applied: the bonds of the two terminal planes are copied, such as the plane at abscissa 0 is equal to the plane at abscissa L, and that for the two directions perpendicular to the electrode planes.

B. Total Conductivity Calculation

Kirchoff's law says that the sum of currents is null at each node. The total dissipated power is given by:

$$P_T = \sum_{i,j} g1_{i,j}(V_{i,j} - V_{i+1,j})^2 + g2_{i,j}(V_{i,j} - V_{i,j+1})^2, \quad (1)$$

where $V_{i,j}$ is the potential at the node (i,j) and $g1_{i,j}, g2_{i,j}$ are conductances between (i,j) and $(i+1,j)$ sites, and between (i,j) and $(i,j+1)$ sites, respectively (Fig. 3-b). Otherwise, the dissipated power is:

$$P_T = G_T \Delta U, \quad (2)$$

where ΔU is the electrical potential difference applied to the conductance lattice (Fig. 3-b). If $\Delta U = 1$V, the total conductance is numerically equal to total power.

Therefore, the problem can be reduced to the calculation of the potentials $V_{i,j}$ at each site, using an exact or an approximated method. Because of the disorder and the relatively large size of the considered systems, the choice of approximated method is done here.

By applying Kirchhoff's law, the potential at each node is expressed as a function of the conductance of the links connecting it to neighboring nodes as follows:

$$V_{i,j} = \frac{g1_{i,j}V_{i+1,j} + g1_{i-1,j}V_{i-1,j} + g2_{i,j}V_{i,j+1} + g2_{i,j-1}V_{i,j-1}}{g1_{i,j} + g2_{i,j} + g1_{i-1,j} + g2_{i,j-1}} \quad (3)$$

The over-relaxation method is used to determine these potentials when the system is at equilibrium. This method consists of iteratively calculating the potentials until constant values are obtained. At first iteration, $V^0_{i,j}$ potentials are set to 0, then at the $n+1$ iteration, the potential at node (i,j) is:

$$V^{n+1}_{i,j} = \omega \tilde{V}_{i,j} + (1-\omega) V^n_{i,j}, \quad (4)$$

where the potential $\tilde{V}_{i,j}$ is obtained by substituting the potential $V^n_{i,j}$ in (3). The value of the relaxation parameter ω plays a major role in the convergence speed of the algorithm [10]. Among its properties, it is worth noting that it must be between 1 and 2 and that there is an optimal value for which the number of iterations is minimal:

$$\omega_{opt} = \frac{2}{1 + \sqrt{1 - \rho^2_{Jacobi}}} \quad (5)$$

In these simulations, Jacobi's spectral radius, ρ_{Jacobi}, is equal to $cos(\pi/L)$, where L is the size of the lattice.

III. Results and Discussion

To determine the optimal lattice size, in terms of balance between accuracy and computing time, the total conductivity is calculated as a function of volume fraction of CuBr without considering porosity. The results obtained for $L = 10, 15, 20$ and 25 are plotted in Figure 4. Only one configuration is considered for each volume fraction of CuBr. Beyond $L = 20$, the curves converge and present a bell-shape with a maximum around 0.6 volume fraction of CuBr, which agrees with previous works on composite systems like Au-YBCO [11] or CuBr-TiO_2 [9]. From these results, $L = 25$ is kept in the following calculations.

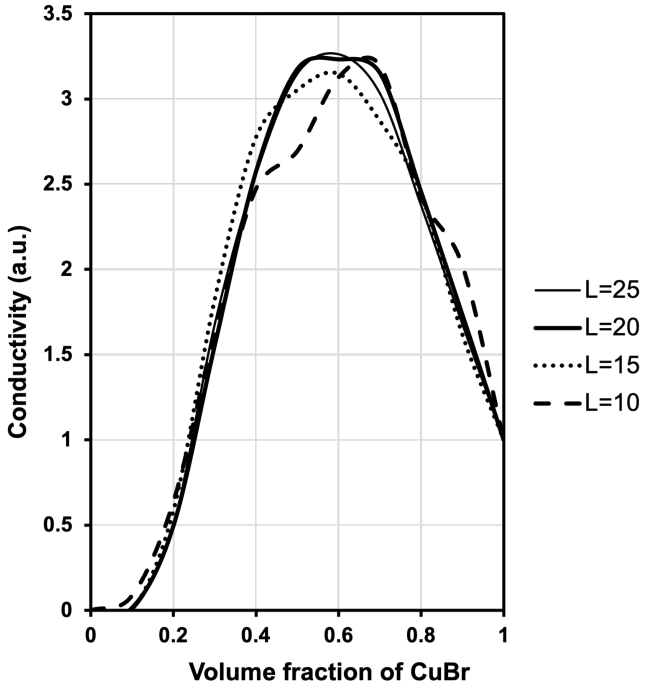

Figure 4. Variation of the total conductivity as a function of the volume fraction of CuBr. Results obtained for $L = 10$ (dashed line), $L = 15$ (small dots), $L = 20$ (thick line) and $L = 25$ (thin line). Interface conductance is $g_{int} = 10$.

When 60% of porosity is introduced, and gradually filled by CuBr, the total conductivity begins to increase around 0.18 volume fraction of CuBr (Figure 5). This value corresponds to the percolation threshold, p_c, which is the volume fraction

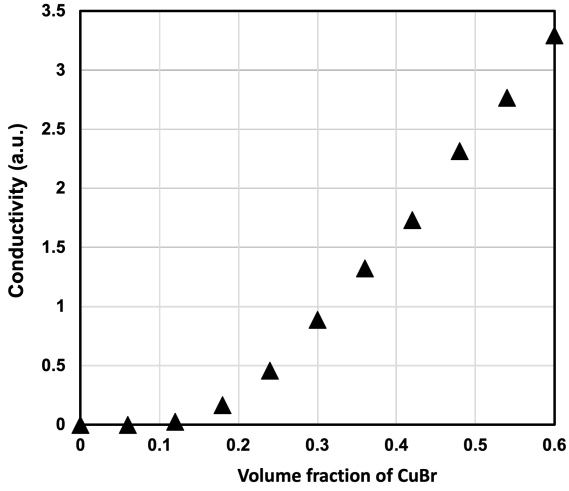

Figure 5. Variation of the total conductivity as a function of the volume fraction of CuBr into a sample made of SiO_2 with a random porosity of 60%.

of CuBr at which infinite cluster appears. For simple cubic lattice, such as considered in this work, $p_c = 0.247$ in the case of bond percolation, and $p_c = 0.307$ in the case of site percolation, considering geometric arrangement of two types of bonds or sites. The system considered here is different as it involves 3 types of bonds. Notice that the conductivity value for 0.6 volume fraction of CuBr, around 3.25, corresponds to the maximum of the curve obtained without considering porosity.

Good agreement is observed when comparing the variation of sensor resistance (Figure 6) and the calculated resistance in the same range of CuBr filling (Figure 7).

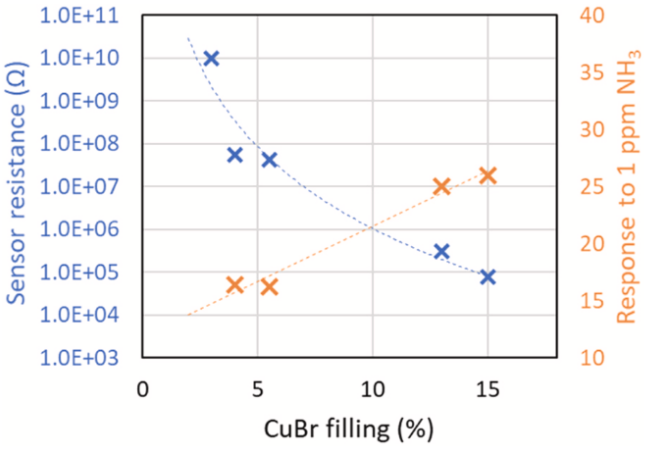

Figure 6. Effect of CuBr filling on the sensor resistance and the sensor response to 1 ppm NH_3, from [6].

Indeed, not only the general trend is recovered, but also the order of magnitude: three decades in resistance sensor as CuBr filling varies from 5% to 15%.

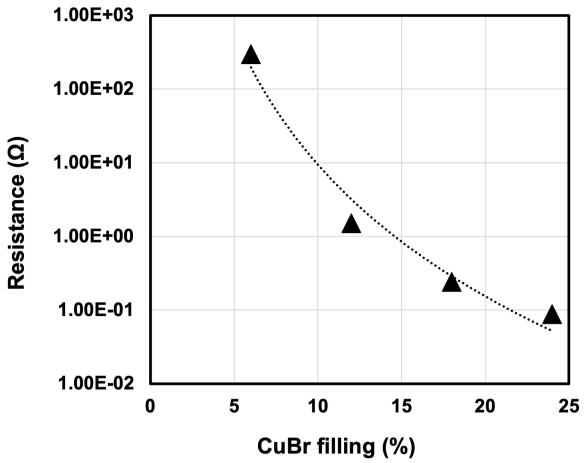

Figure 7. Total calculated resistance in the range 0 to 25% of CuBr filling.

IV. Conclusion and Future Work

In this paper, we developed a numerical model to study the electrical conductivity of SiO_2-sensitive mesoporous layers impregnated with CuBr for ammonia gas sensor applications. The approach consisted of modeling the disordered porous structure by a random conductance network, considering both the porosity and the different conductivities of CuBr, SiO_2 and their interfaces. The total conductivity was then calculated using an over-relaxation method applied to the conductance network. Calculation shows that less than 18% of CuBr in the total volume is enough to obtain a conducting path in the insulator SiO_2 mesoporous matrix. This value agrees with the experiment in which higher sensor performances are reached for a sensitive layer composed of 13% CuBr, 44% SiO_2 and 43% of remaining porosity. The worm-like structure being well modeled by random porosity, it seems unnecessary to build a numerical sample with worm-like porosity. However, additional measurements, such as impedance spectroscopy coupled with calculations for other values of g_{int} would be useful to better characterize the interfaces.

References

[1] K. Nose *et al.*, "Identification of ammonia in gas emanated from human skin and its correlation with that in blood," *Analytical sciences : the international journal of the Japan Society for Analytical Chemistry*, vol. 21, no. 12, pp. 1471–1474, 2005.

[2] D. Czarnowski, J. Górski, J. Jóźwiuk, and A. Borón-Kaczmarska, "Plasma ammonia is the principal source of ammonia in sweat," *European journal of applied physiology and occupational physiology*, vol. 65, no. 2, pp. 135–137, 1992.

[3] P. Lauque *et al.*, "Electrical properties and sensor characteristics for NH_3 gas of sputtered CuBr films," *Sensors and Actuators B: Chemical*, vol. 59, no. 2, pp. 216–219, 1999.

[4] M. Bendahan *et al.*, *Recent Research Developments in Solid State Ionics 2*, ch. High selectivity copper bromide microsensors for ammonia gas. Trivandrum (India) : Transworld Research Network, 2004.

[5] S. Furukawa *et al.*, "Simultaneous and multi-point measurement of ammonia emanating from human skin surface for the estimation of whole body dermal emission rate," *Journal of Chromatography B*, vol. 1053, pp. 60–64, 2017.

[6] L. Weber *et al.*, "A new approach for selective and ultrasensitive ammonia sensors by cubr encapsulation in a mesoporous thin film for potential metabolic acidosis non-invasive monitoring," *Sensors and Actuators B: Chemical*, vol. 417, p. 136124, 2024.

[7] S. Villain, M.-A. Desvals, G. Clugnet, and P. Knauth, "CuBr by impedance spectroscopy," *Solid State Ionics*, vol. 83, no. 3, pp. 191–198, 1996.

[8] P. Lauque, M. Bendahan, J.-L. Seguin, M. Pasquinelli, and P. Knauth, "Electrical properties of thin-films of the mixed ionic-electronic conductor cubr: influence of electrode metals and gaseous ammonia," *Journal of the European Ceramic Society*, vol. 19, no. 6, pp. 823–826, 1999.

[9] G. Albinet, J. Debierre, P. Knauth, C. Lambert, and L. Raymond, "Enhanced conductivity in ionic conductor-insulator composites: numerical models in two and three dimensions," *The European Physical Journal B*, vol. 22, pp. 421–427, 2001.

[10] W. H. Press, S. A. Teukolsky, W. T. Vetterling, and B. P. Flannery, *Numerical Recipes in C (2nd Ed.): The Art of Scientific Computing*. New York, NY, USA: Cambridge University Press, 1992.

[11] C. Lambert, J.-M. Debierre, G. Albinet, and J. Marfaing, "Temperature dependence of the resistivity in Au–$YBa_2Cu_3O_x$ sintered composites," *Philosophical Magazine Part B*, vol. 79, no. 7, pp. 1029–1044, 1999.

Advances on the Internet of Things for High-Resolution and Multi-Scale Measurements in Agricultural Ecosystems

Christophe Cariou, Laure Moiroux-Arvis, Jean-Pierre Chanet
Université Clermont Auvergne - INRAE, UR TSCF
Aubière, France
emails: christophe.cariou@inrae.fr, laure.moiroux-arvis@inrae.fr, jean-pierre.chanet@inrae.fr

***Abstract*—This article presents an overview of recent advances in sensors and data collection applied to monitoring agricultural ecosystems. It first describes a range of innovative sensors currently under development, at both microscopic and macroscopic scales. Next, it highlights recent approaches to collecting data from these sensors in the field, via wireless and satellite communications and data collectors mounted on autonomous vehicles. An example of data collection by drone is presented in this regard. Finally, several future research directions concerning the Internet of Things applied to agroecology are discussed, with a focus on energy consumption and life cycle. Knowledge of these advances invites us to consider new perspectives in agroecology, but also to reflect on the means and policies that could support farmers to adopt these new technologies on a large scale.**

Keywords-Internet of Things; Sensors; Wireless communications; Agricultural ecosystems.

I. INTRODUCTION

Faced with climatic, environmental and demographic challenges, one of the objectives of agroecology - which is a multi-scale and holistic concept (from the plant to the food distribution) - is to develop agricultural ecosystems leading to the preservation of natural resources while generating efficient crop production and positive socio-economic outcomes [1]. To this end, emphasis is placed on significantly reducing the use of chemical inputs by creating conditions conducive to the development of biological diversity and soil fertility. This is achieved through crop diversification and landscape modification as illustrated in Fig. 1. In fact, the spatial and temporal diversification of crops improves agronomic sustainability by limiting pest infestations, reducing disease pressure, mitigating soil degradation and strengthening the overall resilience to climatic variability [2]. Furthermore, rotating crops improves soil fertility and structure, reduces pesticide use by disrupting pest cycles, and contributes to increase biodiversity. These agroecological practices can moreover generate more stable agricultural yields and higher incomes than conventional agriculture [3].

However, the adoption of such agricultural practices remains uncommon on a large scale due to the difficulty of managing highly diversified crops by the farmer. These ecosystems require in fact specific and close monitoring of soil health, plant growth and biodiversity - at both macroscopic and microscopic scales - in order to optimize crop production and detect anomalies early [4]. The Internet of Things has thus a crucial role to play in this regard by designing appropriate sensors and developing relevant data collection strategies [5]. As illustrated in Fig. 2, the ultimate goal is to create a reactive closed-loop process: environmental and biological data are collected remotely in the field, then shared in the cloud and combined with human expertise and history of previous agricultural operations to feed databases, models, scenarios and decision-making algorithms. This feedback process aims to improve the biological interactions and crop production over time, while being able to rapidly adapt to perturbations and varying environmental conditions.

(a) (b) (c)

Figure 1. Examples of spatial arrangements fostering biological interactions: (a) Strip intercropping, (b) Pixel cropping, (c) Permaculture.

However, remotely collecting a wide range of data on several crops at high spatial resolution - in near real-time and at both microscopic and macroscopic scales - poses many challenges. On the one hand, the design of sensors able to measure the state of living soil, the presence of species and the plant health is challenging. On the other hand, the high variability inherent to the spatial distribution of plants requires deploying a significant number of sensors with a high spatial resolution [6]. This creates new challenges, especially in terms of sensor distribution and data collection strategies. These challenges are in addition to the problems of energy consumption, environmental footprint, connectivity in areas without communication facilities and frugality of sensing infrastructures [7]. Recent advances in sensor development, satellite communications, ground and air robotic systems, as well as in edge computing and embedded artificial intelligence, are however opening up new opportunities for meeting these challenges.

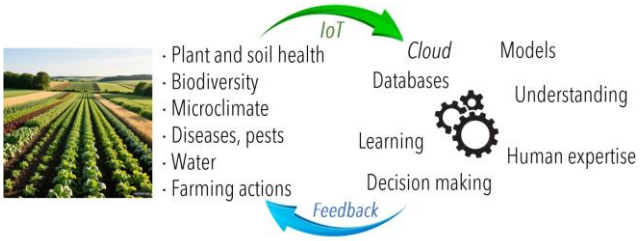

Figure 2. Closed-loop process to adapt farming actions accordingly.

This article presents an overview of recent advances in sensor design and data collection applied to the monitoring of agricultural ecosystems. It is organized as follows. Section II presents a set of innovative sensors currently under development at both microscopic and macroscopic scales. Section III reviews recent approaches to conducting remote data collection in the field, with an emphasis on energy consumption issues. Section IV illustrates a process of data collection using drones. Finally, Section V presents the conclusion and discusses future research directions.

II. SENSORS FOR MONITORING AGRICULTURAL ECOSYSTEMS

Agricultural ecosystems are living systems that are particularly complex to monitor and understand. In order to optimally and sustainably manage the crop production, remote sensing of environmental and biological data is of increasing importance. As illustrated in Fig. 3, this data concerns the soil, the plants, the biodiversity (below and above ground), the climate (global and at the plant level) and the human operations. To collect this data, sensors are the first step in the chain of the Internet of Things. Some are specifically designed to observe the state of living soil and assess the presence of species, others enable to monitor crop growth and plant physiology, whether it be at the microscopic or macroscopic scale. In this Section, we present an overview of particularly innovative sensors currently under development (indicated in red in Fig. 3) in this regard.

A. Measurements at macroscopic scale

1) Soil monitoring: The soil provides the structural support, water, and nutrients necessary for plant growth. It is a living ecosystem containing microorganisms, insects and plant roots. Regularly monitoring the soil health is essential for maintaining a sustainable production [8]. Although the metrics are not well established to quantify the soil health [9], some indicators, grouped into biological, physical, chemical, and functional dimensions of soil functioning, are reported in the literature [10].

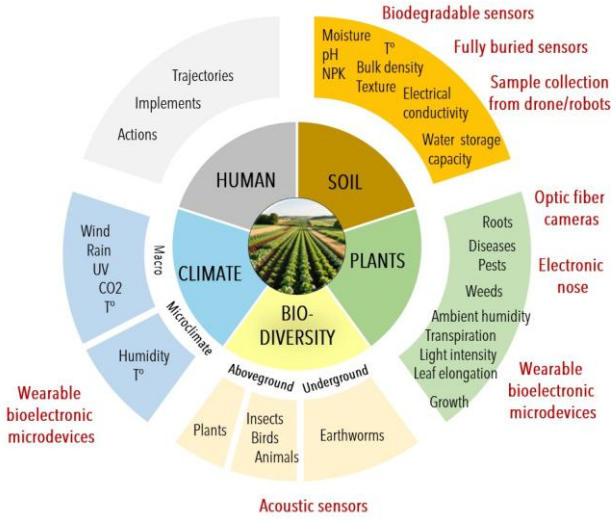

Figure 3. Main data to be monitored in agricultural ecosystems. The text in red indicates recent sensors under development presented in this paper.

The current solutions to assess these indicators remain however limited to a few localized and macroscopic measurements obtained from in situ sensors. The main data monitored within an agricultural ecosystem include soil moisture, temperature, pH, nutrient levels, and electrical conductivity [11]. These measurements are collected using probes buried in in the root zone and radio antennas are positioned on the surface to transmit the measurements. Alternatively, three other innovative approaches are currently being investigated to collect soil data at high spatial resolution, based respectively on fully buried sensor nodes, biodegradable sensors and sample collection from ground robots and drones.

Fully buried sensor nodes. The development of the concepts of Internet of Underground Things (IoUT) and Wireless Underground Sensor Networks (WUSNs) is a recent paradigm aiming to completely bury the sensor nodes, including the radio components [12]. The main advantage lies in the possibility of positioning them anywhere, including in the path of agricultural vehicles, and therefore of easily multiply them in a field. They are moreover protected against the damages generally suffered by surface radio antennas (e.g., damages due to agricultural implements, weathering, theft). However, as the propagation of the electromagnetic waves is much more attenuated in the soil than in the air, about 20 to 300 times worse [13], several scientific and technological challenges remain to overcome, whether it be in terms of communication ranges (usually only a few tens of meters), data collection and energy consumption. The use of drones is a relevant way to collect data of buried communicating sensor nodes [14].

Field-deployable biodegradable sensors. The development of biodegradable sensors is another innovative strategy. For example, Gopalakrishnan et al. [15] have designed miniature chipless sensors (2 cm^2) to monitor the soil Volumetric Water Content (VWC) during seed germination. The sensors are based on miniaturized resonant antennas, constructed from biodegradable materials and compatible with radio frequencies. The resonant frequency of the antenna varies with the soil volumetric water content. The objective is to design sensors able to operate a crop season before being slowly degraded. To collect the measurement, a drone carrying a reader module is used at low flying height (40 cm) to send the interrogation signal and read the reflected signal from the sensor tag. The results demonstrated the capability to measure the VWC within the range of 3.7-23.5%. The final goal is to deploy these sensors at a large spatial scale at 5 cm deep by using a seed drill. Unfortunately, the measurements cannot be stored inside the sensors and depend therefore on the time of drone's passage.

Soil sample collection from robotic vehicles. Performing regular soil sample collections remains, however, the primary method for accurately assessing soil health. This task is, however, time-consuming and does not allow for real-time data. Robots are currently increasingly being studied for collecting soil samples or for moving a probe to different depths in the field [16]. Moreover, as ground robots may have difficulty accessing crops, an alternative is

to use drones carrying soil sampling tools. For example, Klopfenstein et al. [17] used a rotary-wing drone to collect soil samples of a few dozen grams in agricultural fields. The difficulties, however, lie in the need to apply significant loads to the ground to collect samples, and develop lightweight tools adapted to the maximal drone's payload.

2) Plant monitoring: Regularly monitoring the plant health and growth is essential in agriculture, not only to improve crop production but also to understand how some plant varieties acclimate to abiotic and biotic stresses (e.g., climate change, diseases). At the macroscopic level, the monitoring of crops (e.g., yields, diseases, pests, weeds) are commonly carried out through visual observations from satellite images, field sensors or cameras embedded on drones or ground robots [18]. However, more and more approaches are studying the development of other methods to detect diseases and pest infestation early.

Electronic noses for plant disease and pest detection. In fact, with global warming and climate change, invasive pests and pathogens are rapidly extending their territory to new geographic areas and can impact the overall ecological balance of agricultural ecosystems. This proliferation of insects, bacteria, viruses and fungi may have a significant impact on agricultural yields and on biodiversity. The early detection is therefore essential. To this end, electronic noses are particularly promising to detect volatile organic compounds emitted by infected plants [19]. In recent years, research has intensified in this area with ultrasensitive electronic noses and recognition algorithms based on artificial intelligence to identify infestation patterns [20]. The simultaneous presence of multiple diseases complicate however the identification processes, and variability of environmental conditions (e.g., temperature, humidity, wind) may impact the olfactory measurements. For example, Huttnerova et al. [21] demonstrated the possibility of measuring the presence of a substance that identifies bark beetle infestations in forests using ground-based measurements. The electronic nose was then mounted on a drone to fly over the canopy. Despite the installation of a one-meter sampling tube positioned at the front of the drone to minimize the influence of air movements on the electronic nose, the detection of the substance proved unsuccessful. The hypotheses put forward were a lower concentration of the substance above the canopy and stronger winds above trees.

3) Biodiversity monitoring: Biodiversity, both aboveground (e.g., birds, insects, animals, plants) and underground (e.g., insects, earthworms, microorganisms), is a major indicator representative of the good health of an ecosystem. In fact, the diversity represents a key element for capacity of pollination, nutrient cycling, pest control, and water filtration. Higher functional and taxonomic diversity enhances agroecosystem resilience, productivity and long-term stability [22]. In particular, insect monitoring is essential in agroecology as these organisms play critical functional roles, including pollination, pest control through natural predation and nutrient cycling. For example, 70% of global food crops depend on insect pollination, making accurate assessment of pollinator populations a priority for sustainable agriculture. However, traditional monitoring methods, such as pan traps, sweep netting, and visual surveys are labor-intensive, provide limited temporal coverage and often only snapshot data that fail to capture the dynamic nature of insect populations [23]. Recent advances in acoustic technologies propose promising alternatives for continuous insect monitoring.

Acoustic sensors for insect monitoring. Continuous insect monitoring is essential in agroecology to provide the information necessary to assess biodiversity status, evaluate habitat quality, and implement targeted interventions. To this end, the development of acoustic sensors aims to detect and classify flying insects based on their wingbeat frequencies and buzzing patterns. The sensors can operate autonomously for extended periods, collecting data at fine temporal scales that enable detailed analysis of daily activity patterns and seasonal population dynamics [24]. Additionally, acoustic detection methods have proven effective for identifying hidden insect infestations where visual inspection is impractical (e.g., in soil) [25]. The integration of machine learning algorithms with acoustic data facilitates automated species identification and number estimation, addressing the critical challenge of processing large volumes of monitoring data.

B. Measurements at microscopic scale

The design of sensors able to measure the health of ecosystems at microscopic scale is a relatively recent research axis. Some bioelectronic sensors, implantable or attached on plant leaves or stems, are beginning to be studied to collect various information (e.g., ambient humidity, transpiration, light intensity, leaf elongation) and evaluate the plant ability to cope with various abiotic and biotic stresses. At the time being, these studies are limited to controlled environments (e.g., laboratories, greenhouses) but the ambition is to design wearable sensors able to operate on plants growing in their natural environment.

Wearable microsensors on plants. The development of wearable microsensors on plants aim to complement the macroscopic approaches [26]. These sensors must be sufficiently flexible and lightweight to minimize their impact on plant growth. For example, Nassar et al. [27] developed a wearable sensor measuring plant growth using stretchable strain sensors attached to the leaf surface. These strain sensors are capable of measuring the elongation of the leaves at the micrometer scale. They transmit the data via Bluetooth transceivers. Similarly, Zhao et al. [28] developed a multifunctional and stretchable sensor attached to the leaves. This sensor measures variables, such as leaf elongation rates, degree of stomata opening, as well as water content and temperature. The challenge to be met in outdoor conditions is that rain, wind, humidity variations, temperature and light intensity can affect the measurements requiring further research in this regard.

Optic fiber and cameras for measuring root growth. Lastly, fiber optic and visual sensing has been studied to accurately measure the root development of plants. With an

optic fiber arranged in a spiral, Tei at al. [29] managed to measure the penetration of root in the soil. Another approach involves installing a camera inside a transparent tube buried in the ground to measure root growth [30].

Acoustic sensors for underground invertebrate monitoring. In an original way, a few studies aimed to assess underground invertebrate activity and root growth from acoustic sensors. Lacoste et al. [31] for example used highly sensitive piezoelectric sensors to measure acoustic emissions due to the growth of maize roots and the creation of burrows by earthworms. One aim is to monitor earthworm activity periods and adapt the farming practices accordingly to mitigate the impact on the active fauna. Further research is conducted to study the presence of other invertebrates having specific frequency ranges.

III. REMOTE DATA COLLECTION

All sensors presented in Section II must be coupled with wireless communication technologies to remotely transfer the measurements to the cloud. To this end, different strategies can be adopted, depending on whether the sensors are static or can be mobile, see Fig. 4. In the case where the sensors are static, they must either reach a communication element (e.g., gateway, cellular antenna, satellite) or a vehicle as drone or ground robot must regularly come close to them to collect their data. Usually, the communications are based on Low Power Wide Area Networks as LoRa and Sigfox, but also on 3G, 4G, 5G, 6G, LTE-M and NB-IoT, or Wi-Fi, Bluetooth, FSK and ZigBee [32]. Recently, satellite communications based on Geostationary Orbit (GEO) satellites or a constellation of nanosatellites in Low Earth Orbit (LEO) are however increasingly studied for the IoT communications [33]. In fact, this technology is particularly relevant for applications facing signal quality issues or requiring highly reliable global coverage.

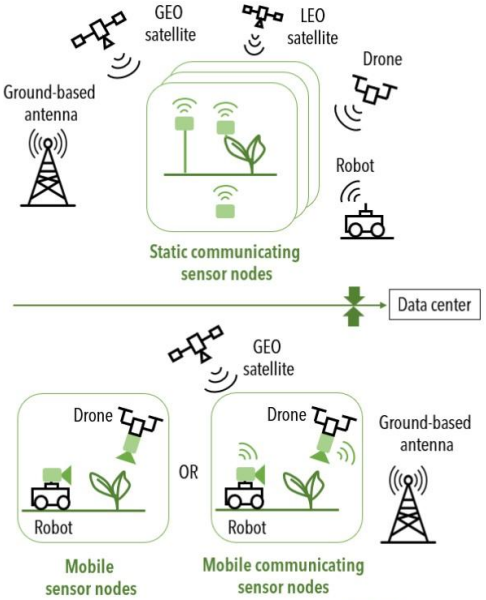

Figure 4. Strategies to collect field data from static and mobile communicating sensor nodes.

Unfortunately, the installation and maintenance costs of static sensor nodes, as well as communication subscription costs, can be a significant obstacle if a large number of sensor nodes need to be deployed. A second issue is the energy consumption of the nodes.

A current challenge is indeed to develop wireless sensor nodes able to operate and communicate with extremely low energy. Low consumption processors, predefined activity schedules or wake-up modules are studied. In particular, by adding an auxiliary Wake-up Receiver (WuR) consuming near-zero energy, the radio frequency spectrum can be continuously monitored for a predefined wake-up signature [34]. When the signal containing the wake-up signature is detected (e.g., sent from a drone), the IoT device in sleep mode is woke-up and its radio activated. This approach aims to highly decrease the node's energy consumption and prolong their operating duration. Another way to reduce the energy consumption of IoT systems lies in local data processing (edge computing). Instead of continuously transmitting raw measurements, sensor nodes can perform preprocessing and transmit only relevant information or alarms. The recent developments in Energy Harvesting (EH) are also particularly promising to supply or recharge self-powered IoT nodes, and even eliminate the need for batteries, see [35]. The energy sources which can be exploited are the ambient ones (e.g., solar, wind, thermal, radio frequency), but also other sources as mechanical ones (e.g., motion of plants) and bioenergy (plants are used as energy sources). For example, the radiation of the frequencies used by telecommunications (i.e., from 3 kHz to 300 GHz) can be harvested to generate a few microwatts sufficient to supply ultra-low-power IoT nodes, see [36]. The exploitation of plant motion is also an interesting strategy to harvest energy. For example, Meder et al. [37] aim to harvest the energy of artificial leaves installed on real leaves by exploiting their motion and oscillations due to wind. Bioenergetical approaches uses the friction of plants, when they come into contact and separate, to exploit the generated electric charges and develop a triboelectric nanogenerator, see [38]. The development of such new energy harvesting technologies is particularly promising for future sensor nodes in agriculture, requiring however to meet several challenges in terms of quantity of energy produced, conversion, storage and consumption.

Some sensors can also be directly mounted on vehicles which can be connected to a communication infrastructure during the data collection. Otherwise, the data is temporarily stored on the vehicle and will be downloaded once back at the farm's docking station. The vehicles (e.g., drones, ground robots) are in charge to displace the sensors within the fields. This mobility is particularly interesting as it is not necessary to excessively increase the number of sensors in the plots (i.e., the same sensor is used several times). Furthermore, other operations can be performed at the same time by the carrier vehicle (e.g., taking soil samples). This approach requires however overcoming many scientific and technological challenges, whether it be in terms of trajectory planning, control, manipulation and connectivity due to dynamic topology and variable network coverage.

IV. DATA COLLECTION BY DRONE

To illustrate a data collection process from static communicating sensor nodes within agricultural ecosystems, this section presents our latest results on this subject. We recently developed communicating sensor nodes which can be buried at 30 cm depth before being fully covered by soil, see Fig. 5. These sensors regularly measure soil moisture and temperature and transmit this information in LoRa 868 MHz through Underground to Aboveground (UG2AG) communications [39]. By using a data receiver mounted on a drone, the objective is to successively approach each node to activate it from a WuR, and then collect data while

(a) (b)

Figure 5. Data collection of buried sensor nodes by using a drone based on RSSI level: (a) Communicating sensor node buried at 30 cm depth before being covered by soil, (b) Drone used to collect the data.

maintaining a high-quality signal (i.e., high value of RSSI). Experiments have shown that the best communications (and therefore data collection) are observed when the drone is positioned directly above the node (RSSI levels greater than -110 dBm). When the drone moves laterally, the RSSI level drops sharply near the ground. However, this strategy poses several challenges, particularly with regard to flight autonomy, optimal trajectory, adapting collection time to the amount of data to be retrieved, and obstacle avoidance by the drone at low flying height.

To enable the installation and removal of sensor nodes, allow rapid deployment across different study sites, and promote hardware reusability, another approach currently investigated is to use a drone equipped with a cable manipulation system to install and move sensor nodes in the field. This approach, similar to drone delivery, brings flexibility but presents numerous challenges in terms of gripping, control and stability.

V. CONCLUSION AND FUTURE WORK

Faced with climate change and the need for sustainable agricultural production, farming methods must adapt and gradually evolve towards greater biological interactions, the preservation of soil fertility and natural resources. New technologies must adapt to these new modes of production by developing efficient sensors and means of collecting data in the field at both high spatial resolution and multi-scales.

Original sensors are currently being developed for this purpose - at microscopic and macroscopic scales - whether they are biodegradable, wearable, or able to detect some odor or sound patterns. To collect the data, different strategies are being studied, ranging from communication with nanosatellites, the use of autonomous drones or ground robots, manipulation of sensors by drones or fully buried approaches. A major challenge is moreover to minimize the energy consumption of sensors and data collection systems, in particular by finding ways to activate them intelligently and harvest energy from different ambient sources.

The ecological impact of the developed solutions requires also to be carefully studied as early as possible in the design and implementation. The consideration of the life cycle of the approaches proposed is in fact essential, necessitating to analyze all the process, from the manufacturing of the different components to the end-of-life with the electronic wastes. A particular attention must also be paid to modular designs, to be able to replace only a part of a device instead of all the system in case of breakdown or need of evolution. There are several ways of development in the IoT sector serving agroecology, making this research particularly captivating and promising.

The adoption of these advances by farmers also raises other challenges, such as the development of specific policies, common standards, and appropriate training. It is therefore necessary to adapt support systems accordingly in order to move towards a fully data-driven agroecology.

ACKNOWLEDGEMENT

This work was supported by the French National Research Agency, OCOD project n°ANR-24-CE25-7644.

REFERENCES

[1] C. Gascuel-Odoux et al., “A research agenda for scaling up agroecology in European countries,” Agronomy for Sustainaible Development, vol. 42(53), pp. 1–18, 2022, doi:10.1007/s13593-022-00786-4

[2] Z. K. Al-Musawi, V. Vona, and I. M. Kulmány, “Utilizing different crop rotation systems for agricultural and environmental sustainability: A review,” Agronomy, vol. 15(8), pp. 1–31 , 2025, doi:10.3390/agronomy15081966

[3] T. B. Mihrete and F. B. Mihretu, “Crop diversification for ensuring sustainable agriculture, risk management and food security,” Global Challenges, vol. 9(2), pp. 1–13, 2025, doi: 10.1002/gch2.202400267

[4] B. Chen, C. Zou, Y. Zhang, C. Gou, and J. Li, “The current status, opportunities, challenges and coping strategies of sustainable agriculture,” Discover Sustainability, vol. 6(1282), pp. 1–21, 2025, doi:10.1007/s43621-025-02100-0

[5] V. Kumar, K.V. Sharma, N. Kedam, A. Patel, T.R. Kate, and U. Rathnayake, “A comprehensive review on smart and sustainable agriculture using IoT technologies,” Smart Agricultural Technology, vol. 8, pp. 1–22, 2024, doi:10. 1016/j.atech.2024.100487

[6] O. Rozenstein et al., “Data-driven agriculture and sustainable farming: Friends or foes?” Precision Agr., vol. 25, pp. 520–531, 2024, doi:10.1007/s11119-023-10061-5J

[7] A. Naser, M. Shmoon, T. Shakeel, S.U. Rehman, A. Ahmad, and V. Gruhn, “A systematic literature review of the IoT in agriculture - Global adoption, innovations, security, and privacy challenges,” IEEE Access, vol. 4, pp. 60986–61021, doi:10.1109 /ACCESS.2024.3394617

[8] J. W. Doran and M. R. Zeiss, “Soil health and sustainability: Managing the biotic component of soil quality,” Applied soil ecology, vol. 15(1), pp. 3–11, 2000, doi:10.1016/S0929-1393(00)00067-6.

[9] J. A. Harris, D. L. Evans, and S. J. Mooney, “A new theory for soil health,” European Journal of Soil Science, vol. 73(4), pp. 1–7, 2022, doi:10.1111/ejss.1329225

[10] J. Lehmann, D. A. Bossio, I. K. Knabner, and M. C. Rillig, “The concept and future prospects of soil health,” Nature

Reviews Earth & Environment, vol. 1(10), pp. 544–553, 2020, doi: 10.1038/s43017-020-0080-8

[11] H. Deshmukh, H. Deshpande, and B.R. Arunkumar, "Advances in soil health monitoring: A review of digital and sensor based tools," Int. J. of Plant & Soil Science, vol. 37(11), pp. 72–89, 2025, doi:10.9734/ijpss/2025/v37i115825

[12] C. Cariou, L. Moiroux-Arvis, F. Pinet, and J. P. Chanet, "Internet of Underground Things in agriculture 4.0: Challenges, applications and perspective," Sensors, vol. 23(8), pp. 1–21, 2023, doi:10.3390/s23084058

[13] M. C. Vuran and A. R. Silva, "Communication through soil inwireless underground sensor networks - Theory and practice," Sensor Networks, pp. 309–347, 2009, doi:10.1007/978-3-642-01341-6_12

[14] C. Cariou, L. Moiroux-Arvis, F. Bendali, Y. Hu, and J. Mailfert, "Unmanned aerial vehicle optimal route planning for data collection of underground communicating sensor nodes in agriculture," J. on Autonomous Transportation Systems, vol. 3(1), pp. 1–17, 2025, doi: 10.1145/3748732

[15] S. Gopalakrishnan et al., "A biodegradable chipless sensor forwireless subsoil health monitoring," Scientific reports, vol. 12, pp. 1–14, 2022, doi:10.1038/s41598-022-12162-z

[16] J. Linford and M. Haghshenas-Jaryani, "A ground robotic system for crops and soil monitoring and data collection in New Mexico chile pepper farms," Discover Agriculture, vol. 2(101), pp. 1–26, 2024, doi:10.1007/s44279-024-00113-3

[17] H. B. Klopfenstein and A. Lussier-Desbiens, "Terra-22: An aerial soil sampling in densely compacted agricultural fields," Drone Systems and Applications, vol. 12, pp. 1–14, 2024, doi:10.1139/dsa-2023-0010

[18] C. Jiang, K. Miao, Z. Hu, F. Gu, and K. Yi, "Image recognition technology in smart agriculture: A review of current applications challenges and future prospects," Processes, vol. 13, pp. 1–31, 2025, doi:10.3390/pr13051402

[19] A. Fundurulic, J. M. S. Faria, and M. L. Inacio, "Advances in electronic nose sensors for plant disease and pest detection," Engineering Proceedings, vol. 48(13), pp. 1–6, 2023, doi: 10.3390/CSAC2023-14890

[20] S. P. Heyram, P. K. Sajeesh, P. S. Kurian, A. S. Bhavana, and L. Sabu, "E-Nose technology: An eminent tool for early detection of plant diseases," Journal of Scientific Research and Reports, vol. 1(10), pp. 379–396, 2025, doi: 10.9734/jsrr/2025/v31i103580

[21] T. Huttnerova, S. Paczkowski, T. Neubert, A. Jirosova, and P. Surovy, "Comparison of individual sensors in the electronic nose for stress detection in forest stands," Sensors, vol. 23, pp. 1–16, 2023, doi:10.3390/s23042001

[22] C. Kremen and A. Miles, "Ecosystem services in biologically diversified versus conventional farming systems: Benefits, externalities, and trade-offs," Ecology & Society, vol. 17(4), pp. 1–25, 2012, doi:10.5751/ES-05035-170440

[23] S. Alberti, G. Stasolla, S. Mazzola, L. P. Casacci, and F. Barbero, "Bioacoustic IoT sensors as next-generation tools for monitoring: Counting flying insects through buzz," Insects, vol. 14(924), pp. 1–15, 2023, doi:10.3390/insects14120924

[24] A. B. Kohlberg, C. R. Myers, and L. L. Figueroa, "From buzzes to bytes: A systematic review of automated bioacoustics models used to detect, classify and monitor insects," Journal of Applied Ecology, vol. 61(6), pp. 1–13, 2024, doi:10.1111/1365-2664.14630

[25] R. Mankin, D. Hagstrum, M. Guo, P. Eliopoulos, and A. Njoroge, "Automated applications of acoustics for stored product insect detection, monitoring, and management," Insects, vol. 12, pp. 1–13, 2021, doi:10.3390/insects12030259

[26] G. Dufil, I.B. Wojcik, A.A. Moreira, and E. Stavrinidou, "Plant bioelectronics and biohybrids: The growing contribution of organic electronic and carbon-based materials," Chemical Reviews, vol. 122, pp. 4847–4883, 2022, doi: 10.1021/acs.chemrev.1c00525

[27] J. M. Nassar, S. M. Khan, D. R. Villalva, M. M. Nour, A. S. Almuslem, and M.M. Hussain, "Compliant plant wearables for localized microclimate and plant growth monitoring," NPJ Flexible Electronics, vol. 2(24), pp. 1–12, 2018, doi:10.1038/s41528-018-0039-8

[28] Y. Zhao et al., "Multifunctional stretchable sensors for continuous monitoring of long-term leaf physiology and microclimate," Omega, vol. 4, pp. 9522–9530, 2019, doi:10.1021/acsome ga.9b01035

[29] M. Tei, F. Soma, E. Barbieri, Y. Uga, and Y. Kawahito, "Non-destructive real-time monitoring of underground root development with distributed fiber optic sensing," Plant Methods, vol. 20(36), pp. 1–10, 2024, doi:10.1186/s13007-024-01160-z

[30] G. Rahman et al., "SoilCam: A fully automated minirhizotron using multispectral imaging for root activity monitoring," Sensors, vol. 20(3), pp. 1–17, 2020, doi: 10.3390/s20030787

[31] M. Lacoste, S. Ruiz, and D. Or, "Listening to earthworms burrowing and roots growing - acoustic signatures of soil biological activity," Scientific Reports, vol. 8, pp. 1–9, 2018, doi:10.1038/s41598-018-28582-9

[32] M. S. M. Rafi, M. Behjati, and A. S. Rafsanjani, "Reliable and cost efficient IoT connectivity for smart agriculture: A comparative study of LPWAN, 5G, and hybrid connectivity models," arXiv preprint, pp. 1–23, 2025, doi: 10.48550/arXiv.2503.11162

[33] T. Adiprabowo et al., "Satellite technology for Internet of Things: An overview," Iota, vol. 5(1), pp. 1–11, 2025, doi:10.31763/iota.v5i1.758

[34] P. Wang, "Ultra-low-power and high-sensitivity wake-up receivers for IoT applications," San Diego Elec. thesis, 2020

[35] A. Ali et al., "Advancements in energy harvesting techniques for sustainable IoT devices," Results in Engineering, vol. 26(1), pp. 1–15, 2025. doi:10.1016/j.rineng.2025.104820

[36] S. N. Arinze, E. R. Obi, S. H. Ebenuwa, and A. O. Nwajana, "RF energy-harvesting techniques: Applications, recent developments, challenges, and future opportunities," Telecom, vol. 6(45), pp. 1–40, 2025, doi:10.3390 /telecom6030045

[37] F. Meder, G. A. Naselli, and B. Mazzolai, "Wind dynamics and leaf motion: Approaching the design of high-tech devices for energy harvesting for operation on plant leaves," Frontiers in Plant Sciences, vol. 13, pp. 1–14, 2022. doi:10.3389/fpls.2022.994429

[38] Y. Feng et al., "Green plant-based triboelectricity system for green energy harvesting and contact warning," EcoMat, vol. 3(6), pp. 1–9, 2021, doi:10.1002/eom2.12145

[39] L. Moiroux-Arvis, C. Cariou, and J. Chanet, "Evaluation of LoRa technology in 433-MHz and 868-MHz for underground to aboveground data transmission," Computers and Electronics in Agriculture, vol. 194, pp. 1–12, 2022, doi: 10.1016/j.compag.2022.10677

Using Giant Magneto-Impedance Effect for Transportation

Valentina Zhukova, Pablo Rodríguez Jiménez
Dept. Polymers and Advanced Materials, Univ. Basque Country, EHU, 20018 San Sebastian, Spain
e-mail: valentina.zhukova@ehu.es

Rafael Garcia-Etxabe
Gaiker Technological Centre, 48170, Zamudio, Spain
e-mail: etxabe@gaiker.es

Mohamed Salaheldeen
Dept. Polymers and Advanced Materials, Univ. Basque Country, EHU, 20018 San Sebastian, Spain and Phys. Dept., Faculty of Science, Sohag University, Sohag 82524, Egypt
e-mail: mohamed.salaheldeenmohamed@ehu.eus

Arcady Zhukov
Dept. Applied Physics, Univ. Basque Country, EIG, EHU, 20018, San Sebastian, and Ikerbasque, Basque Foundation for Science, Spain
e-mail: arkadi.joukov@ehu.es

***Abstract*— Ferromagnetic amorphous microwires exhibit magnetic properties, as well as Giant magneto-Impedance (GMI) which are sensitive to external stimuli, such as stress or heating, making them suitable for the development of various sensors. On the other hand, the use of Taylor-Ulitovsky fabrication technique allows to produce such microwires covered with insulating flexible glass coating and with the widest range of diameters (from 0.1 to 100 μm). We provide experimental results on dependencies of the hysteresis loops and GMI effect of glass-coated microwires on external stimuli. The obtained results are considered as a base for a novel sensing technique allowing non-destructive and non-contact monitoring utilizing ferromagnetic glass-coated microwire for various applications, such as transportation (aircraft, automobile and railroad sectors).**

***Keywords - giant magnetoimpedance effect; magnetic microwires; magnetic softness; smart composites*.**

I. INTRODUCTION

Amorphous magnetic materials, discovered in 60-s, commonly present an unusual combination of excellent magnetic properties (e.g., high magnetic permeability, giant magnetoimpedance, GMI, effect, magnetic bistability, Matteucci and Widemann effects) together with superior mechanical properties (plasticity, flexibility) [1]-[5]. Such combination of physical properties makes them attractive for various technological applications [6]-[8]. Enhanced magnetic softness of amorphous materials is linked to the disordered structure characterized by the absence of the magnetocrystalline anisotropy and defects (dislocations, grain boundaries, etc.) typical for conventional crystalline magnets [1]-[5]. The manufacturing techniques of different types of amorphous materials involves rapid melt quenching [1]-[4]. Such fabrication techniques are generally quite fast and not expensive, allowing preparation of soft magnetic materials without any complex post-processing treatments [1]-[4].

For many applications, especially in the transport (automotive or aviation industries) or medicine, new features such as reduced size, increased corrosion resistance or biocompatibility are in high demand. Therefore, much attention is paid to the development of alternative manufacturing methods that allow obtaining amorphous materials with insulating coatings at the micro- and nanoscale using rapid quenching of the melt [6]-[8].

Glass-coated microwires fabricated by the Taylor-Ulitovsky method meet most of the above-mentioned requirements: such magnetic microwires have micro-nanometer diameters (typically 0.1-100 μm), they are covered with a thin, insulating, biocompatible and flexible glass coating [7]-[11], and can have excellent magnetic softness, high GMI effect or magnetic bistability [9]-[11].

This combination of properties of glass-coated amorphous microwires allows for development of new technological applications, such as magnetic sensors [6]-[9] [12]-[14] or smart composites with tunable magnetic permittivity [8][15].

Recently, the stress and temperature dependence of hysteresis loops and GMI effect are proposed for the development of smart composites with microwires inclusions and magnetoelastic sensors or using magnetoelastic sensors based on stress dependence of various magnetic properties [12]-[19].

In this work, we provide our results on study of the influence of stresses and temperature on GMI effect and magnetic properties of glass-coated microwires paying attention on applications in transportation industries, such as aircraft, automobile or railroad sectors.

The rest of the paper is structured as follows. In Section II, we present the experimental methods, while in Section III we describe the results on the stress and temperature dependencies of the hysteresis loops and the GMI effect of the studied microwires. The article concludes in Section IV.

II. EXPERIMENTAL DETAILS

We studied Co and Fe-rich glass-coated amorphous microwires with metallic nucleus diameters, *d*, between 15 and 40 μm prepared by the aforementioned Taylor-Ulitovsky method. Briefly, the fabrication method consists

of melting a metallic alloy ingot inside a glass (typically Duran or Pyrex) tube using a high-frequency inductor, forming the glass capillary from softened glass, drawing of such capillary filled with the molten metallic alloy and winding of the solidified glass-coated microwires onto a rotating bobbin [9][10].

The hysteresis loops were measured by the fluxmetric method using a specially designed setup for studying soft magnetic microwires of reduced diameter [20]. To avoid the error associated with precise evaluation of the magnetic nucleus diameter we represented the hysteresis loops as the normalized magnetization M/M_o (where M_o is the magnetic moment of the samples at maximum magnetic field amplitude, H_o) versus H.

The GMI ratio, $\Delta Z/Z$, was defined using the commonly $\Delta Z/Z$ definition, as [3][4][7]:

$$\Delta Z/Z=[Z(H)-Z(H_{max})]/Z(H_{max})\cdot 100 \quad (1)$$

where Z is wire impedance, H_{max} – is the maximum applied DC magnetic field (typically below a few kA/m).

Wire impedance, Z, was experimentally measured reflection coefficient S_{11} using a vector network analyzer using the expression:

$$Z = Z_o \frac{(1+S_{11})}{(1-S_{11})} \quad (2)$$

where Z_0=50 Ohm is the characteristic impedance of the coaxial line. Use of the specially designed sample holder with coaxial line connections allows to measure $Z(H)$ dependencies up to GHz frequencies [21].

For wireless measurements of microwire response under stress at 2.45 GHz, we used the free space measurement system, consisting of two broadband horn antennas fixed to the anechoic chamber and a vector network analyzer, previously used for the composites characterization at free space [15]. We measured the scattering S_{22}, parameter. As recently proposed [18], the AC modulating magnetic field was applied parallel to the ferromagnetic microwires to modulate the impedance in the microwire. We use the same modulation magnetic field frequency, f, of 80 Hz as in our previous studies [18].

The applied stresses value, σ, acting on the metallic nucleus has been evaluated considering different Young's moduli of the metallic alloy and the glass, E_1 and E_2 respectively, as was described earlier [22]:

$$\sigma \quad \frac{K\cdot P}{K\cdot S_m+S_{gl}} \quad (3)$$

where $k = E_2/E_1$, P - the applied mechanical load, and S_m and S_{gl} are the cross sections of the metallic nucleus and glass coating respectively.

III. EXPERIMENTAL RESULTS AND DISCUSSION

As expected from previous studies [9], as-prepared Fe–rich and Co-rich microwires present rather different hysteresis loops. As shown in Figure 1, Fe-rich ($Fe_{75}B_9Si_{12}C_4$) microwires present rectangular hysteresis loops. While, Co-rich ($Co_{65.4}Fe_{3.8}Ni_1B_{13.8}Si_{13}Mo_{1.35}C_{1.65}$) microwires present different kind of hysteresis loop with low coercivity and high initial permeability. From the hysteresis loops, we can evaluate the coercivity, H_c, and the switching field, H_s (for the case of rectangular hysteresis loops, see Figure 1a) and magnetic anisotropy field, H_k (for the case of linear hysteresis loops, Figure 1b). It is worth mentioning that H_c, H_s and H_k – values are significantly affected by magnetic field frequency, f, and amplitude, H_o [23]. Therefore, all the measurements have been performed at fixed f (100 Hz) and H_o values.

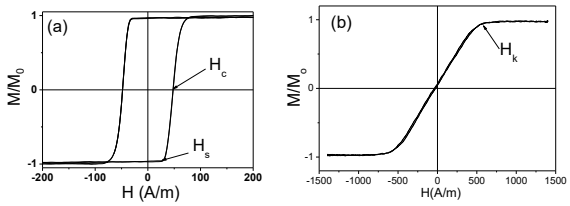

Figure 1. Typical rectangular ($Fe_{75}B_9Si_{12}C_4$ microwire) (a) and linear ($Co_{65.4}Fe_{3.8}Ni_1B_{13.8}Si_{13}Mo_{1.35}C_{1.65}$ microwire) (b) hysteresis loops of magnetic microwires illustrating definitions of H_c, H_s and H_k.

We observed that the shape of the hysteresis loops of Co-rich ($Co_{65.4}Fe_{3.8}Ni_1B_{13.8}Si_{13}Mo_{1.35}C_{1.65}$) microwires remains almost the same (linear with low coercivity) when stress is applied However, an increase in the magnetic anisotropy field, H_k, can be observed upon tensile stress, σ (see Figure 2b). The origin of such linear $H_k(\sigma)$ dependence was recently discussed in terms of the stress dependence of the magnetoelastic anisotropy, K_{me}, given as [24]:

$$K_{me} = 3/2\lambda_S\sigma \quad (4)$$

where λ_s is the magnetostriction coefficient.

As shown in Figure3a, when the tensile stress is applied the character of hysteresis loops of Fe-rich ($Fe_{75}B_9Si_{12}C_4$) microwires does not change, although an increase in H_c is observed. Evaluated $H_c(\sigma)$ and $H_s(\sigma)$ are shown in Figure3b. As can be appreciated, both H_c and H_s present similar tendency showing increase upon applied stress.

Previously, $H_s(\sigma)$ dependence was interpreted considering that the H_s is proportional to the energy required to form the domain wall, γ, involved in the bistable magnetization process. The domain wall energy linked with K_{me} and hence with σ and then it can be expressed as [25]:

$$H_S \propto \gamma \propto \frac{[A(3/2)\ \lambda_S(\sigma+\sigma_r)]^{1/2}}{cos\alpha} \quad (5)$$

where α is the angle between magnetization and axial direction, A is the exchange energy constant, and σ_r is the residual tensile stress. Consequently, H_s must be proportional to $\sigma^{1/2}$ for σ larger than σ_r and cos $\alpha \approx 1$.

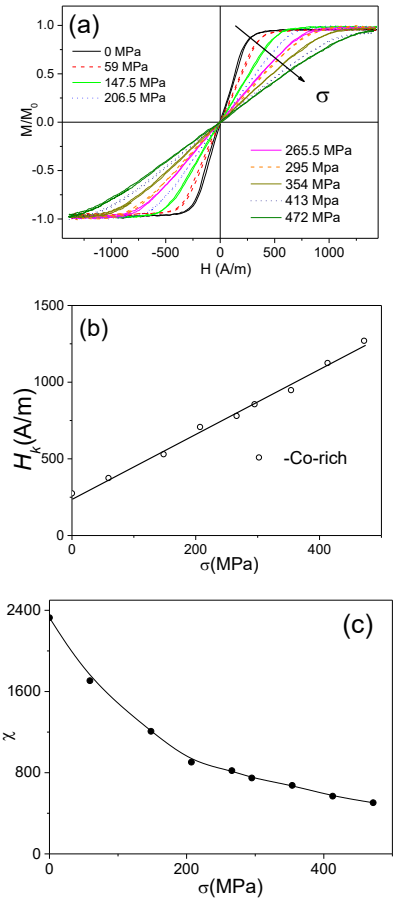

Figure 2. Effect of applied stress on hysteresis loops (a) $H_k(\sigma)$ dependence (b) and $\chi(\sigma)$ (c) of $Co_{65.4}Fe_{3.8}Ni_1B_{13.8}Si_{13}Mo_{1.35}C_{1.65}$ microwires.

The experimentally observed $H_s(\sigma)$ and $H_c(\sigma)$ dependencies better fits to $H_c \sim\sigma^{0.74}$ and $H_s \sim\sigma^{0.58}$ (see Figure 3b). Qualitatively, a fairly good agreement is observed between the predicted and experimental $H_s(\sigma)$ and $H_c(\sigma)$ dependencies.

The observed difference in predicted and experimentally observed $H_c(\sigma)$ and $H_s(\sigma)$ dependencies must be attributed to complex internal stresses [26]. Additionally, although the origin of the switching field, H_s, is linked with the domain wall nucleation or depinning processes, the coercivity, H_c, is also affected by the velocity of the propagating domain wall [23].

Influence of temperature on hysteresis loops of Fe-rich and Co-rich microwire is shown in Figure 4. It is remarkable that upon heating the hysteresis loops of Fe-rich microwires become essentially non-rectangular. Rectangular hysteresis loop transforms into inclined upon heating (with an increase in T). The opposite tendency is observed for Co-rich microwires: upon heating the hysteresis loops becomes almost rectangular (see Figure 4b).

Accordingly, the GMI effect is also affected substantially by temperature (see Figure 5). An increase in $\Delta Z/Z$–value is observed for Fe-rich microwire being most

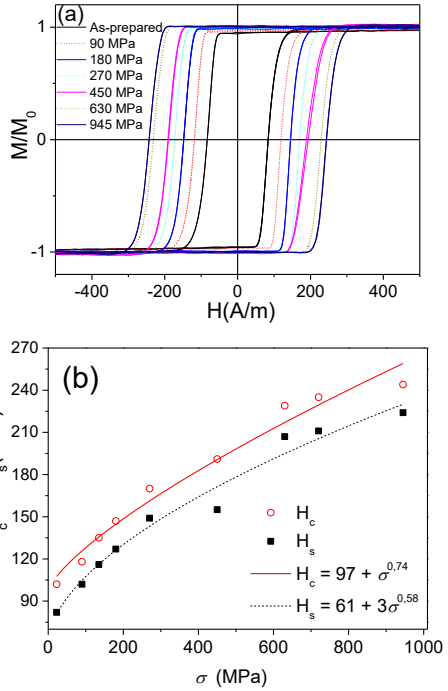

Figure 3. Effect of applied stresses on hysteresis loops (a) and $H_c(\sigma)$ and $H_s(\sigma)$ dependencies (b) of $Fe_{75}B_9Si_{12}C_4$ microwires. The experimental $H_s(\sigma)$ and $H_c(\sigma)$dependencies are compared with fitting considering $H_c(\sigma=0)$=97 A/m and $H_s(\sigma=0)$ =61 A/m.

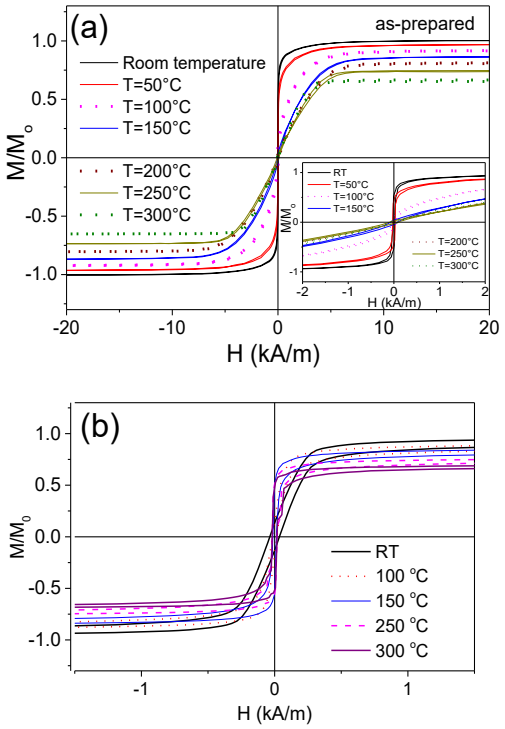

Figure 4. Hysteresis loops of Fe-rich (a) and Co-rich (b) microwire measured at different T.

remarkable at T= 300 °C: Maximum GMI ratio, $\Delta Z/Z_{max} \approx$ 120% is recorded at T= 300 °C (100 MHz) (Figure 5a). While

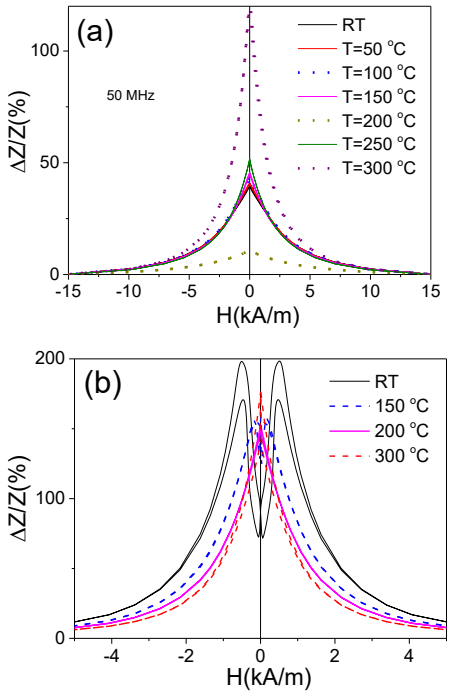

Figure 5. *ΔZ/Z(H)* dependencies of Fe-rich (a)and Co-rich (b) microwires measured at 50 MHz at various temperatures.

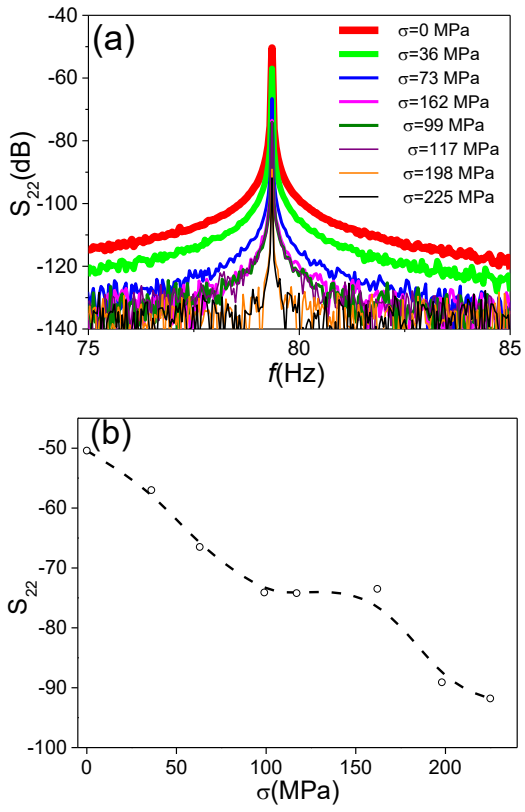

Figure 6. Frequency Spectrum of S_{22} module (a) and effect of applied stress on amplitude of the 1st harmonic (fundamental, 80 Hz) of S_{22} at different σ-values (b).

in Co-rich microwire the opposite tendency (a decrease in $\Delta Z/Z_{max}$ upon heating) is observed (see Figure 5b).

As described above, we measured the influence of applied stress, σ, on microwave signal of single microwire. A low frequency AC magnetic field (80 Hz) was applied by a planar coil placed inside the anechoic chamber. Using the VNA we measured the S_{22} parameters at 2.45 GHz at different σ -values. The S_{22} (σ) dependence is provided in Figure 6a. A substantial decay of the S_{22} parameter measured at 2.45 GHZ is observed (see Figure 6a). The dependence of S_{22} on σ, evaluated from Figure 6a, is provided in Figure 6b. From Figure 6b is evident that upon the applied stress from 0 to 225 MPa, S_{22} changes on 40 dB (100 times) from -50 to -90 dB.

The observed substantial $S_{22}(\sigma)$ dependence can be explained considering the $\chi(\sigma)$ dependence provided in Figure2c.

The observed dependencies of magnetic properties, GMI effect and even S_{22} at microwave frequencies are potentially suitable for exciting applications in structural integrity and health monitoring related to wireless stresses monitoring and integrity in civil engineering, aircraft and automobile industries.

Certainly, contactless stress monitoring in carbon fiber composite materials for the aircraft industry is vital to the safety of modern aircrafts. In these applications glass-coated microwires inclusions with high GMI effect embedded in composites with enhanced corrosion resistance and mechanical properties are responsible for remote stresses or temperature monitoring in aircraft and car industries [18][27].

The peculiarity of the composites used for aircraft industry is the presence of the carbon fibers making such composites conductive. Therefore, further developments were needed to separate the microwave response of magnetic microwires from that of conductive carbon fibres. Recently, this problem has been successfully solved using a low frequency modulated magnetic field [18]. For such applications, high GMI effect and high stress sensitivity of the microwave response of magnetic microwires are essentially relevant.

The main advantage of the microwave stress and temperature monitoring (using *S*- parameters) is the possibility of contactless measurements at large distance to the microwire [8][27][28]. Additionally, the changes in S_{22}- parameter are rather large (see Figure 6). In contrast, changes in H_c and H_s are smaller (see Figure 3). Additionally, the distance to such magnetically bistable microwire is usually limited to a few cm [29]. However, the low frequency measurements (such as dependence of coercivity on external stimuli) are less affected by the matrix conductivity.

IV. CONCLUSIONS AND FUTURE WORK

We demonstrated that magnetic properties, GMI effect and microwave signal produced by ferromagnetic

microwires are substantially affected by mechanical stress and heating.

The obtained experimental results yield new and important insights suitable for development of sensing technique for non-destructive and non-contact monitoring of the composites containing embedded microwire inclusions for aircraft, automobile industries.

ACKNOWLEDGMENT

This work was supported by Spanish MCIU under PGC2018-099530-B-C31 (MCIU/AEI/FEDER, UE) by EU under "Harmony" (HORIZON-CL4-2023-RESILIENCE-01) project and by the Government of the Basque Country under Elkartek (ATLANTIS and MOSINCO) projects. The authors are thankful for the technical and human support provided by SGIker of UPV/EHU (Medidas Magnéticas Gipuzkoa) and European funding (ERDF and ESF).

REFERENCES

[1] J. Durand, "Magnetic Properties of Metallic Glasses" in Topics in Applied Physics Volume 53, 1983, Glassy Metals II. Atomic Structure and Dynamics, Electronic Structure, Magnetic Properties, Editors: H. Beck and H.-J. Giintherodt, Springer-Verlag, Berlin Heidelberg New York Tokyo.

[2] G. Herzer, Amorphous and Nanocrystalline Materials, in: Encyclopedia of Materials: Science and Technology, pp. 149–157, Elsevier Science Ltd., 2001, ISBN: 0-08-0431526.

[3] A. P. Zhukov, "The remagnetization process of bistable amorphous alloys", Mater. Design, vol. 5, pp. 299-305, 1993.

[4] M. Hagiwara, A. Inoue, and T. Masumoto, "Mechanical properties of Fe–Si–B amorphous wires produced by in-rotating-water spinning method", Metall. Trans. A vol. 13, pp. 373-382, 1982.

[5] T. Goto, M. Nagano, and N. Wehara, "Mechanical properties of amorphous Fe80P16C3B1 filament produced by glass-coated melt spinning", Trans. JIM, vol. 18, pp. 759-764, 1997.

[6] D. Kozejova et al., "Biomedical applications of glass-coated microwires", J. Magn. Magn. Mater., vol. 470, pp. 2-5, 2019.

[7] A. F. Cobeño et al., "Magnetoelastic sensor based on GMI of amorphous microwire", Sens. Actuators A, vol. 91, pp. 95-98, 2001.

[8] L. Panina, M. Ipatov, V. Zhukova, J. Gonzalez, and A. Zhukov, "Tuneable composites containing magnetic microwires", ch. 22, pp.431-460 DOI: 10.5772/21423 in Book: Metal, ceramic and polymeric composites for various uses, Edited by John Cuppoletti, 2011, DOI: 10.5772/1428 ISBN: 978-953-307-353-8 (ISBN 978-953-307-1098-3) InTech - Open Access Publisher (www.intechweb.org), Janeza Trdine, 9, 51000 Rijeka, Croatia.

[9] V. Zhukova et al., "Development of Magnetically Soft Amorphous Microwires for Technological Applications", Chemosensors, vol. 10, p. 26, 2022.

[10] H. Chiriac, S. Corodeanu, M. Lostun, G. Ababei, and T.-A. Óvári, "Rapidly solidified amorphous nanowires", J. Appl. Phys., vol. 107, 09A301, 2010.

[11] P. Corte-Leon et al., "The effect of annealing on magnetic properties of "Thick" microwires", J.Alloys Compounds vol. 831, p.150992,2020, doi: https://doi.org/10.1016/j.jallcom.2019.06.094

[12] A. Zhukov et al., "Magnetoelastic sensor of level of the liquid based on magnetoelastic properties of Co-rich microwires", Sens. Actuat. A Phys., vol 81, no. 1-3, pp.129-133, 2000.

[13] A. Talaat et al., "Ferromagnetic glass-coated microwires with good heating properties for magnetic hyperthermia", Sci. Reports, vol. 6, p. 39300, 2016.

[14] M. Churyukanova et al., "Non-contact method for stress monitoring based on stress dependence of magnetic properties of Fe-based microwires", J. Alloys Compd., vol. 748(5) pp. 199-205, 2018.

[15] D. Makhnovskiy, A. Zhukov, V. Zhukova, and J. Gonzalez, "Tunable and self-sensing microwave composite materials incorporating ferromagnetic microwires", Advances in Science and Technology, vol. 54, pp. 201-210, 2008.

[16] D. Praslička et al., "Possibilities of Measuring Stress and Health Monitoring in Materials Using Contact-Less Sensor Based on Magnetic Microwires", IEEE Trans. Magn., vol. 49(1), pp. 128-131, 2013.

[17] A. Allue et al., "Smart composites with embedded magnetic microwire inclusions allowing non-contact stresses and temperature monitoring", Compos. Part A Appl., vol. 120, pp. 12-20, 2019, DOI: 10.1016/j.compositesa.2019.02.014.

[18] V. Zhukova et al., "Free Space Microwave Sensing of Carbon Fiber Composites with Ferromagnetic Microwire Inclusions", IEEE Sens. Lett., vol. 8, No. 1, p. 2500104, 2024.

[19] P. Corte -Leon et al., "Effect of temperature on magnetic properties and magnetoimpedance effect in Fe -rich microwires", J. Alloys Compound. vol. 946, p.169419, 2023, doi: https://doi.org/10.1016/j.jallcom.2023.169419

[20] L. Gonzalez-Legarreta et al., "Optimization of magnetic properties and GMI effect of Thin Co-rich Microwires for GMI Microsensors," Sensors, vol. 20, p.1558, 2020.

[21] A. Zhukov et al., "Routes for Optimization of Giant Magnetoimpedance Effect in Magnetic Microwires", IEEE Instrumentation & Measurement Magazine, vol. 23, no. 1, pp. 56-63, 2020, doi: 10.1109/MIM.2020.8979525.

[22] V. Zhukova, M. Ipatov, and A. Zhukov, "Microwave stress monitoring using Co-rich amorphous microwire assessed by free space measurements", J. Sci.: Adv. Mater. Devices, vol.10, p.100950, 2025 doi: https://doi.org/10.1016/j.jsamd.2025.100950.

[23] A. Zhukov et al., "Frequency dependence of coercivity in rapidly quenched amorphous materials", J. Mat. Sci. Eng. A vol. 226-228, pp. 753-756, 1997.

[24] P. Corte-Leon et al., "Stress dependence of the magnetic properties of glass-coated amorphous microwires" J. Alloys Compound, vol. 789, pp. 201-208, 2019, doi: 10.1016/j.jallcom.2019.03.044

[25] P. Aragoneses et al., "The Stress dependence of the switching field in glass-coated amorphous microwires", J. Phys. D: Applied Phys. vol. 31, pp. 3040-3045, 1998.

[26] A. Zhukov et al., "Ferromagnetic resonance and Structure of Fe-based Glass-coated Microwires," J. Magn. Magn. Mater., vol. 203, pp. 238-240, 1999.

[27] M. Ipatov et al., "Tunable effective permittivity of composites based on ferromagnetic microwires with high magneto-impedance effect", Appl. Phys. A, vol. 103(3), pp. 693-697, 2011.

[28] R. Garcia-Etxabe et al., "Influence of Tensile Stress on Microwave Scattering Parameters of Continuous Ferromagnetic Microwire Embedded into Glass Reinforced Composites", IEEE Trans. Magn., vol. 61(6), p. 4001004, 2025.

[29] S. Gudoshnikov et al., "Evaluation of use of magnetically bistable microwires for magnetic labels", Phys. Status Solidi A, 208, No. 3, 526–529 (2011)/ DOI 10.1002/pssa.201026414.

Magnetic Properties and Applications of Glass-coated Ferromagnetic Microwires

Valentina Zhukova, Paula Corte-Leon
Dept. of Polymers and Advanced Materials, Univ. Basque Country, EHU, 20018 San Sebastian, Spain
e-mail: valentina.zhukova@ehu.es

Juan Maria Blanco
Dept. Applied Physics, Univ. Basque Country, EIG, EHU, 20018, San Sebastian, Spain
e-mail: arcadyzh@gmail.com

Mihail Ipatov
General Magnetic Measurement Service of Advanced Research Facilities (SGIker), University of the Basque Country, UPV/EHU, Planta -1, Avda. Tolosa 72, 20018 Donostia-San Sebastián, Spain
e-mail: mihail.ipatov@gmail.com

Arcady Zhukov
Dept. Applied Physics, Univ. Basque Country, EIG, EHU, 20018, San Sebastian, and Ikerbasque, Basque Foundation for Science, Spain
e-mail: arkadi.joukov@ehu.es

***Abstract*—The impact of post-processing on soft magnetic properties and the Giant Magneto-Impedance (GMI) effect of Fe- and Co-based glass-coated microwires is evaluated. A remarkable improvement of magnetic softness and GMI effect is observed in Fe-rich glass-coated microwires subjected to stress annealing. Frequency dependence of GMI ratio of stress-annealed Fe-rich microwires has been discussed considering frequency dependence of the skin penetration depth, δ, as well as magnetic anisotropy distribution within the metallic nucleus. Annealed and stress-annealed Co-rich microwires present rectangular hysteresis loop and single and fast domain wall propagation. However, Co-based stress-annealed microwires present high magnetoimpedance ratio. Observed stress-induced anisotropy and related changes of magnetic properties are discussed considering internal stresses relaxation and "back-stresses".**

***Keywords- Giant Magneto-Impedance effect; magnetic microwires; magnetic softness; domain wall propagation*.**

I. INTRODUCTION

Development of magnetic sensors is focused on the miniaturization of their size, improvement of their features and on finding of new materials. Among new magnetic materials, a family of thin wire with reduced dimensions recently gained considerable attention [1]. Glass-coated magnetic microwires prepared using the Taylor-Ulitovsky technique with thin metallic nucleus (typically with diameters 0.5 to 50 μm) covered by flexible, insulating and biocompatible glass are therefore quite interesting for sensor applications [2]. This technique allows preparation of the thinnest rapidly quenched wires with amorphous or crystalline structure of metallic nucleus. Good magnetic properties can be observed either in crystalline or in amorphous magnetic wires, but amorphous magnetic wires present several advantages, such as superior mechanical properties, the absence of microstructure defects (grain boundaries, crystalline texture, dislocations, point defects, etc.) [2] and hence precise post-processing is not required. Particularly, amorphous microwires can present Giant Magneto-Impedance (GMI) or magnetic bistability. In the case of glass-coated microwires the magnetoelastic anisotropy contribution becomes relevant since the preparation process involves not only the rapid quenching itself, but also simultaneous solidification of the metallic nucleus surrounded by non-magnetic glass-coating with rather different thermal expansion coefficients [2].

The purpose of this paper is to present the most recent results on tailoring of soft magnetic properties and GMI effect in glass-coated microwires paying special attention to achievement of high GMI effect and on optimization of domain wall dynamics. We also provide several examples of sensor applications of such glass-coated microwires. The rest of the paper is structured as follows. In Section II, we present the experimental methods, while in Section III we describe the results on the dependencies of hysteresis loops, domain wall dynamics and GMI effect of the studied microwires on annealing conditions.

II. EXPERIMENTAL DETAILS

We studied glass-coated amorphous microwires prepared by the Taylor-Ulitovsky method. The manufacturing technique is described elsewhere [3][4]. It involves melt quenching of the metallic alloy inside a glass capillary and winding of the solidified glass-coated microwires onto a rotating bobbin.

We measured the hysteresis loops, dynamics of domain wall propagation and GMI effect. Hysteresis loops were measured by the fluxmetric method using low frequency (100 Hz) AC magnetic field, as described elsewhere [5].

Sample impedance, Z, was determined from the reflection coefficient, S_{11}, using a vector network analyzer, as described in detail elsewhere [6]. From Z, measured at different magnetic fields, H, we evaluated the GMI ratio, $\Delta Z/Z$, as [2][7]:

$$\Delta Z/Z=[Z(H)-Z(H_{max})]/Z(H_{max})\cdot 100 \quad (1)$$

where H_{max} – is the maximum applied DC magnetic field.

In the microwires with rectangular hysteresis loop, we studied the Domain Wall (DW) dynamics using modified

Sixtus-Tonks previously described elsewhere [8][9]. The main difference of used method with respect to classical Sixtus-Tonks [10] technique is that to ensure a single DW propagation we leave one end of the studied sample outside the magnetization coil. Additionally, we employed three pick-up coils in order to avoid the multiple DW propagation [8][9]. The DW velocity, v, can be estimated as [8][9]:

$$v = \frac{l}{\Delta t} \quad (2)$$

where l is the distance between pick-up coils and Δt is the time difference between the ElectroMotive Force (EMF) peaks originated by moving DW in the pick-up coils [8][9].

III. EXPERIMENTAL RESULTS AND DISCUSSION

As already reported previously [2][4], the character of the hysteresis loops is linked to the sign and value of the magnetostriction coefficient, λ_s. Therefore, studied Co-rich and Fe-rich microwires present rather different magnetic properties and hence GMI effect: Fe-rich microwires with λ_s >0 present perfectly rectangular hysteresis loops exhibiting magnetic bistability and coercivity, H_c, of the order of 70 A/m (see Figure1a). In contrast, Co-rich microwires ($\lambda_s \approx 0$) present

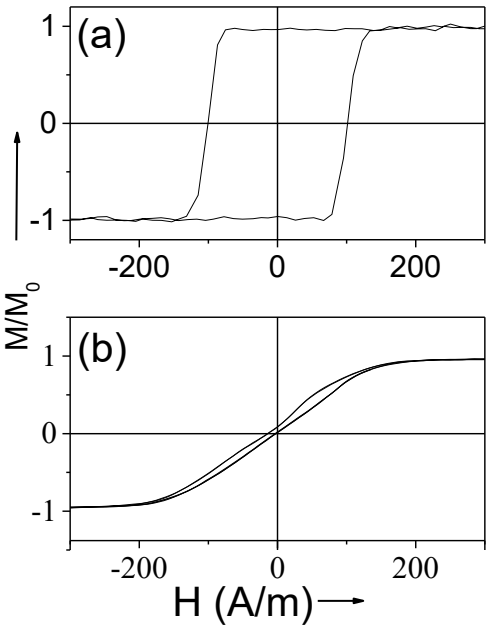

Figure1. Hysteresis loops of amorphous magnetic microwires $Fe_{75}B_9Si_{12}C_4$ (λ_s >0) (a), and $Co_{69.2}Fe_{3.6}Ni_1B_{12.5}Si_{11}Mo_{1.5}C_{1.2}$ ($\lambda_s \approx 0$) (b) microwires.

linear hysteresis loops with an order of magnitude lower H_c (see Figure1b).

As experimentally shown in dozens of previous publications [2][8][9], the remagnetization of Fe-rich microwires with rectangular hysteresis loops runs by fast domain wall, DW, propagation.

The magnetic properties of amorphous materials are mostly determined by the magnetoelastic anisotropy. The common way to reduce the magnetoelastic ansitropy is annealing. For mantaining the amorphous structure of the samples the anealing temperatures, T_{ann}, must be selected below the crystallization temeprature. Usually the crystallization of amorphous Fe- and Co-rich alloys is observed for $T_{ann} \geq 500$ ºC [11]. The crystallization usually deteriorates mechanical properties of amorphous materials [11][12]. Therefore, we tried to anneal our samples at T_{ann} <500 ºC

As shown in Figure 2, it is evident that conventional furnace annealing (without stress) does not modify the hysteresis loop character of Fe-rich microwires: both as-prepared and annealed $Fe_{75}B_9Si_{12}C_4$ samples present similar

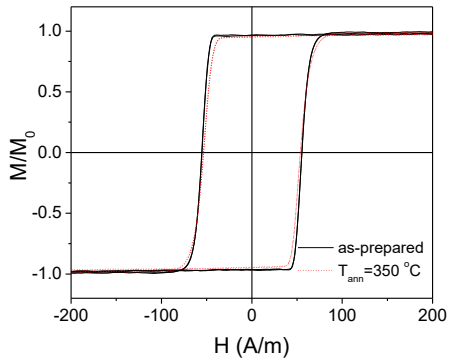

Figure 2. Hysteresis loops of as-prepared and annealed at T_{ann} = 350ºC $Fe_{75}B_9Si_{12}C_4$ microwire.

character of hysteresis loops. Only a slight decrease in H_c is observed after annealing (see Figure 2).

Roughly linear $v(H)$ dependencies are observed in studied Fe-rich microwires in the magnetic field region $H \geq H_c$ (see Figure3a)

Linear $v(H)$ dependencies have been discussed in terms of the viscous DW motion [8][9]. The DW propagates with a velocity, v, given as:

$$v=S(H-H_0) \quad (3)$$

where H_0 is the critical propagation field and S is the DW mobility given by [8][9]

$$S=2\mu_0 M_s/\beta \quad (4)$$

where μ_0 is magnetic permeability of vacuum, M_s -saturation magnetization and β is the viscous damping coefficient.

A substantial DW dynamics improvement in Fe-rich microwires after annealing is achieved (see Figure 3).

The origin of such improvement of DW dynamics, reflected by increase in v and S values is discussed elsewhere considering the dependence of DW dynamics on magnetoelastic anisotropy, K_{me}, given by [8][9][13]:

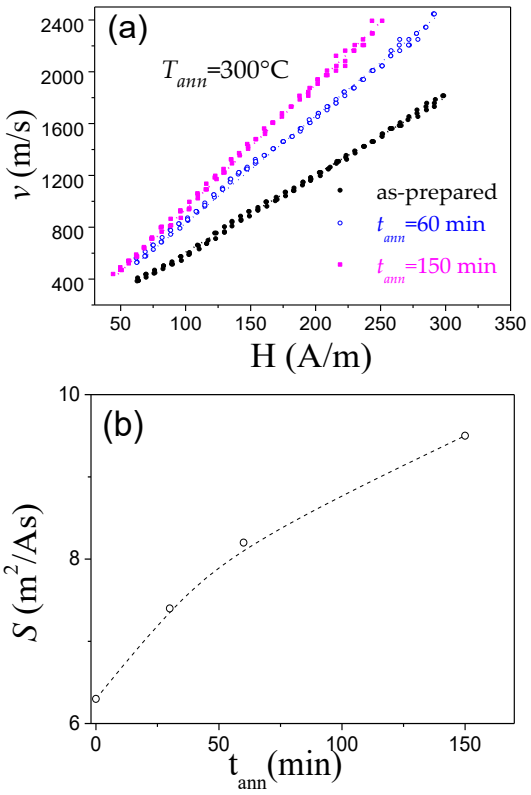

Figure 3. *v(H)* dependencies, measured in as-prepared and annealed for different annealing time, t_{ann}, $Fe_{74}B_{13}Si_{11}C_2$ microwires (a), and $S(t_{ann})$ for the same microwires annealed at 300 ºC (b).

$$K_{me} = 3/2\ \lambda_s\sigma, \qquad (5)$$

being σ–is the stresses value. In the absence of applied stresses, the internal stresses, σ_i, magnitude (and, hence, the degree of the σ_i relaxation) are essentially relevant for the DW dynamics improvement.

The magnetic relaxation damping, β_r, is considered elsewhere as the main factor affecting the DW dynamics at least in amorphous microwires [8]. The β_r is related to a delayed rotation of electron spins and inversely proportional to the domain wall width and given as [7][8]:

$$\beta_r \approx 2M_s\pi^{-1}\ (K_{me}/A)^{1/2} \qquad (6)$$

where A is the exchange stiffness constant.

Consequently, K_{me} can affect S magnitude. Accordingly, the observed change in S-values can be qualitatively explained considering σ_i relaxation [7][8].

On the other hand, upon annealing the hysteresis loop of Co-rich microwires becomes rectangular presenting considerable magnetic hardening (see Figure 4). Such unexpected behavior was explained considering two different phenomena. First of all, circular magnetic anisotropy and the remagnetiztion process by magnetization rotation of Co-rich microwires is associated to low negative λ_s –values and axial character of the internal stresses induced mostly by the difference in thermal expansion coefficients of metallic alloys and glass coating. Accordingly, the relaxation of internal stresses allows the contribution of magnetoelastic anisotropy to be reduced, while the contribution of shape anisotropy increases, facilitating axial magnetic anisotropy. Additionally, a change in the magnetostriction coefficient upon annealing is experimentally observed in several Co-rich microwires [10].

Accordingly, the hysteresis loops of annealed Co-rich microwires becomes similar to as-prepared Fe-rich

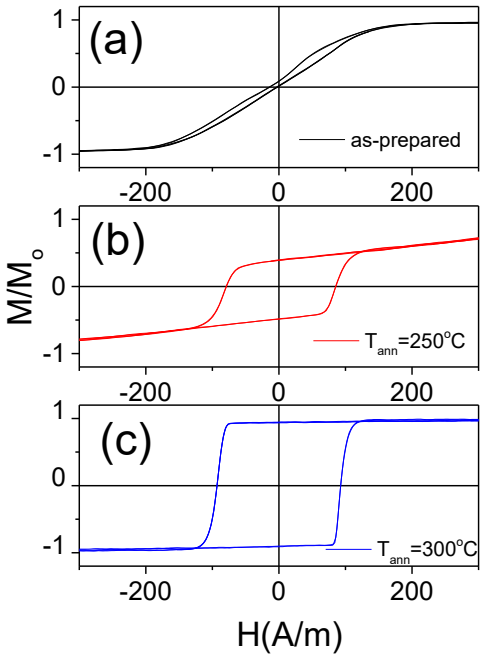

Figure 4. Hysteresis loop of as-prepared (a) and annealed at T_{ann}=250ºC (b) and 300ºC (c) $Co_{69.2}Fe_{3.6}Ni_1B_{12.5}Si_{11}Mo_{1.5}C_{1.2}$ microwires.

microwires (see Figure 4). Such character of hysteresis loops is usually associated with the remagnetization process through the DW propagation.

Consequently, we measured the DW propagation in the Co-rich microwires with magnetic bistability induced by annealing. Obtained *v(H)* dependence are presented in Figure 5a. Observed in studied Co-rich microwire v –values (above 2.5 km/s) are even higher that in Fe-rich microwires (see Figure3). This difference can be attributed to lower λ_s –values of Co-rich alloy.

Surprisingly, a more pronounced GMI effect is observed in annealed Co-rich microwires with higher H_c and rectangular hysteresis loops (see Figure 5b): at a fixed frequency *f,* an increase in ΔZ/Z from approximately 100% to 140% is observed (see Figure 5b). Another important feature of the observed change in the *ΔZ/Z(H)* dependence after annealing is its modification from a double-peak to a single-

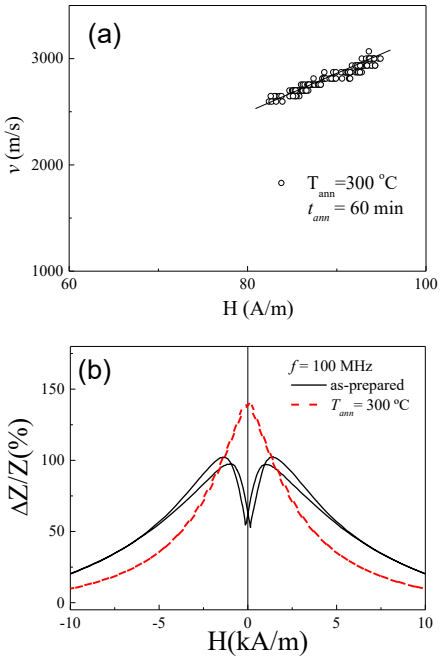

Figure 5. *v(H)* dependence in annealed $Co_{69.2}Fe_{3.6}Ni_1B_{12.5}Si_{11}Mo_{1.5}C_{1.2}$ microwire (a) and effect of annealing on *ΔZ/Z(H)* dependencies of $Co_{69.2}Fe_{3.6}Ni_1B_{12.5}Si_{11}Mo_{1.5}C_{1.2}$ microwires.

peak (see Figure 5b). It is worth noting that a double-peak Δ*Z/Z(H)* dependence is predicted for wires with transverse magnetic anisotropy, whereas a single-peak Δ*Z/Z(H)* dependence is typical for magnetic wires with axial magnetic anisotropy [14]. Accordingly, the observed change in the nature of the Δ*Z/Z(H)* dependence correlates fairly well with the observed change in the hysteresis loops after annealing.

Consequently, annealing of Co-rich microwires allows achievement of unique combination of magnetic properties. Annealed Co-rich microwires can simultaneously present single and fast Domain Wall (DW) propagation and high GMI effects.

Such combinations of magnetic properties can be suitable for various applications, such as magnetic sensors, smart composites with magnetic wire inclusions or magnetic memory devices [15]-[22]. Additionally, annealing can provide better time and temperature stability of properties of magnetic microwires.

For the results presented above, the annealing time was always 1 h, as is commonly used in most published works devoted to the effect of annealing on the magnetic properties of amorphous materials [1][5]. Such annealing time selection allows better comparison of obtained results with existing knowledge. However, annealing time is also another relevant parameter. Thus, it has been shown previously [23] that isothermal annealing with annealing time as a parameter allows for finer tuning of the hysteresis loops of Co-rich microwires. On the other hand, annealing at elevated temperatures and/or for extended times can cause crystallization of amorphous materials, resulting in a significant deterioration of their magnetic and mechanical properties [12]. Therefore, annealing conditions should be chosen with caution.

IV. Conclusion and Future Work

We demonstrated that magnetic properties, GMI effect and domain wall dynamics are substantially affected by annealing.

Obtained experimental results yield new and important insights suitable for development of material with unique combination of magnetic properties suitable for high performance magnetic sensors and devices.

Acknowledgment

This work was supported by Spanish MCIU under PGC2018-099530-B-C31 (MCIU/AEI/FEDER, UE) by EU under “Harmony” (HORIZON-CL4-2023-RESILIENCE-01) project and by the Government of the Basque Country under Elkartek (ATLANTIS and MOSINCO) projects. The authors thank for technical and human support provided by SGIker of UPV/EHU (Medidas Magnéticas Gipuzkoa) and European funding (ERDF and ESF).

References

[1] G. Herzer, Amorphous and Nanocrystalline Materials, in: Encyclopedia of Materials: Science and Technology, pp. 149–157, Elsevier Science Ltd. (2001) ISBN: 0-08-0431526.

[2] V. Zhukova et al., “Development of Magnetically Soft Amorphous Microwires for Technological Applications”, Chemosensors, vol. 10, p. 26, 2022.

[3] H. Chiriac, S. Corodeanu, M. Lostun, G. Ababei, and T.-A. Óvári, “Rapidly solidified amorphous nanowires”, J. Appl. Phys., vol. 107, 09A301, 2010.

[4] T. Goto, M. Nagano, and N. Wehara, “Mechanical properties of amorphous Fe80P16C3B1 filament produced by glass-coated melt spinning”, Trans. JIM, vol. 18, pp. 759-764, 1997.

[5] L. Gonzalez-Legarreta et al., “Optimization of magnetic properties and GMI effect of Thin Co-rich Microwires for GMI Microsensors,” Sensors, vol. 20, p.1558, 2020.

[6] A. Zhukov et al., “Routes for Optimization of Giant Magnetoimpedance Effect in Magnetic Microwires”, IEEE Instrumentation & Measurement Magazine, vol. 23, no. 1, pp. 56-63, 2020, doi: 10.1109/MIM.2020.8979525.

[7] L. V. Panina and K. Mohri, “Magneto-impedance effect in amorphous wires”, Appl Phys Lett. vol. 65, pp. 1189-1191, 1994.

[8] V. Zhukova, J. M. Blanco, M. Ipatov, and A .Zhukov, Magnetoelastic contribution in domain wall dynamics of amorphous microwires, *Physica B* vol. 407, 1450-1454, 2012.

[9] V. Zhukova et al., “Review of Domain Wall Dynamics Engineering in Magnetic Microwires”, Nanomaterials vol. 10, p.2407, 2020, doi: 10.3390/nano10122407.

[10] K. J. Sixtus and L. Tonks, “Propagation of large Barkhausen discontinuities II”, Phys. Rev., vol. 42, pp. 419-435, 1932.

[11] L. Gonzalez-Legarreta et al., “Route of magnetoimpedance and domain walls dynamics optimization in Co-based microwires”, J. Alloys Compound. vol. 830, 154576, 2020, doi: https://doi.org/10.1016/j.jallcom.2020.154576.

[12] V. Zhukova et al., “Correlation between magnetic and mechanical properties of devitrified glass-coated Fe71.8Cu1Nb3.1Si15B9.1 microwires”, J. Magn. Magn. Mater. vol. 249, P1-II, 79-84, 2002.

[13] A. Zhukov, J. M. Blanco, M. Ipatov, and V. Zhukova, “Fast magnetization switching in thin wires: Magnetoelastic and defects contributions”. Sens. Lett. vol. 11 (1), pp. 170-176, 2013, doi: 10.1166/sl.2013.2771.

[14] N. A. Usov, A. S. Antonov, and A. N. Lagar`kov, “Theory of giant magneto-impedance effect in amorphous wires with different types of magnetic anisotropy”, J. Magn. Magn. Mater., vol. 185, pp. 159-173, 1998.

[15] Y. Honkura, “Development of amorphous wire type MI sensors for automobile use”, J. Magn. Magn. Mater. vol. 249, pp. 375-381, 2002.

[16] T. Uchiyama, K. Mohri, and Sh. Nakayama, “Measurement of Spontaneous Oscillatory Magnetic Field of Guinea-Pig Smooth Muscle Preparation Using Pico-Tesla Resolution Amorphous Wire Magneto-Impedance Sensor”, IEEE Trans. Magn., vol. 47**,** pp. 3070-3073, 2011.

[17] D. Makhnovskiy, A. Zhukov, V. Zhukova, and J. Gonzalez, “Tunable and self-sensing microwave composite materials incorporating ferromagnetic microwires”, Advances in Science and Technology, vol. 54, pp. 201-210, 2008.

[18] D. Praslička et al., “Possibilities of Measuring Stress and Health Monitoring in Materials Using Contact-Less Sensor Based on Magnetic Microwires”, IEEE Trans. Magn., vol. 49(1), pp. 128-131, 2013.

[19] A. Allue et al., “Smart composites with embedded magnetic microwire inclusions allowing non-contact stresses and temperature monitoring”, Compos.Part A Appl., vol. 120, pp. 12-20, 2019, DOI: 10.1016/j.compositesa.2019.02.014

[20] V. Zhukova et al., “Free Space Microwave Sensing of Carbon Fiber Composites With Ferromagnetic Microwire Inclusions”, IEEE Sens. Lett., vol. 8, No. 1, p. 2500104, 2024.

[21] D. A. Allwood, G. Xiong, C. C. Faulkner, D. Atkinson, D. Petit, and R.P. Cowburn, “Magnetic domain-wall logic”, Science, vol. 309, pp. 1688-1692, 2005.

[22] S. Parkin, S.-H. Yang, Memory on the racetrack. Nat. Nanotechnol., vol. 10, pp. 195-198, 2015.

[23] A. Zhukov, A. Talaat, J. M. Blanco, M. Ipatov, and V. Zhukova, “Tuning of magnetic properties and GMI effect of Co-based amorphous microwires by annealing”, J. Electr. Mater., vol. 43(12), pp. 4532-4539, 2014, doi: 10.1007/s11664-014-3348-2.

Neuromorphic Approach to Micro-Particle Tracking

Javier Ramos[1], Joan Ferri[1], Fernando Pardo-Carpio[2], José A. Boluda[2], Càndid Reig[1], Teresa Serrano-Gotarredona[3], Bernabé Linares-Barranco[3]

[1] Department of Electronic Engineering, University of Valencia, Burjassot, Spain
[2] Department of Computer Science, University of Valencia, Burjassot, Spain
[3] Instituto de Microelectrónica de Sevilla (IMSE-CNM), Sevilla, Spain

e-mail: javier.ramos@uv.es, jofemon4@alumni.uv.es, fernando.pardo@uv.es
jose.a.boluda@uv.es, candid.reig@uv.es, teresa.serrano@csic.es
bernabe@imse-cnm.csic.es

***Abstract*— The tracking and analysis of moving micro-particles is a demanding task in fields such as industrial processing and biotechnology. Traditional methods rely on conventional frame-based cameras (Charge-Coupled Device (CCD) or Complementary Metal-Oxide Semiconductor (CMOS)) and post-processing software, which often face limitations regarding data volume and processing speed as particle count or velocity increases. This paper explores a neuromorphic approach using event-driven vision sensors, specifically Dynamic Vision Sensors (DVS) and Selective-Change-Driven (SCD) sensors. Unlike traditional systems, these sensors detect local changes in luminance asynchronously, providing high temporal resolution with significantly lower data flow. We present preliminary evidence of micro-particle tracking using several non-commercial, home-developed event-driven cameras integrated into a microfluidic experimental setup.**

Keywords- Selective-Change-Driven (SCD); Dynamic Vision Sensor (DVS); microfluidic; Particle Image Velocimetry (PIV); Particle Tracking Velocimetry (PTV).

I. INTRODUCTION

The tracking and analysis of moving micro-particles is a demanding task in fields as diverse as industrial processing and biotechnological activities. The classical approach relies on conventional frame-based cameras (CCD or CMOS) and post-processing software to perform Particle Tracking Velocimetry (PTV) or Particle Image Velocimetry (PIV) [1][2]. Recently, these methods have been adapted for microfluidic applications such as Microparticle Tracking Velocimetry (uPTV) [3] and Microparticle Image Velocimetry (uPIV) [4] using time-lapse microscopy. Microfluidic systems rely on diverse microfabrication techniques (such as semiconductor processing, micro-machining and additive manufacturing) [5] to create micrometer-scale structures. For basic microchannel studies, particles are injected using a syringe pump and monitored via a microscope coupled with a camera, although future diagnostic applications aim for fully integrated, compact systems.

To overcome the limitations of actual µPTV/µPIV algorithms (such as high computational cost and noise sensitivity) various Artificial Neural Network (ANN) algorithms [6] are increasingly used. Applications range from stereoscopic tracking velocimetry using Stochastic Neural Network (StochNN) [7] and Convolutional Neural Network (CNN) have been used in particle identification [8] to unsupervised feature extraction [9]. In any case, as the number or speed of tracked particles increases, various limitations arise, both in terms of detection (streaks and shadows in images) and processing (given the large amount of data generated), suggesting the use of more powerful approaches, such as those based on new event-based vision sensors [10].

Since the first attempt to replicate human vision in silicon [11], neuromorphic vision sensors (also called Event-Driven, ED) have demonstrated their enormous potential to outperform traditional frame-based systems in terms of energy, resources, and processing speed [12]. These advantages are especially important in fields where high processing speed and very high data rates are required, such as unmanned aerial vehicle (drone/UAV) guidance [13] or multiple particle tracking [14]. While several ED sensor families exist, DVS are currently the most industrial mature [10][15][16]. DVS detect local luminance changes asynchronously as events rather than frames, providing microsecond latency, high dynamic range and low data flow. A specific variant is the SCD sensor [17][18], which uses a Winner-Take-All (WTA) circuit [19] to output the coordinates and intensity of the most significant changes on demand. At 128×128 resolution, SCD sensors offer latencies as low as $100\,\mathrm{ns}$, making them ideal for high-speed tracking.

Event-based sensors offer three key advantages:

- Asynchronous event detections, which reduces bandwidth up to 100 times compared to conventional cameras while maintaining microsecond resolution [14][20]–[22].
- Real-time processing, enabling long-duration recordings and faster-than-real-time analysis without memory constraints [14][22].
- Robustness and flexibility, providing high dynamic range and tolerance to variable illumination in brightfield, fluorescence or high-velocity environments [20]–[22].

In this paper, we present preliminary evidence of the utilization of several non-commercial event-driven cameras for micro-particle tracking applications. The structure of the paper is as follows. In Section II, we specify the experimental setup, explaining the microfluidic components besides the specific architectures of SCD and DVS cameras used in this work. In Section III, we present and analyze the preliminary results obtained from capturing high-speed microparticle fluid. Finally, the conclusions and future work are presented in Section IV.

 ISBN: 978-1-68558-388-0

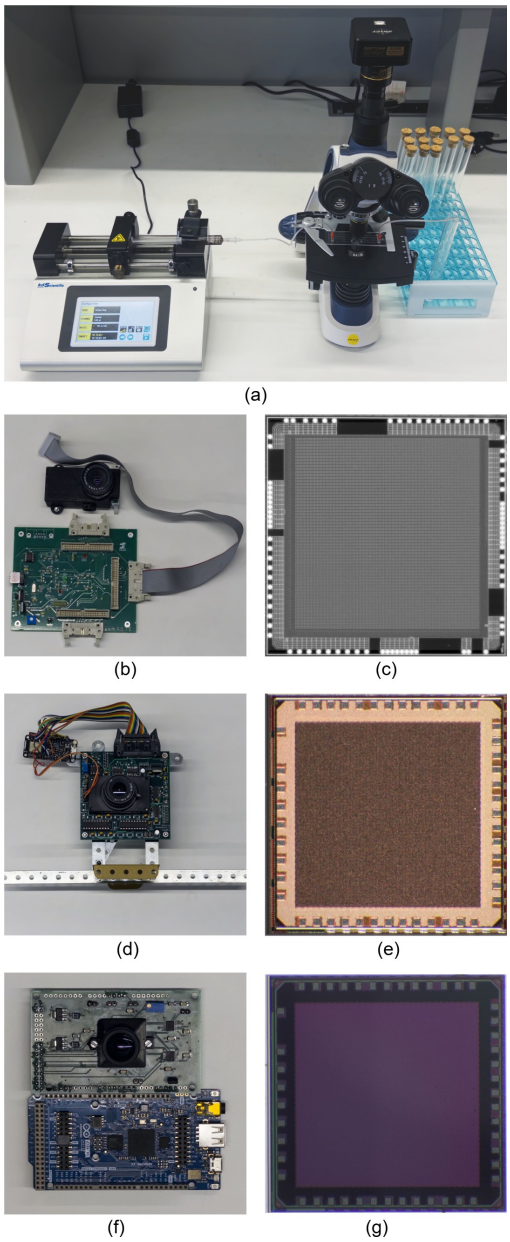

Figure 1. ED cameras and sensors considered in this study: (a) Experimental setup; (b)-(c) DVS camera and sensor; (d)-(e) SCD camera and sensor (64×64); (f)-(g) SCD camera and sensor (128×128).

II. Experimental setup

A complete experimental setup, comprising a standard microscope and a laboratory-grade syringe pump. We made use of Commercial Off-The-Shelf (COTS) single-channel microfluidic chips, and commercial microparticles were considered. To validate our proposal, we utilized home-developed SCD cameras, which were compared to a DVS camera. A conventional digital camera was used as a reference.

A. Microfluidics setup

The utilized setup is shown in Figure 1 (a). As a pump we used the KD Scientific Legato 110 which is a high-precision, single-syringe infusion and withdrawal with a volumetric accuracy of $\pm 0.5\%$ capable of hosting a broad range of syringe volumes from 0.5 μL to 60 mL, an wide range of flow rates, from less than 2 pL/min up to more than 50 mL/min. Fluidic experiments were conducted using a multi-channel thermoplastic chip (Fluidic 138, microfluidic ChipShop GmbH, Jena, Germany). The device comprises four independent straight channels, each measuring 58.5 mm in length with a cross-section of 1000 μm $\times$ 200 μm. Fluidic access was achieved via integrated Mini Luer ports, and the optical transparency of the [Polimethyl methacrylate (PMMA)/Topas] substrate permitted real-time visualization of the flow dynamics. Flow visualization was performed using fluorescent silica particles (sicastar®-redF, micromod Partikeltechnologie GmbH, Rostock, Germany) with a nominal diameter of 20 μm.

B. DVS camera

This camera is based on a 128×128 pixels DVS with improved sensitivity [23]. Each pixel in the DVS sensor individually responds to relative temporal variations of the illumination inpinging on it [24] generating asynchrounously a signed output address event when the relative variation in the illumination goes over a controllable threshold. The output address event codes the (x,y) address that identifies the pixel generating the event. An additional sign bit codes the direction (increasing or decreasing) of the illumination variation. In the sensitive DVS, a low-power low-mismatch amplification stage is added to each pixel which enables the detection of low illumination contrasts [25], making the sensor able to achieve the low noise high sensitivity conditions needed for microscopic applications.

C. SCD camera (64×64 pixels)

This camera is based on a 64×64 SCD vision sensor implemented in standard TSMC 180 nm CMOS technology [17]. It uses a continuous-time logarithmic photoreceptor and a high-speed WTA circuit to select the pixel with the greatest illumination change. The sensor delivers pixels ordered by the illumination change since they were last read, allowing for reduced data bandwidth without loss of accuracy. The sensor can operate in both SCD mode, where it selects and outputs the most changed pixels, and conventional frame-based mode. Compared to frame-based cameras, the SCD sensor can detect and track very fast-moving objects, up to 5-10 kHz, with the same time resolution for both events and illumination level.

D. SCD camera (128×128 pixels)

The sensor of this camera is a recently developed evolution of the previous one. In this case, it is implemented in standard TSMC 65 nm CMOS technology. It includes all the aforementioned characteristics, plus a double parallel WTA circuit, managing ON and OFF events. Preliminary mesurements have also evidenced its higher velocity. Frames from a standard camera are also included as a reference.

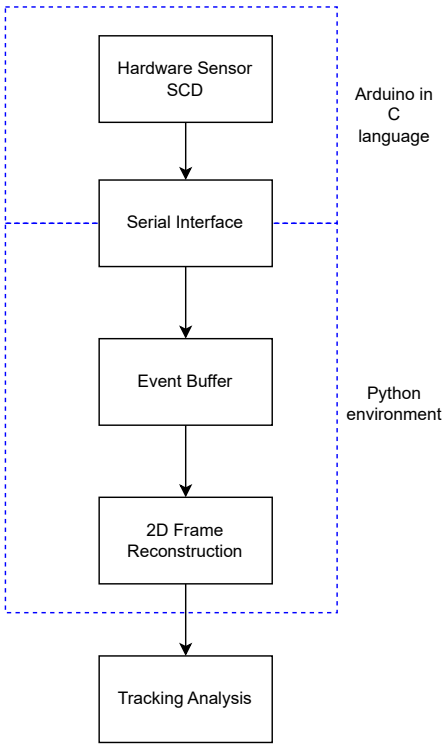

Figure 2. Flowchart describing the method for event processing.

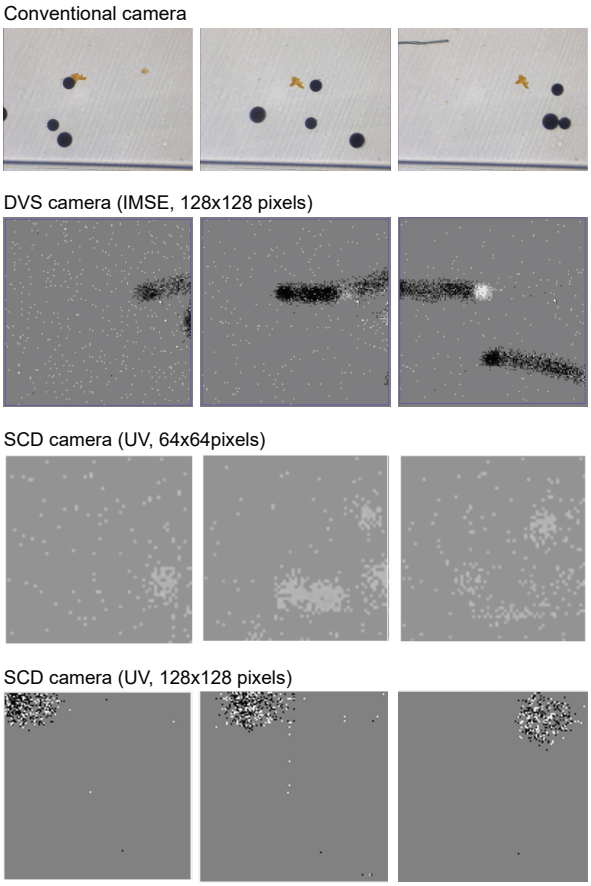

Figure 3. Events captured as frames, for better presentation.

E. Data Processing and Tracking Method

To process the data generated by the neuromorphic sensors, a real-time event-to-frame conversion pipeline is needed. For SCD cameras, the pipeline was implemented using Python as shown in Figure 2 instead of DVS cameras that uses an open-source tool called jAER viewer. Unlike conventional cameras that require high-bandwidth interfaces such as USB 2.0 or 3.0 to transmit full frames, the SCD sensors transmit event data via a standard serial port connection.

Inside the Python environment, the incoming serial event stream is buffered to reconstruct 2D frames in real-time as shown in Figure 3. Once the events are mapped into images, frame-based particle tracking methods are applied to estimate the average fluid velocity. This hardware-software design allows the system to use robust tracking algorithms while fully exploiting the sensor advantages such as high resolution and a drastic reduction in data transmission bandwidth at the hardware level.

III. Preliminary Results

We have attached the different cameras to the microscope, while maintaining an average fluid velocity of about 1.33 mm/s. Results are collected in Figure 3. As observed, the flowing particles are tracked in any case.

To facilitate the visualization and qualitative comparison of results, we have extracted frames from the events reconstruction of all cameras. As shown in Figure 3, the conventional camera is provided as a baseline reference. The camera captures the particles flow correctly, however, for a 1.33 mm/s flow, the sensor generates massive amounts of redundant data for the static microchannel background.

In contrast, the DVS camera demonstrates an advantage in extracting purely movement information. Because the DVS camera only records local temporal changes in illumination, the static background is suppressed. Figure 3 illustrates the resulting output as discrete events corresponding exactly to the particles movement. The contrast changes are precisely illustrated, mapping out high-resolution trajectory paths without the heavy data overhead of synchronous full-frame readout.

Finally, both variants of SCD sensors proved highly efficiency for high-speed micro-particle tracking under real experimental conditions. The 64×64 SCD camera successfully tracked the flow, validating the efficacy of the continuous-time logarithmic photoreceptor and WTA pixel selection despite the lower resolution. The upgraded 128×128 SCD camera obtained a markedly better spatial detail, effectively capturing the flow with minimal noise. Overall, these results verify that neuromorphic architectures can isolate high-speed moving tar-

 ISBN: 978-1-68558-388-0

gets from static backgrounds at the microscope scale producing low amount of data but rich in movement information perfectly appropriated for next-generation velocimetry algorithms.

IV. Conclusion and Future Work

This study demonstrates the viability of utilizing non-commercial event-driven cameras for micro-particle tracking applications. By integrating these sensors with a standard microscope and a microfluidic system, we successfully tracked flowing particles at an average fluid velocity of approximately 1.33 mm/s. Further experiments are required to quantify the performance of each camera.

Acknowledgments

This work has been supported by the Ministry of Digital Transformation and Civil Service under the Recovery, Transformation and Resilience Plan, funded by the European Union – NextGenerationEU, through the PERTE Chip Chairs program (Project Ref: TSI-069100-2023-0012) and by the by the Ministry of Science and Innovation (MCIN) and the State Research Agency (AEI) under the Recovery, Transformation and Resilience Plan, funded by the European Union – NextGenerationEU (Project Ref: PID2023-149071NB-C51/C53).

References

[1] M. H. Qureshi, W. H. Tien, and Y. J. P. Lin, "Performance comparison of particle tracking velocimetry (ptv) and particle image velocimetry (piv) with long-exposure particle streaks", *Measurement Science and Technology*, vol. 32, p. 024 008, 2 Dec. 2020, ISSN: 0957-0233. DOI: 10.1088/1361-6501/ABB747.

[2] M. Raffel et al., *Particle Image Velocimetry*. Springer International Publishing, 2018, ISBN: 978-3-319-68851-0. DOI: 10.1007/978-3-319-68852-7.

[3] P. Salipante, S. D. Hudson, J. W. Schmidt, and J. D. Wright, "Microparticle tracking velocimetry as a tool for microfluidic flow measurements", *Experiments in Fluids*, vol. 58, pp. 1–10, 7 Jul. 2017, ISSN: 07234864. DOI: 10.1007/S00348-017-2362-6/FIGURES/6.

[4] S. T. Wereley and C. D. Meinhart, "Recent advances in microparticle image velocimetry", *https://doi.org/10.1146/annurev-fluid-121108-145427*, vol. 42, pp. 557–576, Dec. 2009, ISSN: 00664189. DOI: 10.1146/ANNUREV-FLUID-121108-145427.

[5] N.-T. Nguyen, S. T. Wereley, and S. A. M. Shaegh, *Fundamentals and applications of microfluidics*, 3rd ed. Artech House, 2019, ISBN: 9781630813642.

[6] N. Macauley et al., "Performing particle image velocimetry using artificial neural networks: A proof-of-concept", *Measurement Science and Technology*, vol. 28, p. 125 301, 12 Nov. 2017, ISSN: 0957-0233. DOI: 10.1088/1361-6501/AA8B87.

[7] Y. Ge, S. S. Cha, and J. H. Park, "Study of particle tracking algorithms based on neural networks for stereoscopic tracking velocimetry", *Optics and Lasers in Engineering*, vol. 44, pp. 623–636, 6 Jun. 2006, ISSN: 0143-8166. DOI: 10.1016/J.OPTLASENG.2005.06.007.

[8] J. Liang et al., "Particle identification in particle tracking velocimetry using two-stage neural networks", *Journal of Industrial and Management Optimization*, vol. 19, pp. 5331–5352, 7 Jul. 2023, ISSN: 1547-5816. DOI: 10.3934/JIMO.2022175.

[9] B. T. Wolfe et al., "Unsupervised learning about 4d features of microparticle motion", *Review of Scientific Instruments*, vol. 89, 10 Oct. 2018, ISSN: 10897623. DOI: 10.1063/1.5037462/355920.

[10] G. Gallego et al., "Event-based vision: A survey", *IEEE Transactions on Pattern Analysis and Machine Intelligence*, vol. 44, pp. 154–180, 1 Jan. 2022, ISSN: 19393539. DOI: 10.1109/TPAMI.2020.3008413.

[11] M. Mahowald, "VLSI analogs of neuronal visual processing: a synthesis of form and function", Ph.D. dissertation, California Institute of Technology, 1992.

[12] D. V. Christensen et al., "2022 roadmap on neuromorphic computing and engineering", *Neuromorphic Computing and Engineering*, vol. 2, no. 2, p. 022 501, 2022. DOI: 10.1088/2634-4386/AC4A83.

[13] G. Chen et al., "Event-Based Neuromorphic Vision for Autonomous Driving: A Paradigm Shift for Bio-Inspired Visual Sensing and Perception", *IEEE Signal Processing Magazine*, vol. 37, no. 4, pp. 34–49, Jul. 2020, ISSN: 15580792. DOI: 10.1109/MSP.2020.2985815.

[14] D. Drazen, P. Lichtsteiner, P. Häfliger, T. Delbrück, and A. Jensen, "Toward real-time particle tracking using an event-based dynamic vision sensor", *Experiments in Fluids 2011 51:5*, vol. 51, no. 5, pp. 1465–1469, Sep. 2011, ISSN: 1432-1114. DOI: 10.1007/S00348-011-1207-Y.

[15] Prophesee, *Metavision technologies*, 2025.

[16] IniVation, *Neuromorphic vision systems*, 2023.

[17] F. Pardo, J. A. Boluda, and F. Vegara, "Selective change driven vision sensor with continuous-time logarithmic photoreceptor and winner-take-all circuit for pixel selection", *IEEE Journal of Solid-State Circuits*, vol. 50, pp. 786–798, 3 Mar. 2015, ISSN: 0018-9200. DOI: 10.1109/JSSC.2014.2386899.

[18] F. Pardo, B. Dierickx, and D. Scheffer, "Space-variant nonorthogonal structure cmos image sensor design", *IEEE Journal of Solid-State Circuits*, vol. 33, pp. 842–849, 6 Jun. 1998, ISSN: 00189200. DOI: 10.1109/4.678644.

[19] F. Pardo, C. Reig, J. Boluda, and F. Vegara, "A 4k-input high-speed winner-take-all (wta) circuit with single-winner selection for change-driven vision sensors", *Sensors (Switzerland)*, vol. 19, 2 2019, ISSN: 14248220. DOI: 10.3390/s19020437.

[20] Y. Ren et al., "Event-based imaging of levitated microparticles", *Applied Physics Letters*, vol. 121, p. 113 506, 11 Sep. 2022, ISSN: 00036951. DOI: 10.1063/5.0106111/2834359.

[21] C. E. Willert and J. Klinner, "Event-based imaging velocimetry: An assessment of event-based cameras for the measurement of fluid flows", *Experiments in Fluids 2022 63:6*, vol. 63, pp. 101–, 6 Jun. 2022, ISSN: 14321114. DOI: 10.1007/s00348-022-03441-6.

[22] J. Howell, T. C. Hammarton, Y. Altmann, and M. Jimenez, "High-speed particle detection and tracking in microfluidic devices using event-based sensing", *Lab on a Chip*, vol. 20, pp. 3024–3035, 16 Aug. 2020, ISSN: 1473-0189. DOI: 10.1039/D0LC00556H.

[23] T. Serrano-Gotarredona and B. Linares-Barranco, "A 128×, 1.5% contrast sensitivity 0.9% fpn 3 μs latency 4 mw asynchronous frame-free dynamic vision sensor using transimpedance preamplifiers", *IEEE Journal of Solid-State Circuits*, vol. 48, pp. 827–838, 3 2013, ISSN: 00189200. DOI: 10.1109/JSSC.2012.2230553.

[24] P. Lichtsteiner, C. Posch, and T. Delbruck, "A 128×128, 120 dB 15 μs latency asynchronous temporal contrast vision sensor", *IEEE Journal of Solid-State Circuits*, vol. 43, no. 2, pp. 566–576, Feb. 2008, ISSN: 00189200. DOI: 10.1109/JSSC.2007.914337.

[25] T. Serrano-Gotarredona and B. Linares-Barranco, *Low-power transimpedance gain circuit for temporal differentiation photodetection systems in dynamic vision sensors*, Spanish patent ES201130862P (in Spanish), Oficina Española de Patentes y Marcas, May, 2011.

Event-Driven Based CMOS Interface for Magnetic Sensing

Arman Shahryari[1], Fernando Pardo[2], José A. Boluda[2], *Càndid Reig
[1]Department of Electronic Engineering | [2]Department of Computer Science
ETSE, Universitat de València, Burjassot, Spain
e-mail: arman.shahryari@uv.es, fernando.pardo@uv.es, jose.a.boluda@uv.es, *candid.reig@uv.es

***Abstract*—An Event-Driven (ED) approach to magnetic sensing is proposed in this paper, utilizing a Selective Change-Driven (SCD) topology and Giant Magnetoresistance (GMR) sensors. The authors developed a 1×8 linear magnetic sensor vector designed for applications such as particle tracking. The system is implemented in standard Complementary Metal-Oxide Semiconductor (CMOS) mixed-signal TSMC 180 nm technology. We are presenting here a preliminary characterization by means of standard Cadence/Virtuoso simulations, including synthetic results from flowing-particle modeling. Unlike conventional frame-based systems, this SCD-based architecture expands the state of the art by performing hardware-level data filtering, drastically reducing data redundancy and power consumption. This makes the system particularly suitable for real-time applications such as high-speed particle sorting or low-latency biomagnetic monitoring, where efficient data throughput is critical.**

Keywords*—*Event-Driven (ED); Resistive Sensors; Giant Magnetoresistance (GMR); Selective-Change-Driven (SCD).

I. Introduction

In general terms, the neuromorphic approach can be understood as the reformulation of classical computing systems into architectures and topologies that attempt to mimic the behavior of the human brain [1]. It involves mimicking biological neurons with artificial equivalents. Unlike classic sensors that require post-sensing processing, bio-inspired systems respond directly to events, integrating perception and cognition within their topology. The aim of neuromorphic-inspired sensors is to create systems capable of generating a final response to an event by implementing the combined functions of perception and cognition in their topology. In this sense, Event-Driven (ED) sensors, also called Address Event Representation (AER) sensors, show clear advantages when compared with conventional sensors, in those scenarios where high speed or limited bandwidth is a must. This is of particular interest for vision sensors. In these architectures, the basic nodes (or pixels) consist of a photoreceptor (commonly a photodiode) together with the electronics (comparators, amplifiers and addressing management) required for adequately identifying and 'addressing' the proper triggered pixels. A particular strategy within AER vision sensors is the Selective Change Driven (SCD) approach [2]. In SCD systems, events are collected at the time they are produced, orderly chosen according to the magnitude of their change. For implementing such a strategy in silicon, some memory elements must be included in each pixel (commonly capacitors), as well as a specific selection circuit (such as Winner-Take-All, WTA, or similar). The use of SCD schemes have traditionally focused on movement detection and analysis [3], but the concept can be extended to many vision applications.

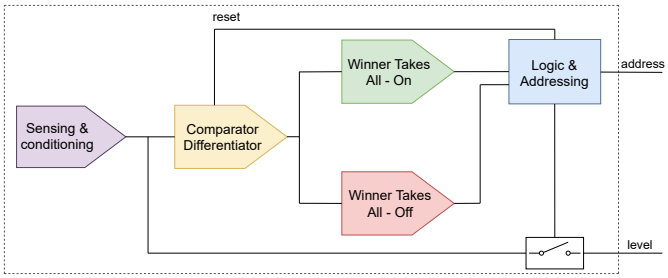

Figure 1. GMR Node scheme.

The Event-Driven concept is not limited to vision sensors [4], in fact, successful AER approaches have been reported for artificial cochleae [5] and magnetostrictive tactile sensors [6]. In both cases, a unique sensor (a microphone and a mechanical sensor) is considered. In addition, bio-inspiration could also be applied to sensing arrays not having counterparts within the human sensory systems, such as Ion-Sensitive Field Effect Transistors (ISFET) sensors [7], piezoresistive sensors [8], or Giant Magnetoresistance (GMR) sensors [9]. For implementing these proposals, integrable sensing elements should be used, replacing the function of the photodiodes.

We propose to apply a neuromorphic approach to magnetic sensing. As a test bench, we have developed a 1×8 linear magnetic sensor having an SCD topology together with GMR sensors, implemented in standard CMOS mixed-signal TSMC 180 nm technology. While the current version utilizes external GMR connections for initial characterization, the architecture is designed for future monolithic integration where sensors will be deposited directly onto the chip. The rest of the paper is organized as follows: Section II describes the circuit topology and its specific functional blocks; Section III presents the validation results with both electrical pulses and magnetic particle modeling; and Section IV concludes the work and discusses future research directions.

II. Circuit Topology

The general scheme of a SCD node [3] is depicted in Figure 1. The current sensor signal level is continuously compared against a sampled and hold value from the last time that sensor in the array was read-out. The difference between the last read-out and current values are rectified and amplified by means of a circuit based on a couple of Operational Transconductance Amplifiers (OTA). The differences I_{diff} of all nodes in the array are compared among them to obtain a set of winners with the

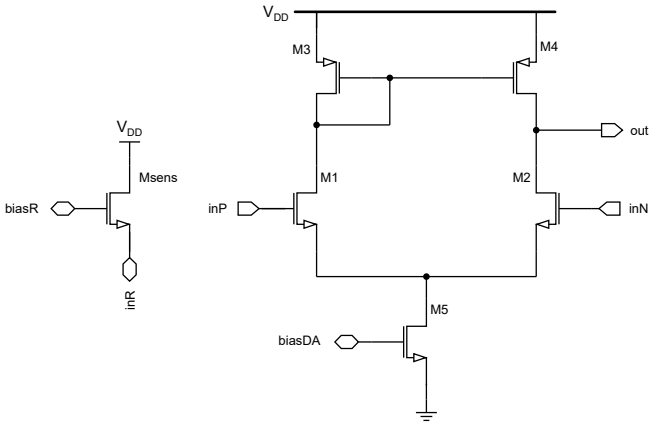

Figure 2. Analog input interface.

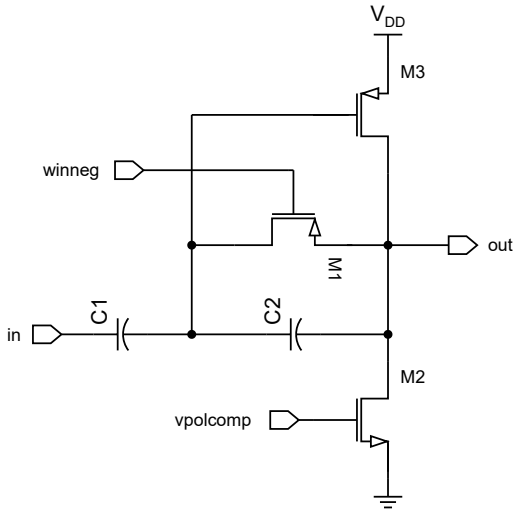

Figure 3. Comparator.

larger differences thanks to an analog Winner-Take-All (WTA) circuit. The distributed logic digital circuits take just one single winner from the set of winners. All this process takes place at each read-out clock cycle, ensuring that each access to the chip yields the output of the sensor that have undergone the largest change, since the last time that specific sensor of the array was read out. A detailed description can be found in [3].

A. Sensing and Conditioning

A significant contribution of this work is the sensing and conditioning block. Here, these pixels, commonly based on photodiodes are substituted by magnetic ones, based on GMR sensing elements.

The analog front-end is shown in Figure 2. It is based on a conventional current source and a differential amplifier with adjustable transconductance through the `biasDA` terminal. In this configuration, the architecture implements a reference by performing a global averaging of the sum of all sensors. This generates a dynamic baseline that is compared against the signal of the selected GMR element. This strategy enables the device to amplify local magnetic anomalies relative to the vector's mean, effectively canceling background magnetic fields.

B. Comparator / Differentiator

The identification of a winning resistive sensor within the array is determined by the transition of the `out` node in the capacitive-feedback comparator. In the architecture seen in Figure 3, a winner is defined as a sensor that experiences a magnetic field change significant enough to overcome a predefined threshold. Unlike traditional static comparators, this topology treats the `in` node as a dynamic input, where the capacitors C_1 and C_2 serve to decouple the DC magnetic baseline and focus exclusively on the voltage swing representative of GMR resistance fluctuations.

The operation is divided into a calibration (reset) phase and a sensing (competition) phase. During reset, the `winneg` signal activates the feedback transistor M_1, biasing the inverter (formed by M_3 and M_2) at its high-gain trip point. This process stores the quiescent environmental magnetic state across the capacitors. When `winneg` is released, the comparator becomes highly sensitive to any local deviation (V_{in}) from this stored baseline. The sensitivity of the "winner" detection is controlled by `vpolcomp`, which regulates the bias current of the inverter stage, determining the speed and the minimum ΔV required to flip the `out` signal.

A sensor is identified as a potential winner when its out node transitions, signaling that the local magnetic transient has exceeded the threshold. Unlike conventional WTA architectures that employ a master-slave bias scheme to force the selection of at least one winner, this topology leverages the high open-loop gain of the M_3/M_2 stage to amplify small-scale anomalies relative to the global average. By adjusting the `vpolcomp` bias, the system can modify the effective gap required to trigger an event, allowing the sensor to distinguish between localized magnetic field of interest and broad environmental noise.

C. Winner-Take-All ON / Winner-Take-All OFF

The Winner-Take-All (WTA) circuit plays a key role in event-driven applications where a single element must be selected according to its relevance [10]. The signal is processed by two logic blocks: WTA_{on} and WTA_{off} circuits, shown in Figure 4, respectively. These blocks are responsible for the decision-making core of the device. They compare the transient signal against a dynamic global reference, ensuring that only the most significant positive or negative fluctuations result in an event trigger. The decision-making stage identifies significant transients in the magnetic signal by employing two complementary blocks. The WTA_{on} Figure 4 (a) block is responsible for detecting magnetic signal increases. It utilizes an N-channel Metal-Oxide-Semiconductor (NMOS)-core high-gain stage where the input voltage is converted into current. When a local signal experiences a positive excursion that exceeds the global baseline by a predefined threshold, the high open-loop gain of the stage drives the corresponding win node high, signaling a positive magnetic event. Conversely, the WTA_{off} block in Figure 4 (b) is designed to monitor

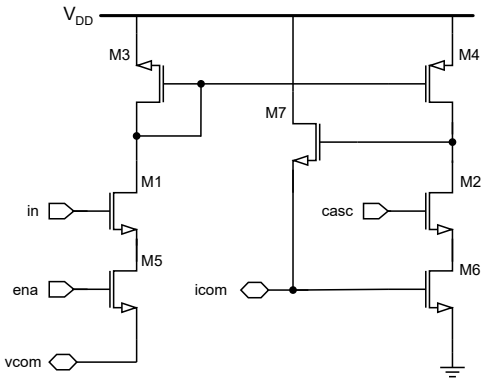

(a) WTA_{on} architecture.

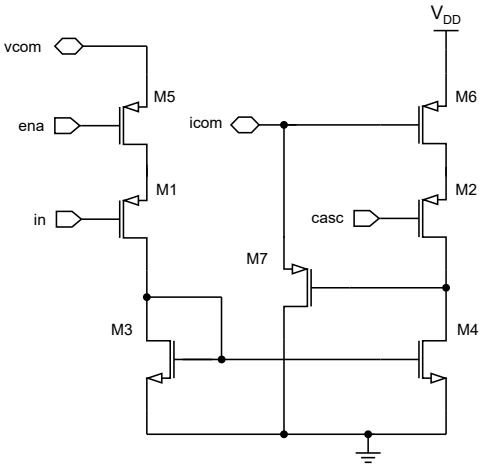

(b) WTA_{off} architecture.

Figure 4. Combined view of the decision-making digital core: (a) ON-event and (b) OFF-event detection.

signal decreases using a P-channel Complementary-Metal-Oxide (PMOS)-core topology. By tracking the lowest signal values relative to the established baseline, the circuit triggers an output event for the specific sensor where the voltage drop is most pronounced. In both blocks, the sensitivity to these subtle anomalies is regulated by the bias current, allowing the system to distinguish localized magnetic signatures from broad environmental noise. This dual-path architecture provides separate channels for ON and OFF events, acting like a filter that ignores the constant background and only reacts when a sensor sees something different from its neighbors. By performing this comparison in the analog domain through current competition, the system avoids the power overhead of high-speed digital sampling, maintaining the energy efficiency required for low-power, high-speed applications.

D. Logic / Addressing

Output management is handled asynchronously, as shown in Figure 5, by asserting column requests (`colRQ`). The single-winner selection circuit grants access via the `colGR` signal, which simultaneously serves as a reset mechanism for the winning channel to initiate a new competition cycle. Once

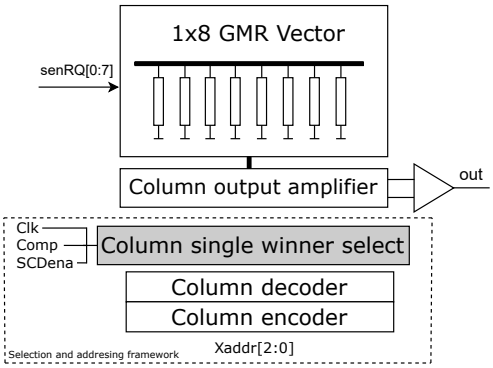

Figure 5. Sensor block with the digital single-winner selection.

arbitration is resolved, an Address Encoder translates the physical sensor position into a 3-bit digital word (`Xaddr[2:0]`). This process is synchronized by the `Clk` and `Comp` signals to prevent digital switching noise from coupling into the sensitive analog front-end. Finally, the infrastructure provides operational versatility through the `SCDena` signal, enabling a standard readout mode where a 3-to-8 decoder allows for individual sensor calibration against the global average.

III. Validation

The validation of the proposed architecture is executed through a two-stage simulation process to verify the overall logic consistency and the system's response to realistic magnetic stimuli. Initially, the sensing and conditioning blocks are subjected to idealized stimuli, just to characterize the fundamental behavior of the winner selection mechanism. Then, the system is integrated with a behavioral model of a magnetic particle environment, using the Magpylib library to simulate the trajectory of magnetized particles over the 1×8 sensor vector. The developed device has been tested by means of Cadence/Virtuoso/Spectre simulations, the golden standard in microelectronics design.

A. Excitation by Pulses

The first stage of validation focuses on the winner identification logic through a series of controlled transient injections. In this phase, the front-end is subjected to a series of calibrated square pulses applied sequentially to each sensing node. This approach is not intended to emulate the physical behavior of a magnetic particle, which produces a significantly different signal profile in reality. Instead, these square pulses serve as a deterministic electrical stimulus to verify the logic mapping of the competitive core. By triggering the sensors in a discrete, sequential order, the simulation confirms that the WTA_{on} and WTA_{off} architectures can correctly identify the winning channel within the 1×8 vector. Results are collected in Figure 6. These results validate the timing and response of the core, ensuring that no event collisions occur during the sequential identification of the winning channels.

B. Particle Tracking

Then, having in mind the subsequent application of magnetic particle tracking, a specific simulation experiment was designed.

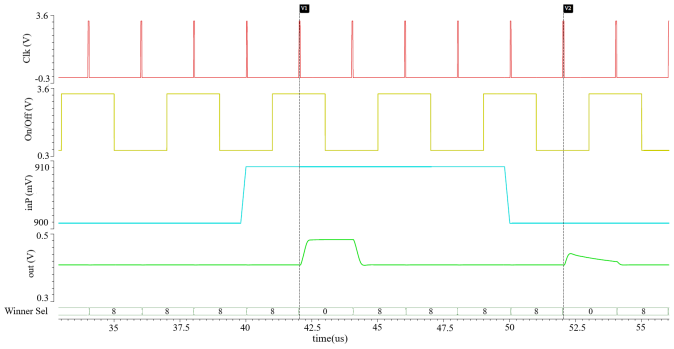

Figure 6. Excitation by pulses: System Clock ; WTA_{on} / WTA_{off}; Input square stimuli ($V_{peak} = 10\,\text{mV}$); Output response; Winner selection logic.

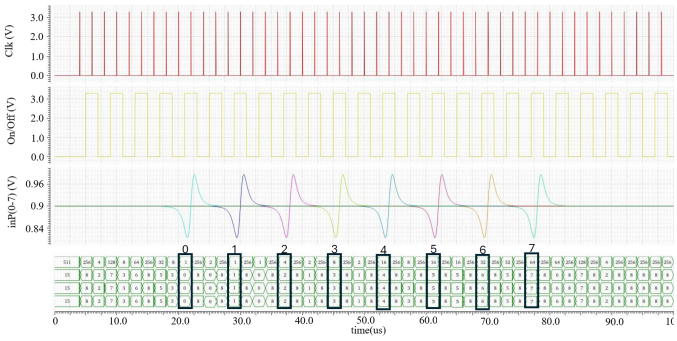

Figure 7. Response to a flowing particle through the 8 sensing elements.

Synthetic responses of magnetic microparticles flowing through a microfluidic channel were obtained using MagPyLib modeling. These data were used as excitation signals for the circuit. The results are collected in Figure 7. As observed, the system tracks the flow of the particles, identifying them individually.

IV. Conclusion and Future Work

A neuromorphic interface for resistive sensors has been developed and validated. Cadence/Virtuoso/Spectre demonstrated both the proper function of the system and its capability of tracking and identifying individual magnetic microparticles. Future research directions will focus on the transition from simulation to physical prototyping. A primary objective is the execution of a tape-out in 180 nm Complementary Metal-Oxide-Semiconductor (CMOS) technology to characterize the impact of thermal noise and substrate coupling on the sensitivity of the analog core under real operating conditions. Furthermore, we intend to quantify the system's common-mode rejection capabilities; while GMR elements are naturally sensitive to ambient fields, the architecture uses the global average of the sensor vector as a dynamic reference; this allows the system to cancel out widespread environmental noise while detecting only the localized magnetic changes caused by a passing particle. Looking ahead, the architecture is intended to be scaled into two-dimensional ($N \times M$) arrays, which will necessitate the exploration of hierarchical Winner-Take-All (WTA) structures to manage higher event densities without compromising power efficiency. Finally, the integrated system will be validated within a microfluidic setup to assess its performance in high-throughput particle sorting and biomagnetic monitoring applications.

Acknowledgments

This work has been supported by the Ministry of Digital Transformation and Civil Service under the Recovery, Transformation and Resilience Plan, funded by the European Union – NextGenerationEU, through the PERTE Chip Chairs program (Project Ref: TSI-069100-2023-0012) and by the by the Ministry of Science and Innovation (MCIN) and the State Research Agency (AEI) under the Recovery, Transformation and Resilience Plan, funded by the European Union – NextGenerationEU (Project Ref: PID2023-149071NB-C53).

References

[1] A. Vanarse, A. Osseiran, and A. Rassau, "Neuromorphic engineering — A paradigm shift for future IM technologies", *IEEE Instrumentation & Measurement Magazine*, vol. 22, pp. 4–9, 2 Apr. 2019, ISSN: 1094-6969. DOI: 10.1109/MIM.2019.8674627.

[2] F. Pardo, P. Zuccarello, J. A. Boluda, and F. Vegara, "Advantages of Selective Change-Driven Vision for Resource-Limited Systems", *IEEE Transactions on Circuits and Systems for Video Technology*, vol. 21, no. 10, pp. 1415–1423, Oct. 2011, ISSN: 1051-8215. DOI: 10.1109/TCSVT.2011.2162761.

[3] J. Boluda, F. Pardo, and F. Vegara, "A Selective Change Driven System for High-Speed Motion Analysis", *Sensors*, vol. 16, no. 11, p. 1875, Nov. 2016, ISSN: 1424-8220. DOI: 10.3390/s16111875.

[4] M.-H. Tayarani-Najaran and M. Schmuker, "Event-Based Sensing and Signal Processing in the Visual, Auditory, and Olfactory Domain: A Review", English, *Frontiers in Neural Circuits*, vol. 15, May 2021, ISSN: 1662-5110. DOI: 10.3389/fncir.2021.610446. (visited on 02/11/2026).

[5] S. C. Liu, A. Van Schaik, B. A. Minch, and T. Delbruck, "Event-based 64-channel binaural silicon cochlea with Q enhancement mechanisms", in *ISCAS 2010 - 2010 IEEE International Symposium on Circuits and Systems: Nano-Bio Circuit Fabrics and Systems*, 2010, pp. 2027–2030, ISBN: 9781424453085. DOI: 10.1109/ISCAS.2010.5537164.

[6] W. Zheng *et al.*, "Bio-inspired Magnetostrictive Tactile Sensor for Surface Material Recognition", *IEEE Transactions on Magnetics*, vol. 55, no. 7, Jul. 2019, ISSN: 00189464. DOI: 10.1109/TMAG.2019.2898546.

[7] M. Huang, J. B. Delacruz, J. C. Ruelas, S. S. Rathore, and M. Lindau, "Surface-modified CMOS IC electrochemical sensor array targeting single chromaffin cells for highly parallel amperometry measurements", *Pflügers Archiv - European Journal of Physiology*, vol. 470, no. 1, pp. 113–123, Jan. 2018, ISSN: 0031-6768. DOI: 10.1007/s00424-017-2067-y.

[8] R. S. Dahiya, G. Metta, M. Valle, and G. Sandini, "Tactile Sensing-From Humans to Humanoids", *IEEE Transactions on Robotics*, vol. 26, no. 1, pp. 1–20, Feb. 2010, ISSN: 15523098. DOI: 10.1109/TRO.2009.2033627.

[9] M. D. Cubells-Beltrán *et al.*, "Monolithic integration of Giant Magnetoresistance (GMR) devices onto standard processed CMOS dies", *Microelectronics Journal*, vol. 45, no. 6, pp. 702–707, Jun. 2014, ISSN: 00262692. DOI: 10.1016/j.mejo.2014.03.015.

[10] F. Pardo, C. Reig, J. A. Boluda, and F. Vegara, "A 4k-Input High-Speed Winner-Take-All (WTA) Circuit with Single-Winner Selection for Change-Driven Vision Sensors", *Sensors*, vol. 19, no. 2, 2019, ISSN: 1424-8220. DOI: 10.3390/s19020437.

Denoising Electromagnetic Sensor Spectra for Maize Crop Evaluation: A Comparative Study of Advanced Architectures

Paulo E. Cruvinel[1,2]
[1]Embrapa Instrumentation, São Carlos, SP, Brazil
[2]Post-Graduation Program in Computer Science - Federal University of São Carlos, SP, Brazil
Email: paulo.cruvinel@embrapa.br

Abstract— **Precision agriculture relies on high-fidelity data for optimal crop management. However, multispectral sensors mounted on Unmanned Aircraft Systems (UAS) are susceptible to significant electromagnetic noise—including thermal, sensor-specific, and motion-induced sources—which degrades data quality and classification accuracy. This paper addresses the critical issue of denoising electromagnetic sensor spectra, particularly across the visible RED, and Near-InfraRed (NIR) bands. We present a comparative analysis of four denoising techniques: a 1D Convolutional Neural Network (1D-CNN), a Denoising Convolutional Network (DnCNN), a Convolutional Autoencoder (CAE) implemented in TensorFlow, and a proposed hybrid architecture combining a low-pass analog operational amplifier filter with a CNN-Long Short-Term Memory (CNN-LSTM) network. Performance is evaluated using Mean Relative Error (MRE), Peak Signal-to-Noise Ratio (PSNR), and the Structural Similarity Index Measure (SSIM). Numerical results indicate that while pure deep learning models excel at handling random noise, the proposed hybrid approach provides superior preservation of critical spectral features in the NIR region—crucial for crop stress analysis—while enhancing efficiency by reducing the computational load on the network.**

***Keywords-electromagnetic light-band sensors*; *signal filtering*; *convolutional neural network*; *operational amplifier*; *agricultural sensor*; *intelligent instrumentation*.**

I. INTRODUCTION

Noise in electromagnetic (EM) sensor spectra represents unwanted energy—both internal and external—that obscures the desired measurement signal [1]. It is characterized by Power Spectral Density (PSD) across various frequencies and sets the fundamental limits of sensor sensitivity (often defined as the Noise Equivalent Intensity or Noise Floor). Noise in EM systems is categorized by its origin and spectral characteristics, including thermal noise (Johnson-Nyquist Noise) caused by the random thermal motion of electrons in resistive components, recognized as White Noise (constant amplitude across frequency); flicker noise, which is dominant at low frequencies; shot noise, which arises from the discrete nature of electrons crossing potential barriers (e.g., in junctions); environmental noise (EMI), which occurs due power lines, motors or even from natural signals, like lightning for instance, that couple into the sensor via radiation or conduction; Random Telegraph Noise (RTN), which is related to high-frequency switching between two resistance states due to defects in the sensor's free layer, i.e., common in magnetic sensors. In fact, the noise spectrum of a sensor often shows a high-frequency white noise plateau and a rising noise floor at low frequencies due to noise [2].

Table I shows a summary of noise sources related to electromagnetic sensors.

TABLE I. TYPICAL NOISE SOURCES

Type	*Description*	*Frequency Dependency*
Thermal	Brownian motion of electrons	White (Flat)
Flicker (1/f)	Trap-and-release of charges	Proporcional to 1/f
Shot	Quantized nature of charge	White (at high bias)
Environmental	External EMI (50/60Hz, harmonics, among others)	Varies (Spikes)
Microphonics	Mechanical vibrations	Low frequency

Typical techniques to mitigate noise from the ElectroMagnetic (EM) spectrum, which is closely known as ElectroMagnetic Interference (EMI) reduction or ElectroMagnetic Compatibility (EMC) management, focus on grounding, shielding, filtering, and physical layout optimization. These methods aim to reduce the emission of noise at the source and increase the immunity of devices to external interference, i.e., improving the Signal to Noise Ratio (SNR). In such a context, signal filtering plays an important role, since it is a fundamental process in electrical engineering and signal processing, designed to separate, remove, or enhance specific components of a signal (such as noise, interference, or irrelevant frequencies).

Traditional filtering methods, whether analog or digital, are generally linear and require extensive prior knowledge of noise characteristics, making effective signal separation difficult when signal and noise overlap in the frequency domain [3]. This limitation has motivated the adoption of Convolutional Neural Networks (CNNs) as adaptive, non-linear, data-driven filters that can be optimized based on the specific characteristics of the signal [4]. However, the dynamic nature of real-world environments necessitates retraining these models to maintain error margins within acceptable limits. Data samples used for training can lose their validity over time—a phenomenon known as data decay or obsolescence—which leads to performance degradation as current data deviates from the training distribution, causing concept drift.

Conversely, in complex signal or image processing, a single traditional filter often falls short. CNNs, leveraging multiple hidden layers, automatically extract hierarchical,

complex patterns—ranging from low-level features (e.g., edges, peaks) to high-level semantic representations [5]. A CNN applies learned kernels to an input (e.g., a 1D signal or image) to produce a feature map. While this process is analogous to Finite Impulse Response (FIR) filtering, the key advantage is that the weights (kernels) are learned directly from the data through backpropagation rather than being handcrafted.

Therefore, selecting the optimal filter for Signal-to-Noise Ratio (SNR) improvement requires a strict evaluation of advantages and disadvantages, balancing the need for aggressive noise mitigation with the preservation of critical signal features.

In this context, hybrid filter architectures—combining the adaptability of CNNs with the reliability of traditional techniques—represent an emerging paradigm for customized, sensor-driven signal processing that warrants further investigation.

The utilization of multispectral sensors for monitoring maize crops has revolutionized precision agriculture [6], enabling the assessment of chlorophyll content, hydration status, and plant stress through the identification of specific reflectance patterns in the Near-InfraRed (NIR) and red-edge spectral bands. Despite their advantages, images collected by UAS-mounted sensors frequently suffer from electrical and magnetic interference [7].

Electromagnetic noise can arise from atmospheric conditions, sensor electronics, and UAS-motor interferences, often presenting as Gaussian noise or complex artifacts. These noises contaminate the spectral data, leading to incorrect vegetation indexes.

To address the limitations of traditional EMI suppression methods, this paper proposes a hybrid approach combining analog filtering with a CNN. The core novelty lies in a two-stage approach: a low-power analog front-end that provides robust, immediate mitigation of broad-band noise, followed by a post-processing CNN that adapts to the specific, complex features of each light-bands signals.

This combination provides both high-frequency attenuation and intelligent, non-stationary noise handling, surpassing the performance limitations of standard filtering techniques. In fact, traditional noise reduction methods (Gaussian filtering) frequently struggle to differentiate between sensor noise and relevant agricultural spectral signatures. This study evaluates not only Deep Learning-based approaches but also hybrid architecture for processing multispectral data from maize crops.

Furthermore, comparative analyses are conducted using the Mean Squared Error (MSE), Peak Signal-to-Noise Ratio (PSNR), and the Structural Similarity Index (SSIM) metrics, which preserve crucial spatial-spectral information for accurate agricultural diagnostics.

Following this introduction, the remainder of this paper is organized as follows. Section II outlines the materials and methods, including agricultural datasets, feature descriptors, and evaluated noise-filtering architectures. Section III provides a comparative analysis of results based on PSNR, SSIM, and MRE metrics. Finally, Section IV presents the conclusions.

II. MATERIALS AND METHODS

A MicaSense RedEdge-M multispectral camera has been considered and embedded onboard, i.e., using a multirotor UAS, DJI Matrice 100 (Figure 1). The specifications of the multispectral sensors from the Micasense camera are detailed in Table II [8].

To capture the various phenomenological states of the maize, eight distinct imaging flights were carried out [9]. In addition, for the light bands data acquisition protocol, the use of the Ground Control Points (GCP), a high-precision GPS in conjunction with a Real-Time Kinematic (RTK) receiver (i.e., allowing accuracy of ± 1 cm, and a Downwelling Light Sensor (DLS) to allow images' contrast correction due to possible superimposition of clouds in the sky has been considered.

TABLE II. SPECIFICATIONS FOR THE MICASENSE CAMERA

Parameters	Specifications
Weigth	170 g (Including DLS)
Dimensions	9.4 cm × 6.3 cm × 4.6 cm (3.7" × 2.5" × 1.8")
External Power	4.2V–15.8V, 4W nominal, 8W peak
Spectral Bands	Narrowband: Blue, Green, Red, Near-IR
Capture Rate	1 capture per second (per band), 12–bit RAW
Ground Sample Distance (GSD)	5.95 cm/pixel (per band)
Wavelength	Blue (475 nm center ± 20 nm) Green (560 nm ± 20 nm) Red (668 nm center ± 10 nm) Near-IR (840 nm ± 40 nm)

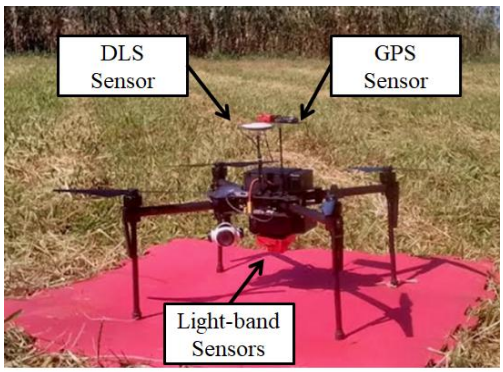

Figure 1. The UAS and hardware setup with sensors for the electromagnetic bands for signals acquisition.

Furthermore, in accordance with the UAS settings and the onboard light-band sensors, for all the flights, the morning periods have been considered to be a time from 11 A.M. to 12 A.M.

To validate the denoising method, for the electromagnetic sensors, when operating in maize crops, an experimental trial was conducted following the cultural management standards of Embrapa Instrumentation. The agricultural experiment took place at the National Reference Laboratory for Precision Agriculture (LANAPRE), in São Carlos, SP, Brazil, near coordinates 21°57'3.9" S and 47°51'10.9" W. The experimental area of 4,000 m² cultivated with maize (Zea mays L.) was managed under precision agriculture

principles. As illustrated in Figure 2, the Pioneer P4285 VYHR flat-grain hybrid was used, sown at a density of 5 seeds per linear meter and a spacing of 0.90 m between rows. The layout consisted of forty blocks of 12 rows each (60 rows total), resulting in 600 plants per block and a total population of 24,000 seeds.

Figure 2. Partial view of the maize experimental field during flight 8, taken prior to the critical reproductive stages (silking, blister, dough, dent, and physiological maturity).

The block diagram in Figure 3 illustrates the sensor-based denoising architectures analyzed in this study. Based on data from the multispectral camera, we use both original and filtered signals to evaluate, as an example, the Normalized Difference Vegetation Index (NDVI). The NDVI [10-11] utilizes linear combinations of the RED (668 nm ± 10 nm) and Near Infra-Red (NIR) (840 nm ± 40 nm) bands to monitor biomass density. For agricultural applications, this index is generally analyzed within the 0.0 to 1.0 range.

Besides, prior to calculating the NDVI indices, the analog and digital signals (post A/D conversion) were filtered using several approaches: 1D Convolutional Neural Network (1D-CNN) [12], Denoising Convolutional Neural Network (DnCNN) [13-15], and a Convolutional Autoencoder (CAE) implemented in TensorFlow, CAE (TensorFlow) [16-17]. The performance of these models was compared against a hybrid architecture integrating a active low-pass Butterworth Op-Amp filter [18-19] with a Convolutional Neural Network-Long Short-Term Memory (CNN-LSTM) [20].

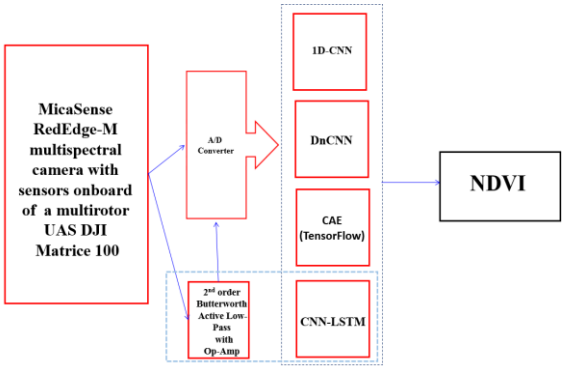

Figure 3. The sensor-based arrangement for the comparative study for denoising the EMI based on advanced architectures.

Regarding the filter`s architecture, the 1D-CNN for Electromagnetic Interference (EMI) noise reduction, it is a deep learning approach that directly analyzes, cleans, and removes unwanted noise from one-dimensional time-series or frequency-domain data. Unlike traditional filtering methods that rely on fixed mathematical transformations, 1D CNNs automatically learn to distinguish between desired signals and noise patterns directly from raw data, resulting in accurate and robust denoising—particularly for complex and non-stationary noise. This specialized network uses convolutional kernels (filters) that slide along a single dimension to extract features. It consists of input layers (for receiving noisy raw data), multiple convolutional layers (for feature extraction), and pooling layers (for down sampling to reduce dimensionality), often structured as an autoencoder that transforms noisy inputs into improved, reconstructed outputs. The network is trained on pairs of noisy and clean signals; through backpropagation, it learns to maximize the SNR and minimize the Mean Squared Error (MSE) between the input and output. In this work, it was implemented as a Convolutional Autoencoder, where the encoder compresses the noisy waveform into a latent representation of key features, and the decoder reconstructs the signal with improvements.

The DnCNN architecture, short for denoising convolutional neural network, is a deep learning-based model designed to remove noise from images (and signals in general) while preserving structural details. Also, unlike traditional denoising methods that often blur images, DnCNN leverages residual learning to specifically learn the noise in an image and subtract it, resulting in sharper and higher-quality outputs.

The core components of DnCNN are centered on residual learning, where the network is trained to learn the residual noise, i.e., the difference between the noisy and an improved image, instead of the direct mapping from noisy to improve the SNR. This approach can allow the training process more efficient and accurate. For this work, we used an architecture that also incorporates batch normalization layers between convolutional layers and rectified linear units, a technique that speeds up training and accelerates convergence. We also used a deep architecture composed of 20 layers of 3x3 convolutions, and pooling layers were intentionally avoided to retain essential structural information.

In addition, a Convolutional Autoencoder (CAE) was implemented in TensorFlow. It serves as a powerful deep learning approach for EMI noise reduction, utilizing unsupervised neural networks to identify, isolate, and remove unwanted electromagnetic noise from captured electronic signals. In this work, the CAE is employed to process digitally converted, noisy EMI signals captured from camera sensors, mapping these corrupted inputs back to a clean, reconstructed state. The architecture consists of an encoder, which uses convolutional layers to compress input signals into a lower-dimensional latent representation, filtering out random noise while retaining essential features,

 ISBN: 978-1-68558-388-0

and a decoder, which reconstructs the denoised signal from this compact representation. Leveraging the TensorFlow framework, the CAE is trained on pairs of noisy and clean data to learn the underlying, noise-free structure of the signal. By focusing on the core signal structure of specific electromagnetic bands, the network learns to ignore high-frequency, chaotic EMI noise. This trained model efficiently removes random noise while preserving crucial signal components. Moreover, a hybrid approach combining a low-pass active Op-Amp filter with a subsequent CNN-LSTM model was implemented for evaluation. This multi-stage strategy leverages hardware speed to eliminate high-frequency noise while using data-driven modeling to remove complex, non-stationary residual interference. The technique operates in two stages: first, an active low-pass analog filter acts as a pre-processing step to reduce broadband EMI, particularly differential-mode noise. Second, the CNN-LSTM model processes the partially filtered signal to remove nonlinear, non-Gaussian, and non-stationary noise that analog filters cannot eliminate. This CNN-based modality extracts spatial-structural features, effectively capturing local temporal-frequency characteristics.

Figure 4 illustrates the second-order Butterworth low-pass filter implemented in this work for each light band. This circuit features a non-inverting Op-Amp configuration with two RC networks to define the frequency response. The corresponding Bode plot demonstrates a characteristic -40 dB/decade roll-off in the stopband. Furthermore, the filter's response is contingent upon the voltage magnification factor (Q) at the cutoff frequency.

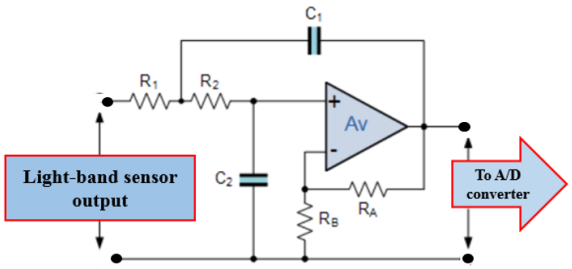

Figure 4. Hardware architecture of the second-order Butterworth low-pass filter used for light-band sensor signal filtering.

The cutoff frequency is given by (1) as follows.

$$f_c = \frac{1}{2\pi\sqrt{R_2 R_3 C_2 C_3}} \quad (1)$$

For the Butterworth response, it is common to set R_2=R_3 surface mount resistors and C_2=C_3 ceramic capacitor. For a cutoff frequency of 200 kHz with 100 pF capacitors, the resistor value should be equal to 8.2 kΩ. To maintain the Butterworth response (quality factor Q = 0.707) in a Sallen-Key topology of equal components, the Op-Amp gain was fixed at around 1.6 through the feedback resistors. For this work, we have selected the Analog Devices LTC 6269 Op-Amp, which has a 500 MHz Gain-Bandwidth Product (GBW), ultra-low bias current FET-input.

Furthermore, to improve SNR, all the collected signals were filtered, and each ROI was rotated, i.e., taking into consideration the angle calculation by (2) as follows.

$$Rotation = \begin{bmatrix} 1 & 0 & t_x \\ 0 & 1 & t_y \\ 0 & 0 & 1 \end{bmatrix} \begin{bmatrix} \cos\theta & -\sin\theta & 0 \\ \sin\theta & \cos\theta & 0 \\ 0 & 0 & 1 \end{bmatrix} \begin{bmatrix} 1 & 0 & -t_x \\ 0 & 1 & -t_y \\ 0 & 0 & 1 \end{bmatrix} \quad (2)$$

where the parameters ($-t_x$), and ($-t_y$) correspond to the translation of the ROI to the origin, whereas (t_x), and (t_y) can allow shifting it back to its original position.

Additionally, the evaluation of the different filtering processes was conducted using the MSE, PSNR, and the SSIM metrics [21].

The MSE gives a measure about the average of the squares of the errors, which are the differences between corresponding pixel intensities in the original and distorted images. It is given by (3) as follows.

$$MSE = \frac{1}{MN}\sum_{i=1}^{M}\sum_{j=1}^{N}(F(i,j) - I(i,j))^2 \quad (3)$$

The PSNR is the ratio of maximum signal intensity to distortion noise, expressed in decibels (dB). Higher values signify better quality, making it a vital metric for denoising applications requiring high pixel-level precision. It is calculated using (4), with MAX_v defined as the maximum potential pixel value for the given digital image format.

$$PSNR = 20\log_{10}\left(\frac{MAX_v}{\sqrt{MSE}}\right) \quad (4)$$

The SSIM is a perception-based image quality metric that evaluates the similarity between two images (typically an original image and a distorted or noisily image by measuring luminance, contrast, and structural degradation. It is calculated using (5) as follows.

$$SSIM(x,y) = \frac{(2\mu_x\mu_y + c_1)(2\sigma_{xy} + c_2)}{(\mu_x^2 + \mu_y^2 + c_1)(\sigma_x^2 + \sigma_y^2 + c_2)} \quad (5)$$

where μ_x is the pixel sample mean of x, μ_y is the pixel sample mean of y, $(\sigma_x)^2$ is the sample variance of x, $(\sigma_y)^2$ is the sample variance of y, σ_{xy} the sample covariance of x and y, c_1,and c_2 are variables to stabilize the division with weak denominator, i.e. to avoid division by zero. Using SSIM alongside PSNR is crucial because PSNR measures pixel-level technical error (noise removal strength), while SSIM evaluates perceptual structural similarity (edge/detail

preservation). PSNR often favors blurry images, whereas SSIM ensures denoised images remain visually clear to human perception, preventing over-smoothing.

III. RESULTS AND DISCUSSIONS

Radiometric calibration was performed previously to the multispectral signal and image acquisition, in fact it was necessary to collect both analog signals from the RED and NIR sensors, as well as to convert then in digital, as metadata, for the digital image to a physical scale.

Besides, the geometry of the aerial image was established by the size of the sensor, the focal length, and the height of the UAS flights, which together determine its Ground Sample Distance (GSD), as presented in Table III. The GSD provides the corresponding measure for the pixels of the surface of the experimental area or the area covered by the image. The percentages established for both the lateral and frontal overlapping of the aerial images were equal to 80% respectively.

The total number of registered images was equal to 320 for each spectral band, i.e., leading to a required storage capacity equal to 14.76 GB (gigabytes), because the surface width and height were equal to 25 m × 80 m, respectively, and the distances between each front and side capture were 4 m and 5 m, respectively.

TABLE III. PARAMETERS USED FOR DATA ACQUISITION

Description	Values	Units
Flying altitude	138	m
Mission flying time	12	min
Max. speed of flying	11	m/s
Front and side overlap	80	%
Ground sample distance	5.95	cm/pixel

Figure 5 shows example results from the eighth flight, featuring rotated images and their corresponding Regions Of Interest (ROI) for block 25 analysis. The images are displayed in RGB, NIR, and RED light-bands, which were used to calculate NDVI values.

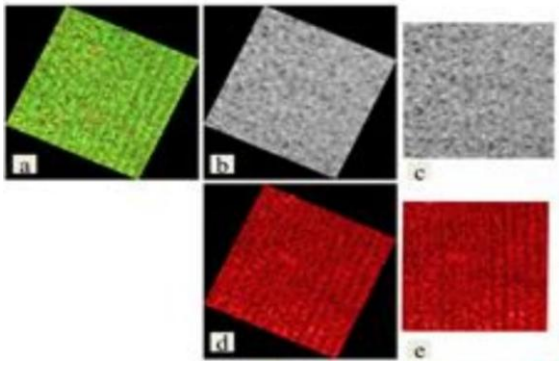

Figure 5. Analysis using the original electromagnetic light-bands (Block 25, Flight 8): (a) RGB, (b) NIR, (c) ROI NIR, (d) RED, and (e) ROI RED.

Table IV presents a numerical comparison of CNN-only architectures versus a hybrid approach that combines a low-pass active filter with a specific CNN algorithm. Utilizing RGB, NIR, and Red light-bands from UAS flight-eight, this analysis evaluates performance in maize crop monitoring using MSE, PSNR, and SSIM metrics.

TABLE IV. NUMERICAL COMPARISON OF CNN-ONLY ARCHITECTURES VERSUS A HYBRID APPROACH

Light-bands	*Metric*	*1D-CNN*	*DnCNN*	*CAE TensorFlow*	*Hybrid Butterworth+ CNN-LSTM*
RED	MRE (%)	5.2	3.5	3;8	1.2
	PSNR (dB)	28.5	32.1	31.5	38.4
	SSIM	0.88	0.92	0.91	0.97
NIR	MRE (%)	6.1	4.0	4.2	1.5
	PSNR (dB)	27.8	31.0	30.5	37.2
	SSIM	0.86	0.90	0.89	0.95

It was possible to observe that the use of the 1D CNN approach for EMI noise reduction is trained on pairs of noisy and less-noisy signals. Through backpropagation, it learns to maximize the SNR and minimize the Mean Squared Error (MSE) between the input and output. It presents high accuracy in removing complex, non-stationary noise. Besides, it does not require handcrafted features or complex pre-processing, operating directly on the raw input data. It is also highly efficient and well-suited for this application and resource-constrained devices. In this work, the 1D CNN was used to invert the EMI data to obtain good images, removing noise from raw data to directly estimate values from agricultural structures.

The use of a DnCNN enabled blind Gaussian denoising, meaning, it was able to remove noise of unknown or varying levels without needing to be retrained for different, specific noise intensities. Such a CNN presents high performance, as it consistently outperforms traditional methods like BM3D in both PSNR and SSIM indices.

By using a Convolutional Autoencoder (CAE) implemented in TensorFlow for noise reduction, it has shown that the model learns to ignore high-frequency, chaotic noise and focus on the core signal structure. In fact, the encoder reduces data dimensionality, essentially filtering out random noise while keeping essential signal components. In the process, the decoder reconstructs the signal without the noise. The observed key benefits include non-linear noise modeling and the processing of complex data, making it useful for application to EMI sources, including those that may occur in agricultural areas.

Furthermore, the proposed hybrid system—utilizing an active 2nd-order Butterworth Op-Amp filter combined with a CNN-LSTM model—outperforms standalone 1D-CNN, DnCNN, and CARE models in denoising and enhancing NDVI across Red and NIR bands. This hybrid architecture provides superior PSNR and SSIM, minimizing the MRE by handling high-frequency noise via hardware (Butterworth filter) and addressing structural/temporal inconsistencies via software (CNN-LSTM). Figure 6 illustrates the resulting

application of this hybrid architecture after the filtering process, using a sample from Block 25 of the eight-flight dataset.

For the CNN-LSTM algorithm it was considered convolutional layers to extract the spatial features across each RED, GREEN, BLUE, and NIR light-bands, followed by the LSTM layers to model temporal dynamics and suppress interference. As for all the evaluated CNN in this work, such a model was implemented in Python using an open-source high-level Application Programming Interface (API) to build the neural network (*Keras*), as well as a TensorFlow, where the signal patterns were identified, since LSTM layers learn long-term sequence correlations to refine the signal, using datasets structured as samples, time steps, or even features.

This arrangement has proved to allow a significant impact on the NDVI, as the hybrid model preserves the sharp contrast between RED absorption and NIR reflectance. Figure 7 shows the NDVI maps before the application of the light-bands hybrid filtering process, and after the application of the hybrid filter, i.e., carried out during flight 8, taken prior to the critical reproductive maize stages.

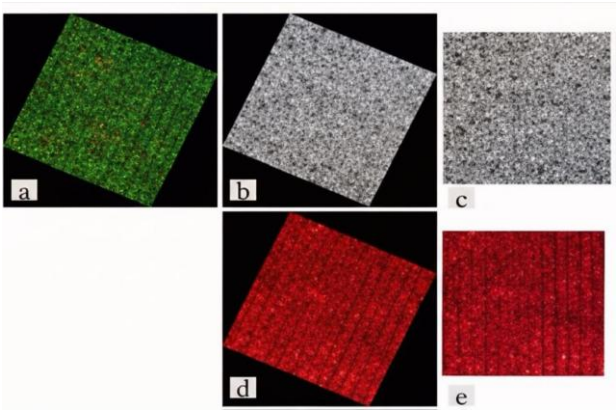

Figure 6. Hybrid architecture filtered samples (Block 25, Flight 8): (a) RGB, (b) NIR(c), ROI for NIR(d), RED(e), and ROI for RED.

Consequently, the resulting NDVI values are closer to ground truth (with less than 0.05 deviation), while standalone models tend to oversmooth, leading to an underestimation of vegetation health and biomass. Working with better-accuracy NDVI values is crucial for maize management because it enables precise, proactive decision-making that optimizes resource use, maximizes yield, and significantly reduces costs. In maize production, small inaccuracies in NDVI can lead to mismanagement of nitrogen fertilizer, incorrect, delayed, or premature irrigation, and an inability to detect early-stage crop stress or nutrient deficiencies before they become irreversible.

In such a context, high-accuracy NDVI allows for variable rate nitrogen application, ensuring fertilizer is applied based on actual plant demand, reducing environmental impact and cost. Also, accurate, time-series NDVI data improves yield predictions, particularly in the mid-to-late growth stages.

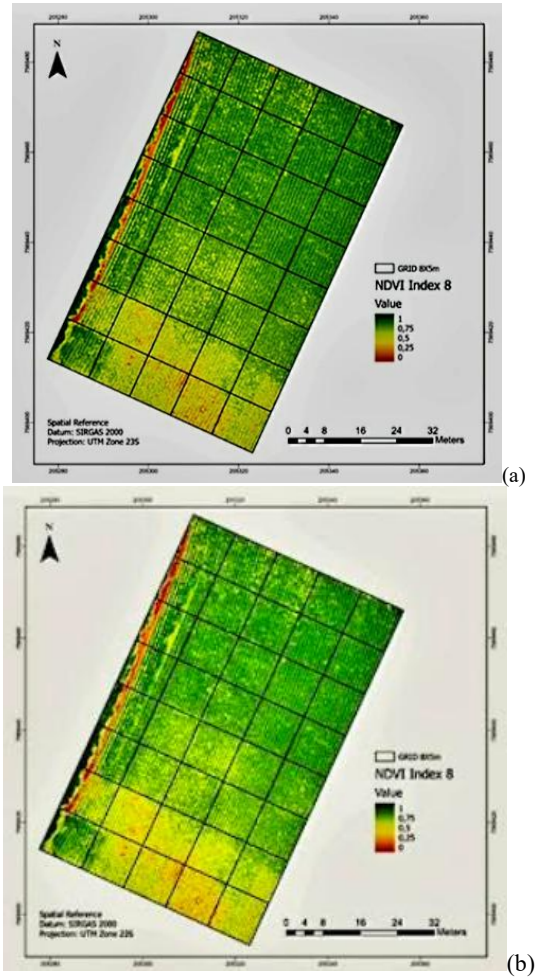

Figure 7. NDVI maps for the maize experimental field from flight 8, capturing data prior to the critical reproductive stages of the crop. Map (a) shows the results before filtering, while (b) shows the data after applying the hybrid filter for electromagnetic noise reduction.

Furthermore, lower NDVI values can indicate drought, disease, or pest damage. Accurate data acts as an early warning system, allowing farmers to identify stressed zones before they are visible to human being eye.

IV. CONCLUSION AND FUTURE WORK

This work compared 1D-CNN, DnCNN, CAE, and a hybrid CNN-LSTM for spectral denoising across electromagnetic light-bands used in agriculture. The Hybrid CNN-LSTM model provided the best performance, with an average PSNR of 37.8 dB and high SSIM, making it suitable for high-precision, op-amp-based electromagnetic sensor systems. Future research will focus on developing an embedded platform that integrates an active filter and a Convolutional Neural Network (CNN) for real-time

agricultural applications, thereby improving crop productivity and optimizing natural resource utilization.

ACKNOWLEDGMENT

This research was partially supported by both the São Paulo Research Foundation, Brazil (FAPESP, Process No. 17/19350-2), and the Brazilian Corporation for Agricultural Research (Embrapa).

REFERENCES

[1] M. Kaur, S. Kakar, and D. Mandal, "Electromagnetic interference," in *Proceedings of the 3rd International Conference on Electronics Computer Technology*, Kanyakumari, India, vol. 4, pp. 1-5, 2011.

[2] J T. Kelemenová, O. Benedik, and I. Koláriková, "Signal noise reduction and filtering," *Acta Mechatronica*, vol. 5, nº. 2, pp. 29-34, 2020.

[3] M. M. Seron and G. C. Goodwin, "Design limitations in linear filtering," in *Proceedings of the 34th IEEE Conference on Decision and Control*, New Orleans, LA, USA, 1995, vol. 2, pp. 1519-1524, 1995.

[4] P. Purwono et al., "Understanding of convolutional neural network (CNN): A review," *International Journal of Robotics and Control Systems*, vol. 2, nº. 4, pp. 739-748, 2023.

[5] X. Zhao et al., "A review of convolutional neural networks in computer vision," *Artificial Intelligence Review*, vol. 57, nº.4, pp. 1-43, 2024.

[6] S. Laveglia, G. Altieri, F. Genovese, A. Matera, and G. C. Di Renzo, "Advances in sustainable crop management: integrating precision agriculture," *AgriEngineering*, vol. 6, nº. 3, pp. 3084-3120, 2024.

[7] P. E. Cruvinel and L. A. Colnago, "Sensor-based platform for evaluation of atmospheric carbon sequestration's potential by maize crops," in *IARIA, Proceedings of the Tenth International Conference on Advances in Sensors, Actuators, Metering and Sensing (ALLSENSORS 2025)*, Nice, France, pp. 31-36, 2025.

[8] MicaSense RedEdge-M™, Multispectral Camera, *User Manual*, vol. 1, pp. 1-47, 2017.

[9] M. W. L. Carvalho et al., "Productive performance of maize crop irrigated with and without water deficit in different plant arrangements," *Brazilian Journal of Maize and Sorghum*, vol. 19, pp. 1196-11208, 2020.

[10] J. W. Rouse et al., "Monitoring vegetation systems in the great plains with ERTS," in Proceedings of the Third Earth Resources Technology Satellite-1 Symposium, National Aeronautics and Space Administration (NASA), SP-351, Washington DC, USA, pp. 309-317, 1974.

[11] C. J. Tucker, "Red and photographic infrared linear combinations for monitoring vegetation," *Remote Sensing of Environment*, vol. 8, pp. 127-150, 1979.

[12] S. Kiranyaz, O. Avci, O. Abdeljaber, T. Ince, M Gabbouj, and D. J. Inman, "1D convolutional neural networks and applications: A survey," *Mechanical Systems and Signal Processing*, vol. 151, pp. 107398-107418, 2021.

[13] S. Roy, Single image DnCNN visibility improvement (SImDnCNNVI)", *Scientific Visualization*, vol. 14, nº. 3, 2022.

[14] X. T. Dong, Y. Li, and B. J. Yang, "Desert low-frequency noise suppression by using adaptive DnCNNs based on the determination of high-order statistic," *Geophysical Journal International*, vol. 219, nº. 2, pp. 1281-1299, 2019.

[15] T. Rahim, S. Khan, M. A. Usman, and S. Y. Shin, "Exploiting de-noising convolutional neural networks DnCNNs for an efficient watermarking scheme: A case for information retrieval," *IETE Technical Review*, vol. 38, nº. 2, pp. 245-255, 2021.

[16] Y. Zhang et al., "CAE-CNN: Predicting transcription factor binding site with convolutional autoencoder and convolutional neural network," *Expert Systems with Applications*, vol. 183, pp. 115404-115414, 2021.

[17] L. Yu, B. Li, and B. Jiao, "Research and implementation of CNN based on TensorFlow," in *Proceedings of the IOP Conference Series: Materials Science and Engineering*, vol. 490, nº.4, pp. 042022-042027, 2019.

[18] T. Khanna and D. K. Upadhyay, "Design and analysis of higher order fractional step Butterworth filters," in *Proceedings of the International Conference on Soft Computing Techniques and Implementations (ICSCTI)*, Faridabad, India, pp. 77-82, 2015.

[19] F. S. Ibarra et al., "Design of 2nd order low-pass active filters by preserving the physical meaning of design variables," *Revista Mexicana de Física*, vol. 57, nº.1, pp. 1-10, 2011.

[20] A. Rostamian and J. G. O'Hara, "Event prediction within directional change framework using a CNN-LSTM model," *Neural Computing and Applications*, vol. 34, nº. 20, pp.17193-17205, 2022.

[21] D. Sadykova and A. P. James, "Quality assessment metrics for edge detection and edge-aware filtering: A tutorial review,"in Peoceedings of the International Conference on Advances in Computing, Communications and Informatics (ICACCI), pp. 2366-2369, 2017.

Operational Noise Characterization and Band-Integrated Detection Limits of a Thermo-Formed Piezoelectret Accelerometer

Igor Nazareno Soares*, Ruy Alberto Corrêa Altafim*, Ruy Alberto Pisani Altafim†
*Department of Electrical and Computer Engineering, Engineering School of São Carlos
University of São Paulo
São Carlos, Brazil
†Department of Computer Systems, Informatics Center
Federal University of Paraíba
João Pessoa, Brazil
e-mail: igor.soares@usp.br, altafim@usp.br, ruy@ci.ufpb.br

***Abstract*—Thermo-Formed Piezoelectret Accelerometers (TFPAs) have recently emerged as mechanically tunable vibration sensors. While previous studies have demonstrated their sensitivity and structural tunability, the stochastic limits of vibration detection have not yet been experimentally quantified. This work presents an operational noise characterization and band-integrated detection limit analysis of a TFPA under controlled sinusoidal excitation. The sensor was excited between 50 Hz and 3200 Hz with an acceleration amplitude of 9.81 m/s^2 (1 g). Deterministic signal components were separated from stochastic fluctuations using harmonic regression, and the residual signals were analyzed through Welch Power Spectral Density (PSD) estimation to obtain the operational noise spectrum. The equivalent acceleration noise density was found to remain on the order of 10^{-4} g/$\sqrt{\text{Hz}}$ across most of the analyzed frequency range. Band-integrated analysis yielded detection limits of approximately 3.09 mg Root-Mean-Square (RMS) in the 50–250 Hz band and 22.42 mg RMS over the full 50–3200 Hz range for a unity Signal-to-Noise Ratio (SNR) criterion. These results establish the stochastic performance limits of the TFPA and provide a quantitative assessment of its operational vibration detection capability under the present measurement conditions, thereby contributing to a more complete evaluation of TFPAs as mechanically tunable sensors for practical vibration monitoring applications.**

Keywords*- *Piezoelectret accelerometer; Vibration sensing; Operational noise characterization; Detection limits; Power spectral density; Harmonic regression.

I. INTRODUCTION

Piezoelectret-based sensing technologies have emerged as a lightweight and cost-effective alternative to conventional piezoelectric accelerometers. Owing to their electret charge storage capability and mechanically compliant polymer structures, piezoelectrets enable geometrically tunable transduction mechanisms that are attractive for vibration sensing applications [1]–[3].

Recently, a Thermo-Formed Piezoelectret Accelerometer (TFPA) architecture based on an open tubular polymer electret structure fabricated by thermo-forming was introduced and experimentally validated, demonstrating adjustable dynamic response through seismic mass variation and structural configuration [4][5]. Subsequent investigations provided extended dynamic characterization under controlled excitation conditions [6] and demonstrated the tunability and application potential of the device in domain-specific scenarios such as agricultural monitoring [7]. Collectively, these studies established the TFPA platform in terms of design, dynamic response, and application-oriented tunability.

While sensitivity and frequency response are fundamental performance metrics [8], they are not sufficient to fully characterize the detection capability of a dynamic sensor. The minimum measurable acceleration level is limited by stochastic noise contributions originating from the sensing structure, the transduction mechanism, the signal conditioning electronics, and the data acquisition chain [9]. In accelerometer research, noise is often reported as voltage noise density or equivalent acceleration noise density, typically measured under quiescent or unloaded conditions. However, practical sensing scenarios commonly involve operation under dynamic excitation, where deterministic vibration components coexist with stochastic fluctuations.

When a sensor is subjected to controlled sinusoidal excitation, the measured output contains a deterministic component phase-locked to the excitation frequency, potentially accompanied by higher-order harmonics arising from nonlinearities. Superimposed on these components is a stochastic contribution that represents operational noise. If deterministic components are not explicitly removed, Power Spectral Density (PSD) estimates may be biased, particularly near the excitation frequency, leading to inaccurate noise quantification [10]. Furthermore, detection limits derived from spectral quantities depend on the frequency band over which noise is integrated, emphasizing the importance of band-specific evaluation rather than single-value noise floor reporting [11].

To address these aspects, the present study adopts a signal processing framework for operational noise characterization under sinusoidal excitation. The deterministic component at the excitation frequency and its harmonics is estimated via harmonic regression using sine–cosine basis functions and subsequently removed from the measured signal. The residual signal is then analyzed using Welch PSD estimation [10] to obtain the voltage noise density. By combining the residual spectral density with the sensitivity estimated through harmonic regression, an equivalent acceleration noise density is derived. Band-integrated Root-Mean-Square (RMS) noise

levels are subsequently obtained by integrating the equivalent acceleration noise density over specified frequency intervals, from which the corresponding detection limits are derived [11]. In addition, the analysis accounts for heterogeneous acquisition sampling rates by interpolating spectra onto a common frequency grid bounded by the minimum Nyquist frequency.

Using this approach, the operational noise characteristics and band-integrated detection limits of a TFPA equipped with a 30 g seismic mass are established over the 50–3200 Hz frequency range under controlled sinusoidal excitation with an amplitude of 9.81 m/s^2 (1 g). The resulting detection limits provide a metrologically transparent assessment of the operational sensing capability of the TFPA under the present measurement conditions.

The remainder of this paper is organized as follows. Section II describes the experimental setup and measurement conditions. Section III presents the signal processing methodology used for operational noise estimation and detection limit calculation. Section IV reports the experimental results, which are subsequently discussed in Section V. Finally, the main conclusions of this work are summarized in Section VI.

II. Experimental Setup

A. Device Configuration

The device under investigation is a TFPA previously introduced and characterized in [5]–[7]. The sensing element consists of an open tubular thermo-formed polymer electret structure mechanically coupled to a rigid seismic mass. A schematic representation of the sensing structure is shown in Figure 1.

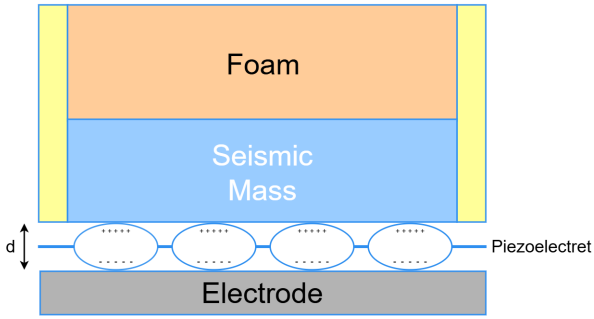

Figure 1. Schematic representation of the TFPA sensing structure.

In the present study, the accelerometer was configured with a seismic mass of 30 g, corresponding to the configuration analyzed in the most recent application-oriented investigation [7]. The electrical output of the TFPA was conditioned using the same signal conditioning chain described in the previous studies to ensure consistency in transduction gain and bandwidth. No modifications were introduced in the sensing structure or conditioning electronics for the present measurements.

B. Excitation Conditions

Dynamic characterization was performed using controlled electrodynamic excitation. The accelerometer was mounted on a vibration exciter together with a reference accelerometer and subjected to sinusoidal acceleration with a nominal amplitude of 1 g. A schematic representation of the experimental setup is shown in Figure 2.

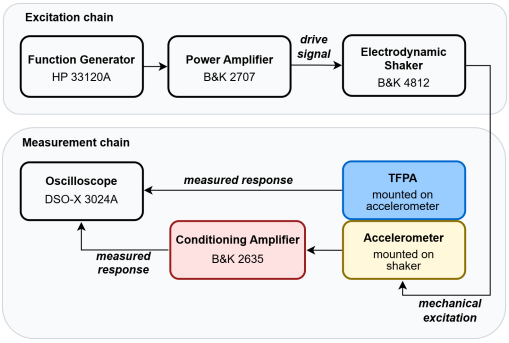

Figure 2. Experimental setup used for dynamic characterization of the TFPA.

Sinusoidal excitation was applied over the frequency range from 50 Hz to 3200 Hz.

The excitation level was monitored using a calibrated Brüel & Kjær 8305 reference accelerometer connected to a B&K 2635 charge amplifier configured with an output sensitivity of 316 mV/g.

C. Data Acquisition

For each excitation condition, three synchronized time-domain signals were recorded:

- time vector t (s),
- output voltage of the reference accelerometer v_{ref} (V),
- output voltage of the TFPA v_{tfpa} (V).

The sampling frequency of each record was determined directly from the time vector as the inverse of the median sampling interval. Since the dataset contains records acquired at different sampling frequencies, this variability is accounted for in the signal processing procedure described in Section III.

III. Signal Processing and Operational Noise Estimation

This section describes the signal processing procedure used to separate deterministic excitation components from stochastic noise in the measured TFPA signals. The methodology includes harmonic regression for removal of the deterministic response, PSD estimation of the residual signal, and the derivation of equivalent acceleration noise density and band-integrated detection limits.

A. Pre-processing and Sensitivity Estimation

For each excitation frequency f_0, the acquired time-domain signals $v_{\mathrm{tfpa}}(t)$ and $v_{\mathrm{ref}}(t)$ were first centered by subtracting their mean value in order to remove DC offsets:

$$v(t) \leftarrow v(t) - \overline{v} \tag{1}$$

where $\overline{v}$ denotes the arithmetic mean over the record duration.

The fundamental amplitude of the TFPA output at the excitation frequency was estimated using harmonic regression. The measured signal was projected onto sine and cosine basis functions at f_0:

$$v_{\mathrm{tfpa}}(t) \approx A_1 \sin(2\pi f_0 t) + B_1 \cos(2\pi f_0 t) \tag{2}$$

The peak amplitude of the fundamental component was then obtained as

$$V_{\mathrm{amp}} = \sqrt{A_1^2 + B_1^2}. \tag{3}$$

Since the excitation amplitude was experimentally adjusted to 1 g peak-to-peak, the corresponding peak acceleration amplitude is $a_p = 0.5$ g. The sensitivity of the accelerometer was therefore calculated as

$$S(f_0) = \frac{V_{\mathrm{amp}}}{0.5\ g} \quad [\mathrm{V/g}]. \tag{4}$$

This procedure was repeated for all excitation frequencies, resulting in a discrete sensitivity curve $S(f_0)$ over the 50–3200 Hz range.

B. Harmonic Regression and Residual Signal Definition

Under sinusoidal excitation, the measured signal may contain higher-order harmonics due to nonlinearities in the sensing structure or conditioning electronics. To isolate the stochastic component, harmonic regression including up to H harmonics was performed:

$$\hat{v}(t) = \sum_{h=1}^{H} \left[A_h \sin(2\pi h f_0 t) + B_h \cos(2\pi h f_0 t) \right]. \tag{5}$$

The number of harmonics was selected as

$$H = \min\left(5, \left\lfloor \frac{F_s/2}{f_0} \right\rfloor\right), \tag{6}$$

ensuring that harmonic components did not exceed the Nyquist frequency while limiting overfitting.

The residual signal, interpreted as operational noise, was defined as

$$r(t) = v_{\mathrm{tfpa}}(t) - \hat{v}(t). \tag{7}$$

C. Power Spectral Density Estimation

The residual signal was analyzed using Welch PSD estimation with a Hann window, segment length of 512 samples, and 50% overlap. The PSD estimate is denoted as

$$P_{rr}(f) \quad [\mathrm{V^2/Hz}]. \tag{8}$$

where $P_{rr}(f)$ denotes the PSD of the residual signal $r(t)$.

The corresponding voltage noise density was computed as

$$S_V(f) = \sqrt{P_{rr}(f)} \quad [\mathrm{V}/\sqrt{\mathrm{Hz}}]. \tag{9}$$

The Welch method provides statistical averaging through segmentation of the residual signal, allowing stable spectral estimation of the noise spectrum.

D. Common Frequency Grid for Heterogeneous Sampling Rates

Measurements acquired at different sampling frequencies lead to PSD estimates with different frequency resolutions and Nyquist limits. To allow consistent aggregation across excitation conditions, the individual PSDs were interpolated onto a common frequency grid.

The common grid was defined using the largest frequency-bin spacing among all records and was limited to the smallest Nyquist frequency observed in the dataset. Each individual spectrum was then mapped onto this grid using piecewise linear interpolation.

The median voltage noise density across all excitation conditions was then computed as

$$S_V^{\mathrm{med}}(f) = \mathrm{median}_i\{S_{V,i}(f)\}, \tag{10}$$

where i indexes the excitation frequencies. The median was adopted as a robust central estimator in order to reduce the influence of occasional residual spectral peaks and inter-record variability.

E. Equivalent Acceleration Noise Density

The frequency-dependent sensitivity curve $S(f)$ was obtained by interpolating the discrete sensitivity estimates $S(f_0)$ onto the common PSD frequency grid using piecewise linear interpolation. The equivalent acceleration noise density was then computed as

$$S_a(f) = \frac{S_V^{\mathrm{med}}(f)}{S(f)} \quad [g/\sqrt{\mathrm{Hz}}]. \tag{11}$$

F. Band-Integrated Detection Limits

The band-integrated RMS acceleration noise over a frequency interval $[f_1, f_2]$ was computed as

$$a_{n,\mathrm{RMS}} = \sqrt{\int_{f_1}^{f_2} S_a^2(f)\, df}. \tag{12}$$

In discrete form,

$$a_{n,\mathrm{RMS}} = \sqrt{\sum_{f_k \in [f_1, f_2]} S_a^2(f_k)\, \Delta f}. \tag{13}$$

The resulting quantity, expressed in g RMS, is defined as the band-integrated operational detection limit for the specified frequency interval.

IV. Results

This section presents the experimental results obtained from the TFPA measurements under controlled sinusoidal excitation. The analysis focuses on three main aspects: the sensitivity of the sensor $S(f)$, the operational noise spectrum $S_V(f)$ obtained from the residual signals after harmonic regression, and the resulting band-integrated detection limits derived from the equivalent acceleration noise density $S_a(f)$.

A. Sensitivity and Signal-to-Noise Ratio

The sensitivity of the TFPA was obtained from the fundamental harmonic amplitude extracted via harmonic regression, according to (4). The resulting sensitivity curve exhibits a pronounced maximum near the resonance region, while the remaining excitation frequencies present substantially lower sensitivity values.

Figure 3 presents the frequency dependence of the TFPA sensitivity obtained from the harmonic regression procedure.

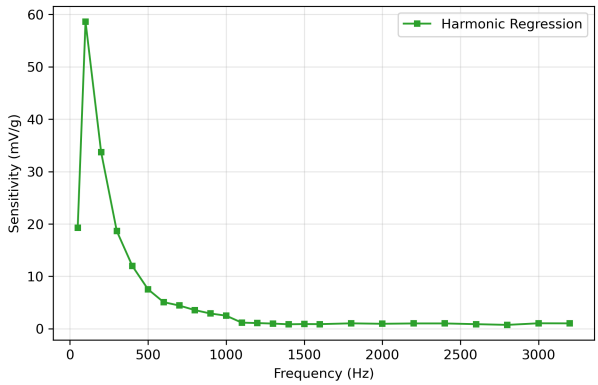

Figure 3. Sensitivity $S(f)$ of the TFPA obtained from harmonic regression.

To evaluate the consistency of the sensitivity estimation procedure, the sensitivity obtained directly from the time-domain [7] was compared with the sensitivity derived from the fundamental component estimated through harmonic regression. The comparison between both estimates is shown in Figure 4.

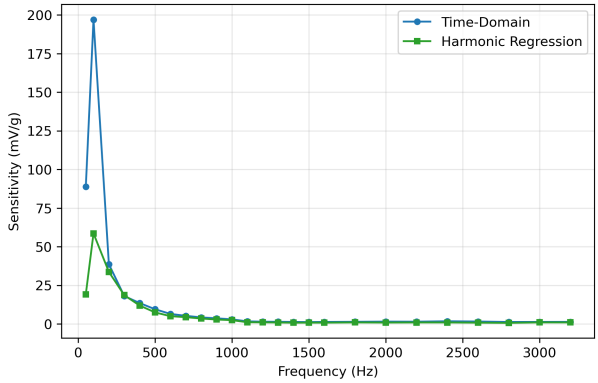

Figure 4. Comparison between TFPA's sensitivity estimated directly from the time-domain signal and from harmonic regression of the fundamental component.

Across the analyzed excitation frequencies between 50 Hz and 3200 Hz, the Signal-to-Noise Ratio (SNR), defined as the ratio between the deterministic fundamental amplitude and the RMS residual noise level, varied between approximately 12.6 dB and 43.1 dB. These values indicate that the deterministic component of the TFPA response remained clearly distinguishable from the residual noise across the analyzed frequency range.

B. Operational Noise Spectral Density

Following harmonic regression, the residual signals were analyzed using Welch PSD estimation. The resulting voltage noise densities $S_V(f)$ from all excitation conditions were interpolated onto a common frequency grid and aggregated using the median estimator (10).

To assess whether the observed spectral levels were dominated by the TFPA or by the measurement chain, the voltage noise density was compared with that of the reference accelerometer channel. Figure 5 presents this comparison.

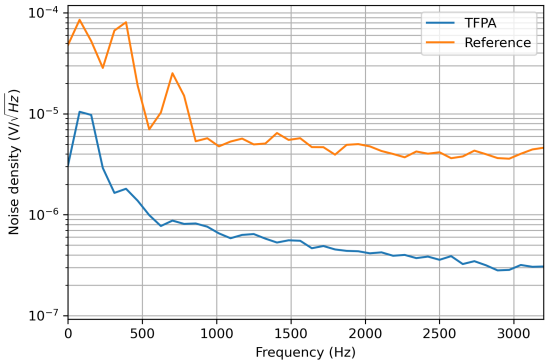

Figure 5. Comparison between the voltage noise density $S_V(f)$ of the TFPA channel and the reference accelerometer channel.

The median voltage noise density exhibited an overall decreasing trend with increasing frequency. At low frequencies near 78 Hz, the median voltage noise density was approximately 1.05×10^{-5} V/$\sqrt{\text{Hz}}$.

Across the analyzed frequency range, the voltage noise density measured at the TFPA output remained consistently below the noise level observed in the reference channel. This result indicates that the TFPA measurement channel exhibited a lower voltage noise density than the reference measurement channel under the present experimental conditions. In this context, the reported noise floor should be interpreted as an operational measurement result of the complete sensing setup, rather than as a fully isolated estimate of the intrinsic TFPA transduction noise.

Using the interpolated sensitivity curve $S(f)$, the voltage noise density $S_V(f)$ was converted into equivalent acceleration noise density $S_a(f)$ according to (11). Figure 6 presents the resulting equivalent acceleration noise spectrum.

Across the analyzed frequency range up to 3200 Hz, the median equivalent acceleration noise density remained on the order of 10^{-4} g/$\sqrt{\text{Hz}}$, with typical values around 1.5×10^{-4} g/$\sqrt{\text{Hz}}$ in the mid-frequency region.

C. Band-Integrated Detection Limits

Band-integrated detection limits were computed by integrating the equivalent acceleration noise density $S_a(f)$ over specified frequency intervals according to (13). The resulting RMS acceleration noise defines the operational detection limit for each band.

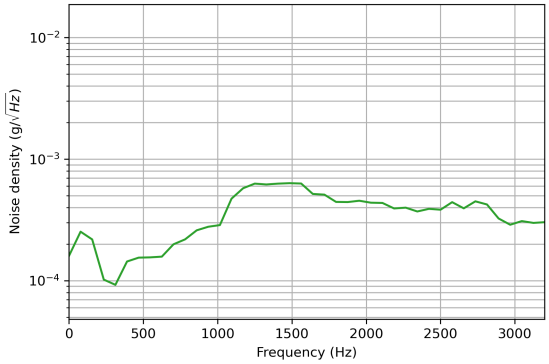

Figure 6. Equivalent acceleration noise density $S_a(f)$ obtained from the TFPA voltage noise density $S_V(f)$ using the interpolated sensitivity curve $S(f)$.

For a detection criterion corresponding to SNR = 1, the resulting detection limits were:

- 3.09 mg RMS for the 50–250 Hz band,
- 3.70 mg RMS for the 50–500 Hz band,
- 22.42 mg RMS for the full 50–3200 Hz band.

When adopting a more conservative detection criterion of SNR = 3, the corresponding detection limits increased to:

- 9.26 mg RMS (50–250 Hz),
- 11.10 mg RMS (50–500 Hz),
- 67.25 mg RMS (50–3200 Hz).

Figure 7 summarizes the resulting detection limits for the analyzed frequency bands.

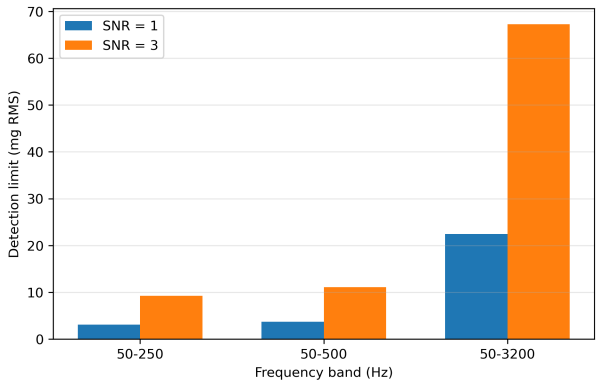

Figure 7. Band-integrated detection limits of the TFPA for different frequency bands and detection criteria.

As expected, the detection limit increases with the integration bandwidth due to the cumulative contribution of spectral noise components. Nevertheless, within the lower frequency band most relevant for many vibration monitoring applications (50–250 Hz), the TFPA demonstrated operational detection limits on the order of only a few milligravity RMS.

These results provide a quantitative assessment of the operational sensing capability of the TFPA and complement the sensitivity and tunability characteristics previously reported for this device architecture.

V. Discussion

This section interprets the experimental results in terms of the sensing characteristics and operational behavior of the TFPA. In particular, the sensitivity, stochastic noise behavior, and band-integrated detection limits are analyzed to assess the practical vibration sensing capability of the device.

A. Sensitivity Characteristics

The experimentally observed sensitivity exhibits a pronounced dependence on excitation frequency. This behavior is consistent with the expected dynamics of a mass–spring sensing structure, in which the mechanical transfer function varies across the analyzed frequency range.

Such sensitivity variation was previously reported for the TFPA architecture and attributed to the dynamic interaction between the thermo-formed electret structure and the seismic mass [6]. The present results confirm that this behavior persists under the operational conditions used for noise characterization.

To evaluate the consistency of the sensitivity estimation procedure, the sensitivity obtained directly from the time-domain signal was compared with the sensitivity derived from the fundamental component estimated through harmonic regression, as shown in Figure 4.

A strong agreement between the two estimates is observed over most of the analyzed frequency range, indicating that the deterministic component of the TFPA response is well captured by the harmonic model. Larger deviations occur near the resonance region, where the estimate derived from the time-domain signal tends to exceed the fundamental-based estimate. This behavior suggests that the waveform departs from a purely sinusoidal shape under dynamic amplification, likely due to increased harmonic content and residual waveform distortion.

The wide dynamic range of sensitivity observed across the analyzed frequency range also reflects the tunable nature of the TFPA concept. As demonstrated in previous work [7], modifications of the seismic mass or structural geometry allow the operational response of the sensor to be shifted toward application-specific frequency bands.

B. Operational Noise Behavior

The spectral analysis of the residual signals revealed a stable operational noise floor across the analyzed frequency range after removal of the deterministic excitation components. The remaining stochastic component of the TFPA signal exhibited a broadband spectral distribution, as illustrated in Figure 5 and Figure 6.

The use of Welch PSD estimation introduces statistical averaging through segmentation of the residual signal, which contributes to the stability of the spectral estimates obtained from each measurement record.

The voltage noise density generally decreased with increasing frequency, reflecting the combined influence of the sensor transduction mechanism and the electronic measurement chain. When converted to equivalent acceleration units using

the sensitivity, the resulting noise spectrum remained within the order of 10^{-4} g/$\sqrt{\text{Hz}}$ over most of the analyzed range.

A reduction in the equivalent acceleration noise can be observed near the resonance region. This behavior results from the increase in mechanical sensitivity in that frequency range. Since the equivalent acceleration noise density is obtained by dividing the voltage noise density by the sensitivity, the enhanced transduction gain effectively reduces the acceleration-equivalent noise level near resonance.

An important observation arises from the comparison between the TFPA noise spectrum and the reference accelerometer channel shown in Figure 5. Across the evaluated frequency bands, the voltage noise density measured at the TFPA output remained consistently lower than that observed in the reference channel, with clearly distinct residual spectral levels under the present experimental conditions. This comparison indicates that the residual spectral levels depend on the implemented measurement channel, and that the reported noise floor should not be interpreted as a fully isolated estimate of the intrinsic TFPA transduction noise, but rather as an operational result of the TFPA measurement chain.

C. Band-integrated detection limits

The band-integrated detection limits obtained in this study provide a practical measure of the operational sensing capability of the TFPA. While the spectral noise density characterizes the stochastic behavior of the sensor at individual frequencies, the integrated RMS acceleration noise quantifies the minimum detectable vibration level over a specified frequency band.

As expected, the detection limit increases with the integration bandwidth due to the cumulative contribution of spectral noise components. This behavior reflects the broadband nature of the residual noise spectrum observed after removal of the deterministic excitation.

Within the lower frequency band analyzed (50–250 Hz), the TFPA demonstrated a detection limit of approximately 3.09 mg RMS for a unity SNR criterion. Even when adopting a more conservative threshold (SNR = 3), the corresponding detection limit remains below 10 mg RMS in this band. These values indicate that the sensor is capable of resolving vibration levels in the milligravity range when operating within moderate bandwidths.

An important aspect of the obtained detection limits is that they were derived from operational measurements performed under controlled sinusoidal excitation. In this context, the reported values represent operational detection limits that incorporate not only the intrinsic sensor response but also the influence of the measurement chain and the experimental excitation environment. As such, they provide a realistic assessment of the detection capability that can be expected when the device operates in practical measurement conditions.

D. Implications for TFPA-based sensing applications

The results presented in this study extend the characterization of the TFPA beyond sensitivity and structural tunability by providing a quantitative assessment of its operational noise behavior and detection capability. While previous investigations established the design, dynamic response, and application-oriented tunability of the TFPA [5]–[7], the present work adds an evaluation of its operational stochastic detection limits.

In particular, the operational detection limits derived from the residual spectral analysis provide an estimate of the minimum vibration levels that can be resolved under realistic measurement conditions. The results indicate that the TFPA is capable of detecting acceleration levels in the milligravity range within moderate bandwidths, which are typical of many practical vibration monitoring scenarios.

This capability is especially relevant for applications involving low-cost or distributed sensing systems, where lightweight and mechanically tunable sensors can provide useful vibration information without requiring complex instrumentation. In such contexts, the combination of tunable frequency response, milligravity-level detection limits, and simple electromechanical architecture makes the TFPA a relevant candidate for vibration monitoring tasks in environments where traditional sensing solutions may be impractical or cost-prohibitive.

VI. Conclusion and Future Work

This work presented an operational noise characterization and band-integrated detection limit analysis of a TFPA under controlled sinusoidal excitation. A signal processing framework based on harmonic regression was employed to separate deterministic excitation components from stochastic noise, allowing the residual signal to be analyzed using PSD estimation.

The results demonstrated that the TFPA exhibits a sensitivity consistent with the dynamic behavior of a mass–spring sensing structure, while maintaining a stable operational noise floor across the analyzed frequency range. The equivalent acceleration noise density remained on the order of 10^{-4} g/$\sqrt{\text{Hz}}$, leading to band-integrated detection limits of approximately 3.09 mg RMS in the 50–250 Hz band and 22.42 mg RMS over the full 50–3200 Hz range for a unity SNR criterion.

These results provide a quantitative assessment of the operational vibration detection capability of the TFPA. The present noise characterization helps establish the operational performance limits of the device and contributes to a more complete evaluation of its potential as a mechanically tunable accelerometer architecture for practical vibration sensing applications.

The present study is limited to one TFPA configuration with a 30 g seismic mass and one excitation level of 1 g over the analyzed frequency range. Repeatability across repeated runs, specimen-to-specimen variability, uncertainty quantification, and sensitivity to processing choices were not exhaustively investigated here and should be addressed in future work. Further studies may also investigate approaches to better separate the intrinsic sensor noise from the contribution of the conditioning and acquisition chain.

REFERENCES

[1] M. M. Moreira et al., "Piezoelectrets: A brief introduction," *IEEE Sensors Journal*, vol. 21, pp. 22 317–22 328, 2021.

[2] R. A. Altafim et al., "Piezoelectrets from thermo-formed bubble structures of fluoropolymer- electret films," *IEEE Transactions on Dielectrics and Electrical Insulation*, vol. 13, pp. 979–984, 5 2006.

[3] R. A. P. Altafim et al., "Template-based fluoroethylenepropylene piezoelectrets with tubular channels for transducer applications," *Journal of Applied Physics*, vol. 106, p. 014 106, 2009.

[4] J. F. Alves et al., "An accelerometer based on thermoformed piezoelectrets with open-tubular channels," *Annual Report - Conference on Electrical Insulation and Dielectric Phenomena, CEIDP*, vol. 2020-October, pp. 524–526, 2020.

[5] I. N. Soares et al., "New design for a thermo-formed piezoelectret-based accelerometer," in *ALLSENSORS 2023, The Eighth International Conference on Advances in Sensors, Actuators, Metering and Sensing*, IARIA, 2023, pp. 21–24.

[6] I. N. Soares, R. A. C. Altafim, R. A. P. Altafim, and M. M. Tokoro, "Investigation of thermo-formed piezoelectret accelerometer under different electrodynamic vibration conditions," in *ALLSENSORS 2024, The Ninth International Conference on Advances in Sensors, Actuators, Metering and Sensing*, IARIA, 2024, pp. 32–37.

[7] I. N. Soares, R. A. C. Altafim, and R. A. P. Altafim, "Applicability assessment of a thermo-formed piezoelectret accelerometer in agricultural robotics systems," in *ALLSENSORS 2025, The Tenth International Conference on Advances in Sensors, Actuators, Metering and Sensing*, IARIA, 2025, pp. 19–25.

[8] J. Hillenbrand, S. Haberzettl, T. Motz, and G. M. Sessler, "Electret accelerometers: Physics and dynamic characterization," *The Journal of the Acoustical Society of America*, vol. 129, no. 6, pp. 3682–3689, Jun. 2011.

[9] C. D. Motchenbacher and J. A. Connelly, *Low-noise electronic system design*. Nashville, TN: John Wiley & Sons, 1993.

[10] D. B. Percival and A. T. Walden, *Spectral Analysis for Physical Applications*. Cambridge, England: Cambridge University Press, 1993.

[11] J. Bendat and A. Piersol, *Random Data: Analysis and Measurement Procedures*, Fourth Edition. Wiley, 2010.